Controlled surface manipulation at the nanometer scale based on the atomic force microscope

Rubio Sierra, Francisco Javier

München 2006

Controlled surface manipulation at the nanometer scale based on the atomic force microscope

Rubio Sierra, Francisco Javier

Dissertation
an der Fakultät für Geowissenschaften
der Ludwig–Maximilians–Universität
München

vorgelegt von
Rubio Sierra, Francisco Javier
aus Sevilla (Spanien)

München, den 5 September 2006

Contents

List of Figures

List of Tables

Abbreviations

ADC	Analog to Digital Converter
AFM	Atomic Force Microscope
BASIC	Beginner's All-purpose Symbolic Instruction Code
CCD	Charged Coupled Device
CD-R	Compact Disc Recordable
CMOS	Complementary Metal-Oxide-Semiconductor
DAC	Digital to Analog Converter
DPL	Dynamic Plowing Lithography
DSP	Digital Signal Processor
FISH	Fluorescence In Situ Hybridisation
FMA	First Mode Approximation
FWHM	Full Width at Half Maximum
GUI	Graphical User Interface
LASER	Light Amplification by Stimulated Emission of Radiation
LHP	Left Half Plane
MFA	Microscopio de Fuerzas Atómicas
MFC	Microsoft Foundation Classes
MIMO	Multiple Input Multiple Output
PCR	Polymerasa Chain Reaction
RHP	Right Half Plane
RKM	Rasterkraftmikroskop
SPICE	Simulation Program with Integrated Circuits Emphasis
SMD	Surface Mount Devices
SPM	Scanning Probe Microscopy
STM	Scanning Tunneling Microscope
TTL	Transistor-Transistor Logic
UHV	Ultra High Vacuum
UV	UltraViolet

Zusammenfassung

Ziel dieser Arbeit ist die Entwicklung theoretischer und experimenteller Methoden zur kontrollierten Manipulation von Oberflächen auf der Nanometerskala sowie die Realisierung eines Nanomanipulators auf Basis eines Rasterkraftmikroskops (RKM).

Die Übertragungsfunktion eines dynamischen Systems wie dem RKM erlaubt nicht nur eine theoretische Charakterisierung, sondern ist auch für die Analyse von Stabilität und Steuerbarkeit in verschiedenen Systemkonfigurationen einsetzbar. Die abgeleitete Übertragungsfunktion entspricht einem realistischen Modell des Sensors des RKMs bei Betrachtung sowohl aller seiner Resonanzmoden als auch der Spitzen-Oberfläche Wechselwirkung. Diese theoretische Beschreibung wird durch die Messung der Frequenzantwort entlang des Federbalkens bestätigt.

Verschiedene experimentelle Methoden und Steuerungsverfahren sind im *NanoManipulator* kombiniert um die Verwendbarkeit des RKMs für die Modifizierung von Oberflächen zu optimieren. Lichtmikroskopie ermöglicht die schnelle Untersuchung der Probe und exakte Positionierung der RKM-Spitze auf der für die Manipulierung gewünschten Region. Zusätzlich bietet die UV-Laser gestützte Ablation eine Möglichkeit zur kontaktfreien Manipulation verschiedener Materialien, einschließlich biologischer Proben. Zwei verschiedene Möglichkeiten für die Steuerung des Systems sind im *NanoManipulator* enthalten: (i) automatisierte Steuerung durch Anwendung eines Vektor-Raster Moduls, und (ii) interaktive Steuerung durch Benutzung einer haptischen Schnittstelle.

Als beispiele des *Nanomanipulators* werden zwei verschiedene Standardmethoden für dynamische RKM-Lithographie (*dynamic* und *modulated plowing*) zur Profilierung dünner Fotolackfilme verglichen. Die Ergebnisse der Experimente zeigen, dass durch die Modulation der Indentierungskraft, mit der im *modulated plowing* Modus die Spitze im ständigen Kontakt mit der Oberfläche gehalten wird, eine gute Reproduzierbarkeit erreicht wird und unerwünschte Artefakte vermieden werden.

Die Isolierung und Entnahme von lokalisierten Abschnitten menschlicher Chromosomen ist eine viel versprechende Alternative für die Analyse menschlichen Erbguts. Der *NanoManipulator* ist ein besonders geeignetes Werkzeug für die Realisierung einer solchen Anwendung. Für den direkten Vergleich beider Methoden werden zwei nebeneinander liegende Chromosomen mittels RKM basierter

mechanischer Manipulation sowie kontaktfreier Ablation durch UV-Laser dissek-
tiert. Die Ergebnisse beider Manipulationsverfahren werden vor Ort mit Hilfe von
RKM analysiert und zeigen, dass die mechanische Manipulation ein hochpräzises
Verfahren jenseits der Lichtbeugungsgrenze darstellt.

Bei der akustischen Kraftlithographie, einer neuen Methode der RKM-basierten
Lithographie, wird der RKM-Federbalken durch Schallwellen angesteuert, die bei
der Messung von der Probenoberfläche aus eingekoppelt werden. Der Einfluss
von Frequenz und Größe der Schallwellen zusammen mit der Vorlast des Feder-
balkens werden ausführlich analysiert. Akustische Kraftlithographie ist entweder
als ein eigenständiges Verfahren oder als Ergänzung anderer Methoden für die
Feinjustierung von Manipulationskräften anwendbar.

Abstract

The object of this thesis is the development of theoretical and experimental methods for the controlled manipulation of surfaces at the nanometer scale, including the design, construction and experimental demonstration of an atomic force microscope (AFM) based manipulator.

The transfer function description of an AFM system not only offers a theoretical dynamic characterization but, additionally, it is appropriate for the analysis of stability and controllability of different system configurations, i.e. different inputs and outputs. In this thesis, transfer functions are derived that correspond to a realistic model of the AFM sensor, including all its resonance modes and the tip-sample interaction. This theoretical description is then validated using the frequency response along an AFM cantilever.

Different experimental and control techniques have been combined in the NanoManipulator system to optimize AFM lithography. Optical video microscopy allows a fast recognition of the sample and exact positioning of the AFM tip in the particular region of interest, while UV-laser ablation offers the possibility of non-contact manipulation of a wide range of materials, including biological specimens. Two different control approaches have been implemented in the NanoManipulator system: (i) automated control using a vector-scan module, and (ii) interactive control based on the use of a haptic interface.

Using the NanoManipulator, the two different standard AFM lithography techniques based on dynamic methods (namely dynamic and modulated plowing) are compared by performing nanopatterning on thin resist films. The results reflect that modulated plowing, where the AFM tip is in permanent contact with the resist surface while the force is being modulated, offers the highest reliability, minimizing undesired side effects.

The isolation and extraction of localized regions of human metaphase chromosomes represents a promising alternative to standard methods for the analysis of genetic material. The NanoManipulator is an excellent tool for such application, as it is here illustrated by comparing AFM based mechanical dissection and non-contact ablation on side by side chromosomes. The results are analyzed *in situ* using AFM imaging, revealing the high precision of mechanical dissection.

Acoustical force nanolithography is a novel method for AFM based lithogra-

phy where the cantilever is actuated using an acoustic wave coupled through the sample surface. The influence of acoustic wave frequency and magnitude, along with the preloading force of the cantilever are studied in detail. Acoustical force nanolithography can be used as a stand alone method or as a complement for the fine adjustment of manipulation forces.

Resumen

La finalidad de esta tesis es el desarrollo de métodos experimentales y teóricos para la modificación controlada de superficies en la escala del nanómetro, incluyendo el diseño, realización y demonstración experimental de un manipulador basado en el microscopio de fuerzas atómicas (MFA).

La descripción de un sistema dinámico, como el MFA, basada en la función de transferencia del sistema no sólo ofrece una caracterización teórica, además es el método adecuado para el análisis de la estabilidad y controlabilidad de diferentes configuraciones, es decir elección de distintas entradas y salidas. La función de transferencia obtenida corresponde a un modelo realista del sensor, incluyendo todos sus modos de resonancia y la interacción entre la punta y la superficie. Esta descripción teórica es validada usando la medida de la respuesta de frequencias del sistema a lo largo del sensor del MFA.

El sistema *NanoManipulator* combina diferentes técnicas experimentales y de control en un solo instrumento para optimizar métodos de litografía basados en el MFA. Microscopía óptica equipada con vídeo permite una inspección rápida de la muestra y un posicionamiento exacto de la punta del MFA sobre la región de interés. Por otro lado, la ablación a través de un laser ultravioleta ofrece la posibilidad de realizar manipulación libre de contacto en un gran rango de materiales, incluyendo especímenes biológicos. Dos métodos diferentes de controlar el sistema han sido implementados en el *NanoManipulator*: (i) control automático a través de un módulo de escaneado vectorial y (ii) control interactivo usando un interfaz háptico.

Las dos técnicas estandar basadas en modos dinámicos del MFA (*dynamic* y *modulated plowing*) para realizar litografía son analizados en su aplicación para el modelado de películas ultrafinas de polímeros. Los resultados reflejan que *modulated plowing*, en el cual la punta está en contacto permanente con la superficie mientras que la fuerza indentora es modulada, ofrece una alta reproducibilidad del proceso y minimiza otros efectos colaterales no deseados.

La separación y extracción de regiones localizadas de cromosomas humanos representa una alternativa prometedora para el análisis del genoma humano. Para esta aplicación el *NanoManipulator* es un instrumento altamente adecuado. Su aplicación es demostrada comparando la disección mecánica a traves del MFA

y la ablación libre de contacto a través del laser ultravioleta realizadas quasi-simultaneamente en dos cromosomas diferentes. Los resultados son analizados *in situ* usando el MFA, reflejando la alta precisión del método mecánico cuya resolución supera el límite impuesto por la difracción de la luz.

La nanolitografía de fuerza acústica es un nuevo método donde el cantilever del MFA es actuado usando ondas ultrasónicas acopladas a traves de la superficie de la muestra. La influencia en el proceso de la frecuencia y magnitud de la onda, así como de la energía inicial contenida en la vibración del cantilever es estudiada con detalle. La nanolitografía de fuerza acústica puede ser aplicada como un método independiente, o para el ajuste ultrapreciso de las fuerzas de manipulación.

Chapter 1

Introduction

One milestone on the roadmap of nanotechnology is the fabrication of new materials with improved properties due to specially designed nanometer-scaled features, which directly implies the characterization, change, and control of surfaces at the nanometer scale. Two different approaches are available for nanostructuring and modifying properties of surfaces. In the "bottom-up" approach, molecular self-assembly processes involving non-covalent bonding are used for nanostructuring. The second approach, denominated "top-down", downscales the structuring of surfaces into the nanoscale by using currently available methods, usually high-end lithography processes applied in the semiconductor industry. Although the "bottom-up" approach is quite interesting since it leads to completely new structures, it lacks of a real spatial control of the patterning process and requires additional characterization methods.

The most versatile "top-down" approach to get access to the nanoscale is the lithography of surfaces by scanning probe microscopy (SPM), which relies on the modification of chemical, electrical or mechanical properties of a surface by using a proximal probe. SPM based lithography achieves a high fabrication control over both direction and position. Additionally, SPM offers the possibility of *in situ* ultra-high resolution characterization of the fabrication process and resulting surface structure. The success of SPM also relies on the fact that its application for imaging is not only restricted to topography measurement, but also offers a plethora of possibilities to characterize different surface properties, including the local acquisition of spectroscopy data reaching the single-molecular level.

The first member of the SPM family was the scanning tunneling microscope (STM) [1], invented by Gerd Binnig and Heinrich Rohrer in 1981 at the IBM laboratories in Zürich. The STM measures surface topography using the tunneling current flowing through a nanometer-wide gap between a conductive sharp tip and a conductive sample. The invention of the STM was awarded the Nobel prize in physics in 1986, and led to the development of a vast family of scanning probe

microscopes, each one relying on the measurement of a different physical quantity (tunneling current, contact force, capacitance, amongst others).

The potential of the STM for the local modification of surfaces with a spatial resolution far beyond the light diffraction limit was soon understood by Ringger *et al.* [2] and Staufer *et al.* [3] using electrical pulses on metallic flat surfaces. The field experienced a fast development in different applications including resist exposure and oxidation, material indentation, deposition or removal and etching, reaching its zenith in the astonishing achievement of the positioning of single atoms on a surface by Eigler and Schweizer[1].

However, the STM has some severe limitations, the most important of them being the fact that it is only applicable on conducting surfaces. Another prominent member of the SPM family is the atomic force microscope (AFM), invented by Binnig *et al.* in 1986 [5]. The working principle of the AFM relies on the measurement of the contact force between the apex of a sharp tip attached at the free end of a microcantilever and the sample surface. The main advantages of the AFM are: (i) it can image almost any flat surface, i.e. there is no need for the sample to be conductive; (ii) it can work in different environments including liquids; (iii) it offers a direct measurement of the interaction forces, facilitating the control and characterization of the lithography process. Due to these adventages, the AFM has become the preferred scanning probe microscope in a wide range of scientific and technological applications both for imaging and lithography. This versatility also translates into its application to lithography, allowing for a wide variety of different physical and chemical surface modifications (§ 2.3.2).

However, the research on controllability and the extension of the capabilities of AFM based lithography has just begun, and many issues are still unresolved. The main restrictions to AFM performance in the modification of surfaces include its limited field of operation to areas of some tens of micrometers in diameter, the necessary contact between probe and sample either for imaging or manipulation, and the lack of knowledge about how system dynamics really affects the lithography process.

1.1 Scope of this thesis

The thesis of this work is the improvement of AFM based manipulation by a derivation of a realistic dynamical model based on a transfer function approach, the development of an experimental setup specifically designed for AFM lithography, and the investigation of new actuation methods of the AFM cantilever to enhance lithography controllability.

---

[1]For a general review on STM based lithography see [4].

The transfer function description of a dynamical system is the most appropriate approach for the study of system stability and controllability, since it allows analyzing quantitatively the influence of the system inputs and outputs on the cantilever response. Such a description must consider a realistic model of the AFM system, which implies taking into account both the extended nature of the cantilever (leading to an infinite number of resonance modes) and the tip-sample interaction. A proper validation of the model is offered by the characterization of the frequency response along the AFM cantilever.

The NanoManipulator system developed in this work is an AFM based setup specifically designed for the local modification of surfaces. To enhance performance, the range of operation of AFM has been extended by combining it with optical microscopy. The implementation of UV-laser ablation in the same instrument provides a setup with the ability to perform non-contact lithography of surfaces. Two different control methods for manipulation have been implemented in the NanoManipulator. The first is an automated control based on a vector-scan procedure where the user selects the manipulation parameters and lithography path. The second consists of an interactive control of the system using a joystick stage while the user obtains a tensile feeling of the tip-sample interaction forces through a haptic interface.

Finally, acoustical force nanolithography is a novel method for AFM based mechanical lithography where the cantilever is actuated for manipulation using an acoustic wave coupled through the sample surface.

1.2 Outline

Due to the varied thematic of this work, each chapter is preceded by a short introduction, and includes a brief conclusion section of the respective chapter to facilitate clarity and readability.

In **Chapter 2** the basic concepts of AFM for its application in microscopy and lithography are introduced, and the underlying physical principles are also reviewed. We further give a brief overview of the state-of-the-art in AFM based lithography.

The transfer function description of the AFM system is introduced in **Chapter 3**. For the sake of clarity, we have presented the surface coupled and uncoupled models separately. The implications of the different inputs and outputs on system stability, controllability, and AFM microscopy and lithography operation are also discussed.

In **Chapter 4** the experimental characterization of the frequency response along an AFM cantilever is presented. The transfer function description developed in the previous chapter is used as a validation model for the experimental

data.

Chapter 5 presents the technical characteristics of the NanoManipulator, its operation modes, and the advances it introduces with respect to conventional AFM setups for its application on lithography. The function and performance of the NanoManipulator is illustrated with experimental results.

The analysis of the two different dynamic methods for the mechanical modification of surfaces by AFM applied to the lithography of thin resist films is presented in **Chapter 6**. The transient response of the cantilever during the process is acquired and analyzed. The resulting lithography pattern is characterized by AFM to study the reliability of both methods.

The application of the NanoManipulator to the dissection of human metaphase chromosomes for optimizing current methods of genetic analysis is presented in **Chapter 7**. The mechanical dissection by AFM and the non-contact ablation by UV-laser are directly compared to show the different achievable resolutions.

In **Chapter 8** acoustical force nanolithography is illustrated by a description of the experimental procedure and the characterization of the different parameters that control the process.

Finally, in **Chapter 9**, the conclusions drawn in this work are summarized including an outlook on future development in the field of surface nanomanipulation control by AFM.

Chapter 2

AFM based lithography: working principles

In this chapter the basic principles of AFM based lithography are introduced. Firstly, the mode of operation of standard AFM for imaging is presented. Then, the different theories that describe the tip-sample interaction in the elastic regime are briefly summarized. As basis of surface structuring by AFM the physical mechanisms behind plastic deformation in different materials are introduced. Finally, the standard methods for the modification of materials using AFM are explained, particularly those involving tip-sample mechanical contact.

2.1   The atomic force microscope

2.1.1   Mode of operation

The basic principle of the AFM is the mechanical interaction of a high aspect ratio tip with a sample surface. The AFM probe is attached to the end of a micromachined cantilever which, due to its geometrical and material properties, allows for the precise measuring of the tip-sample interaction forces. The relative position between probe and sample is adjusted by three orthogonal piezoelectric actuators. In order to obtain a surface profile, the AFM probe is scanned over the sample while a detection system measures cantilever deflection. The small radius of the AFM tip at its end (approx. 10–20 nm) enables the outstanding high lateral resolution. The high force resolution of the cantilever in the range of piconewtons combined with the positioning resolution of piezoelectric actuators (approx. 0.1 nm) achieves the high vertical resolution in the subnanometer range.

   The force statically applied by the AFM tip onto the sample is directly related to the flexural deflection Δz of the cantilever. Using Hooke´s law, the applied load

F_{L} is given by:

$$F_{\mathrm{L}} = -k\Delta z, \tag{2.1}$$

where k corresponds to the force constant of the cantilever. For a rectangular cantilever, the force constant is given by

$$k = E\frac{d^3 w}{4L^3}, \tag{2.2}$$

where E is the Young´s module of the cantilever, d is the cantilever thickness, w is the cantilever width, and L corresponds to the cantilever length. However, cantilever thickness is difficult to control in the standard cantilever fabrication process, as nominal thickness values given by the manufacturer are highly inaccurate. Thus, due to the third-power dependance on cantilever thickness of the force constant analytical expression, indirect calibration methods have to be applied in order to obtain more precise values of the force constant [6].

Several methods have been developed for the cantilever deflection detection. Currently, the standard method implemented in most of the systems is the beam deflection method [7], where a collimated laser beam is focused on the cantilever and reflected onto a quadrant photodiode. The current of each quadrant is amplified, converted into a voltage, and electronically processed to obtain the sum of the four detectors (summing signal), the difference between the top and bottom detectors (V_{TB}), and the difference between left and right detectors (V_{LR}). The normal deflection of the cantilever results in a change in the vertical signal V_{TB}, which is used to reconstruct sample topography and determine the loading force on the sample. The lateral deflection of the cantilever is measured using the lateral photodiode signal V_{LR}. Note that the vertical signal of the detector does not directly measure the cantilever position but the cantilever slope. The alternative method is the direct measurement of cantilever position using interferometric methods [8]. Although this approach is seldom found in commercial AFM systems, it represents the detection system of choice for UHV and cryogenic AFM. Figure 2.1 shows the basic components of a standard AFM system.

In standard AFM imaging modes, the maximum normal load exerted by the AFM tip is kept constant during sample scanning by using a proportional-integral regulator to adjust tip vertical position[1]. In up-to-date AFM systems, the feedback loop is managed by a digital system processor (DSP). In each process cycle i the regulator measures a control signal C_i which corresponds to cantilever deflection in contact AFM mode and to cantilever oscillation amplitude in tapping AFM mode.

---

[1]In modern AFM systems, the derivative part of the controller is no longer used, since it does not significantly improve the controller performance while introducing additional noise in the acquired images.
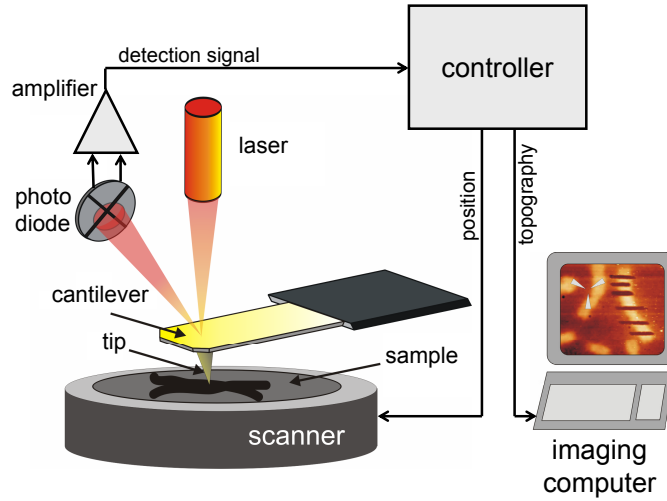
Figure 2.1: Schema of a standard AFM using laser beam deflection detection for the measurement of cantilever flexural and lateral bending.

The regulator error is given by

$$E_i = S - C_i, \tag{2.3}$$

where S is the imaging setpoint which is defined by the user and sets the value of the control signal to be maintained during imaging. In each cycle the regulator calculates the vertical position difference Δz_i to keep the error close to zero, hence maintaining a constant tip load onto the sample during scanning using

$$\Delta z_i = P(E_i) + I(E_{i-1} + E_{i-2} + E_{i-3} + ...), \tag{2.4}$$

where P and I are, respectively, the proportional and integral regulator constants. The magnitudes of the proportional and integral constants have different effects on the transient response of the system. The proportional part of the controller reduces the rise time, increases the overshoot, and reduces the steady-state error, whereas the integral part of the controller decreases the rise time, increases both the overshoot and the settling time, and eliminates the steady-state error. The combination of both parts results in the optimal achievable system response, although both constants must be carefully tuned each time AFM imaging is performed to obtain an optimal image quality: too low constant values lead to poor resolution because the tip insufficiently follows surface topography, while too high values result in tip oscillations which worsen image quality. Figure 2.2 illustrates the tip separate position responses of the proportional and integral part of the controller to a topography step, and shows how the combination of both yields an optimal system response.
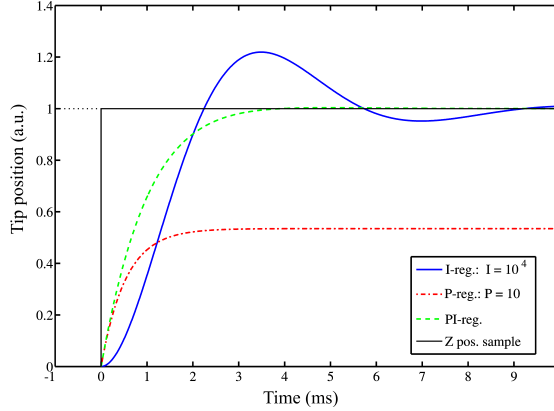
Figure 2.2: Separate tip position responses for different configurations of the feedback controller to a topography step: only proportional part, only integral part, and the combination of both. The proportional part alone produces a large steady-state error, while the integral part produces a considerable overshoot. When both controller parts are combined, the tip response time is optimized and no overshoot is produced. The cantilever described in § 3.1.4 was used to calculate the step response.

One of the main advantages of AFM imaging compared to other high resolution imaging methods such as optical or electron microscopy is that it is inherently three-dimensional. Moreover, unlike in other methods, the probe-sample interaction is relative straightforward and does not highly depend on material properties, except when soft samples are imaged. The most critical issues affecting the metrological correct measurement of surfaces by AFM are caused by noise, positioning errors, and effects due to the finite size of the tip. Imaging noise can be eliminated by filtering or averaging of the acquired data. Positioning errors are minimized by linearizing the piezoelectric actuators using sensors based on interferometry, capacitive detection or strain gauge measurements [9]. Figure 2.3 illustrates the mechanism of imaging distortion due to the finite size of the tip. When lateral dimensions of surface features (especially width and depth of bumps and grooves respectively) are measured by AFM, the tip shape effect must be taken into account. Current correction methods rely on an estimation of the "worst case" tip shape from the acquired image, i.e. calculation of outer bound of tip shape and deconvolution of the estimated shape from the image [10, 11].

2.1.2 AFM imaging modes

Figure 2.4 shows a typical force-distance curve acquired under ambient conditions. When the tip approaches the surface, it snaps into contact with the surface lead-
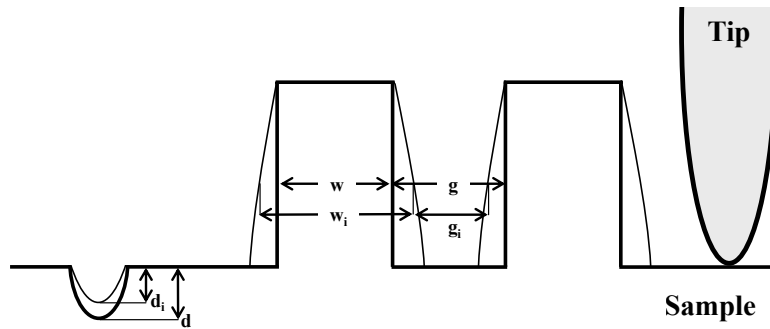
Figure 2.3: Imaging artifacts induced by the finite size of the AFM tip. The thick line shows the sample surface while the thin line represents the tip trajectory, corresponding to the measured topography. The image illustrates how the AFM dimensional measurement overestimates the width of bumps ($w_i > w$) while underestimating the width of grooves ($g_i < g$). Note also the distortion in the measurement of groove depth in features smaller than the tip size ($d_i < d$).

ing to an initial attractive regime. As the cantilever base is further approached toward the sample, the tip-sample interaction force enters into a repulsive regime. When the cantilever base is retracted, the repulsive part of the curve is initially reproduced again, but due to adhesion forces a hysteresis curve is produced when the snap-into contact point is reached. These adhesion forces are mainly caused by the thin water layer covering the sample surface in ambient conditions. In a dry environment, the hysteresis in the force-distance curve is present due to the attractive van der Waals forces and the plastic deformation of the sample surface.

In contact mode AFM the normal deflection of the cantilever, which is directly related to the tip loading force onto the sample by the cantilever force constant, is used as the control signal in the internal feedback loop. The setpoint is selected in such a way that the tip-sample interaction force is in the repulsive regime during imaging. Due to the fact that in contact mode AFM the loading force remains approximately constant, the lateral deflection of the cantilever is directly related to the friction force acting at the tip-sample contact. The measurement of cantilever lateral deflection during contact imaging yields friction maps of the sample, giving insights into surface material properties [12]. Contact mode AFM is a relatively straightforward method which has been applied for the imaging of a wide range of materials. However, due to the combination of tip indentation and lateral forces during scanning, undesired material modification due to wear can occur when imaging soft materials.

In tapping mode AFM, also known in literature as intermittent contact AFM, the cantilever is excited in its first flexural resonant frequency, usually using a dither-piezo. The cantilever oscillation amplitude is used as the control signal in
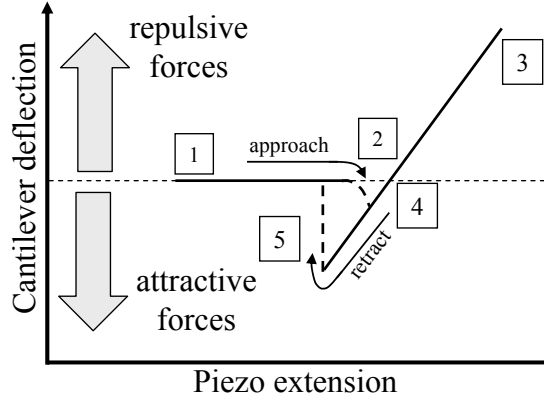
Figure 2.4: Typical force-distance curve acquired under ambient conditions. The AFM tip is initially approached to the surface (1). In close proximity snap into contact is produced (2), then the loading force is increased by extension of the piezoelectric actuator (3). In the withdrawal curve, negative deflection of the cantilever is produced due to surface adhesion (4) until the elastic force in the cantilever is greater than the adhesion force and the tip jumps out of contact (5).

the feedback loop and is kept constant during imaging. In each oscillation cycle, the tip is only in contact with the sample during a finite time corresponding to the lowest part of the oscillation. The maximum load force applied is proportional to the difference between the oscillation amplitudes of the free vibrating and the surface-coupled (during imaging) cantilever. During imaging, the phase difference between cantilever oscillation and excitation signal is proportional to the dissipated energy in the sample, which is related to the surface material properties and used in so-called "phase-imaging" [13]. Tapping mode is especially advantageous in imaging soft samples, although it can be applied for a wide range of materials. Figure 2.5 shows a typical experimental setup for imaging in tapping mode.

Although a plethora of AFM imaging modes exists, we have only described the two most widely extended methods in this section. These are the two imaging modes implemented in the NanoManipulator system (Chapter 5).

2.2 Tip-sample interaction

2.2.1 Lennard-Jones potential

A simple equation to approximately describe the tip-sample interaction force $f_{ts}(d)$ is the Lennard-Jones potential [14, 15]

$$f_{ts}(d) = \frac{A}{d^{12}} - \frac{B}{d^6},$$

(2.5)
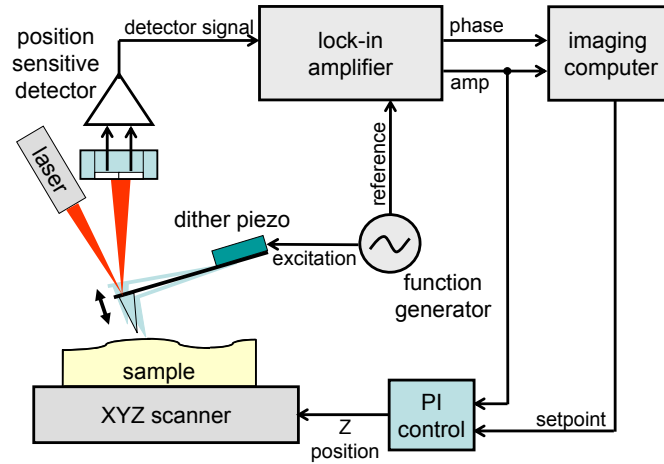
Figure 2.5: Schema of a typical AFM configuration for tapping mode. A lock-in amplifier is used to extract oscillation amplitude and phase shift from the cantilever vertical deflection signal.

where d corresponds to the tip-sample distance, and A and B are factors which are found either theoretically or empirically. The negative term of the Lennard-Jones potential corresponds to the weak attractive van der Waals force which is produced by the intermolecular interaction arising from the dipole moment of molecules. The van der Waals force comprises three different types of forces: (i) *induction* force, (ii) *orientation* force, and (iii) *dispersion* force. Except for small highly polar molecules, such as water, the dominant force in the van der Waals interaction is the dispersion force, which is also present on non-polar molecules and is caused by instantaneous dipole moments in the charge distribution of the electron orbitals in molecules. It is worth noting that the van der Waals force is used to calculate the interaction between macroscopic bodies. Of special interest for AFM is the consideration of a sphere (coresponding to the tip) interacting with a plane (corresponding to the sample). In this case, the van der Waals attractive force $f_{vdw}(d)$ is given by

$$f_{vdw}(d) = -\frac{HR}{6d^2},$$
(2.6)

where H corresponds to the Hamaker´s constant, and R is the sphere radius. The positive term in the Lennard-Jones potential is the repulsive force caused by overlapping electron orbitals (Pauli exclusion principle). A thorough description of the forces constituting the Lennard-Jones potential is found in [16].

2.2.2   Elastic contact regime

In order to obtain a theoretical value of the contact forces, different theories dealing with the elastic deformation of solids can be applied [17, 18]. If both tip and sample are deformed, then the theories of Hertz [19] and Sneddon [20] have to be combined, considering the tip as a sphere of radius R and the sample as a flat surface. The tip-sample contact radius a is given by

$$a = \left(\frac{Rf}{E^*} \right)^{1/3},$$ (2.7)

where f is the effective force, which in this case exclusively corresponds to the external applied load. E^* is the reduced Young´s modulus given by

$$\frac{1}{E^*} = \frac{3}{4} \left(\frac{1 - \nu^2}{E} + \frac{1 - \nu_i^2}{E_i} \right),$$ (2.8)

where E and E_i correspond to the Young´s moduli of the flat surface (sample) and indenter (tip) respectively, while ν and ν_i correspond to the respective Poisson´s ratios. The tip deformation δ_T is given by

$$\delta_T = \frac{f}{E^* a},$$ (2.9)

while the sample deformation δ_S is given by

$$\delta_S = \frac{1}{2} a \ln \left(\frac{R + a}{R - a} \right).$$ (2.10)

The Hertz-Sneddon model does not consider the surface forces, which become important when the tip radius is sufficiently small or the sample surface is adhesive. In the Derjaguin-Müller-Toporov (DMT) theory [21], in addition to the external load force f, adhesion caused by van der Waals forces acting along the contact area perimeter between tip and sample is also taken into account. The DMT model is analytically derived by minimizing the sum of the elastic and surface energies. The effective interaction force f is found in § 3.1.3, while the indentation for a non-deformable spheric indenter is given by

$$\delta_S^{dmt} = \frac{a^2}{R},$$ (2.11)

where the contact radius a is found by using the effective interacting force in (2.7). The DMT theory is an adequate description for surfaces with low adhesion and small tip radii. An alternative approach is the Johnson-Kendall-Roberts (JKR)

theory [22], which considers only short range forces inside the contact region, leading to an effective force f_{jkr} given by

$$f_{\text{jkr}} = \left(\sqrt{f_{\text{n}}} + \sqrt{f_{\text{adh}}} \right)^2 , \tag{2.12}$$

where f_{n} and f_{adh} respectively are the loading and adhesive forces. Again, this effective force is used to calculate the contact radius a in (2.7). The indentation considering a non-deformable spheric indenter is given by

$$\delta_{\text{S}}^{\text{jkr}} = \frac{a^2}{R} - \frac{2}{3} \sqrt{\frac{6\pi W a}{E^*}}, \tag{2.13}$$

where W is the adhesion work per unit area. The JKR model is suitable for surfaces presenting high adhesion and large tip radii. An analytical transition between the JKR and DMT models has been developed by Maugis [23].

When a thin soft film of thickness h on a hard substrate is considered as sample, the force required to cause an indentation increases. An analytical expression for the relationship between applied load and indentation depth has been developed by Dimitriadis *et al.* [24] considering a finite sample thickness in the Hertz model with a non-deformable spheric indenter

$$f_{\text{n}} = \frac{4E\sqrt{R}\delta_{\text{S}}^{3/2}}{3(1-\nu^2)}$$
$$\left[1 - \frac{2\alpha_0}{\pi}\chi + \frac{4\alpha_0^2}{\pi^2}\chi^2 - \frac{8}{\pi^3}\left(\alpha_0^3 + \frac{4\pi^2}{15}\beta_0 \right)\chi^3 + \frac{16\alpha_0}{\pi^4}\left(\alpha_0^3 + \frac{3\pi^2}{5}\beta_0 \right)\chi^4 \right], \tag{2.14}$$

where $\chi = \sqrt{R\delta}/h$, and the constants α_0 and β_0 depend on the sample Poisson´s ratio and on the bonding between the layer and substrate. This expression is equivalent to the Hertz model as h becomes large. Additionally, the term enclosed in the brackets decreases as the sample becomes thinner and, in consequence, a higher load force is required to produce a given indentation.

It is also worth noting that the above described theories only represent a rough estimate for numerical values of applied forces and corresponding indentation, as they are based on the linear elasticity theory: due to the small tip radius of the AFM probe tip indentation produces large local strains that far exceed the linear material elastic regime, even under small loads.

2.2.3 Plastic deformation of materials at the nanometer scale

Engineering materials can be classified at the macro scale into three different groups depending on which mechanism takes place during a deformation caused by an external applied load [25]:

Elastic materials which behave elastically until fracture occurs. All ionic and covalent crystals are in this group.

Elasto-plastic materials are metals that are stressed beyond their elastic limit, producing a permanent deformation without fracture.

Visco-elastic materials plastically deform by a "viscous flow" where molecules or groups of molecules slide over one another as response to the applied stress. Polymers belong to this class of materials.

Two fundamental mechanisms are responsible for plastic deformation in crystals: *slip*, which occurs when one part of the crystal becomes displaced along a particular crystallographic plane, and *twinning*, which occurs when one part of the crystal reorients itself as the mirror image of the remaining crystal. Crystalline slip is the most common plastic deformation mechanism in crystals and is described by the dislocation theory, based on the fact that slip starts from structural defects within the crystal lattice.

The exact underlying mechanisms that produce plastic deformation in viscoelastic materials, especially in amorphous polymers, are still not well understood. However, molecular dynamics simulations suggest that stress-induced mobility, which is related to transitions at the molecular level between different conformations of the polymer chains, produces the glass-to-liquid transition where plastic deformation occurs [26].

Three different material behaviors are observed in force-distance curves acquired by AFM: ideally elastic, ideally plastic, and elasto-plastic. The latter represents the most common case. These three behaviors are ideally shown in Fig. 2.6 without considering adhesion. In the ideally elastic behavior, the approach and withdrawal curves overlap and the material recovers its original shape after unloading. In the ideally plastic behavior, the material does not regain its original shape when the applied load is decreased, and a plastic indentation δ_p equally to the maximum penetration depth remains. In the elasto-plastic behavior, the force of the unloading curve is less than that of the loading curve for the same indentation depth; the remaining indentation after unloading (δ_{ep}) is denominated as "zero load plastic deformation", while the indentation depth that the material recovers (δ_e) is referred to as "zero load elastic deformation".

AFM indentation experiments have been thoroughly studied using molecular dynamics experiments [27]. However, the exact deformation mechanisms in nanoscratching (tip indentation followed by lateral displacement) have not been investigated in detail. The few studies that have been carried out are restricted to the nanoscratching of metals [28, 29] and Si(100) [30] using molecular dynamics simulations. These studies have established that nanoscratching leads to the
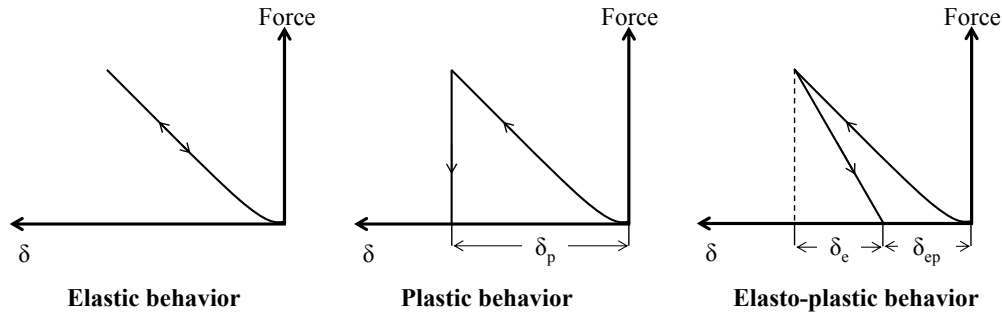
Figure 2.6: Applied load vs. indentation in approach and withdrawal curves for three different material behaviors: ideally elastic (left panel), ideally plastic (center panel), and elasto-plastic (right panel).

formation of surface and bulk dislocation, and that it also produces substantial changes in the properties of the scratched surfaces.

2.3 Nanoscale manipulation methods by AFM

2.3.1 Mechanical nanomachining

AFM-based mechanical nanomachining is a straightforward and powerful method for the controlled manipulation of surfaces, and was quickly understood as such by Jung *et al.* in 1992 [31]. In AFM based mechanical nanomachining the loading force is increased beyond the plastic deformation limit of the material. Four different methods are available for AFM mechanical nanomachining:

Force-distance curve indentation: this method consists of the application of an increasing load on a single point of the surface. Above a threshold load, plastic deformation is produced. This method is not commonly used for the nanofabrication of structures, but it represents a useful technique for the determination of local hardness and Young´s moduli of surfaces [32].

Static plowing lithography: in this method, a constant load above the plastic deformation limit is applied onto the sample while the sample is moved in respect to the tip. This method is also referred to as nanoscratching. This is a simple method that has found many different applications. However it has been claimed that lateral forces during scratching diminish the quality of the lithographed features [31, 33, 34, 35]. Nanoscratching has been also used to fabricate and study local changes of surface properties [36], and to investigate microwear [37] and scratch resistance of coatings [38].
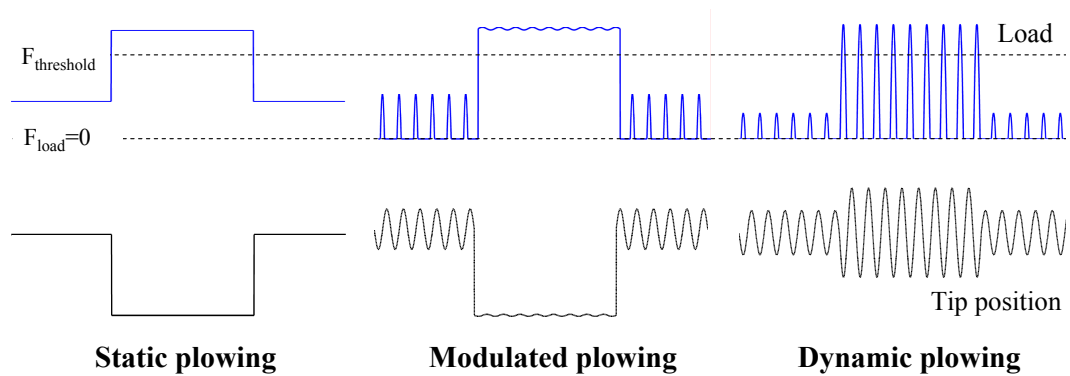
Figure 2.7: Schematic representation of tip position (lower curves) and applied load (upper curves) in the three different AFM based lithography methods. The two dotted lines mark the zero load point and the threshold load for plastic deformation respectively.

Modulated plowing lithography: in order to minimize lateral forces during the lithography process, the plowing force can be modulated. This method is usually combined with tapping mode imaging. To perform lithography, the tip-sample distance is reduced while maintaining cantilever modulation. In this way, the AFM tip is in permanent contact with the sample surface but the applied load during plowing is modulated.

Dynamic plowing lithography[2]: in this method, the oscillation amplitude of the cantilever excitation signal is increased to overcome the threshold load for plastic deformation of the sample while the manipulation path is being executed. This method is easily combined with tapping mode imaging, since it does not require an average displacement of the cantilever base as in the previous methods, but merely an increase of the cantilever excitation signal. During the lithography process, similar to tapping imaging, the cantilever is only in intermittent contact with the sample surface.

The transient tip positions and applied loads for the three described lithography methods are depicted in Fig. 2.7.

AFM mechanical nanomachining has been demonstrated on a wide variety of materials including metals [39], semiconductors [40], polymers [41] or biomaterials [34]. Selective removal of superficial layers to study the internal structure of

---

[2]In literature, both presented non-static methods for lithography are referred to as dynamic plowing lithography. However, as we will see in Chapter 6, the methods not only differ in their realization and dynamic properties, but also yield quite different results and must hence be differentiated.

biological specimens has been achieved, revealing the internal structure of collagen [42] or of a bacterial cell wall [43]. Mechanical nanomanipulation can also be used to extract minute quantities of biomaterial for subsequent chemical analysis [44].

2.3.2 Miscellaneous methods

Several other methods without mechanical contact have been proposed for the local manipulation of surfaces by AFM. One powerful patterning strategy is local anodic oxidation. The local growth of an oxide layer is induced by the application of an electric current between tip and sample surface. The water meniscus, always present between tip and sample under ambient conditions, acts as the electrolyte. Electronic devices such as nanowires, metal-oxide field effect transistors (MOSFET), single-electron transistors and quantum point contacts have already been fabricated by this method [45]. The control of the growth direction of organic molecule monolayers with conducting properties is a basic issue for the development of molecular electronic devices that could be solved using a silicon oxide template fabricated by means of local anodic oxidation [46].

Chemical surface manipulation by AFM nanolithography can be achieved by adding molecules to the surface, e.g. by dip pen nanolithography [47] or by substitution of surface components. In substitution lithography (nanografting and nanoshaving), self-assembled monolayers are removed by means of mechanical desorption by the AFM tip followed by in-situ replacement of a second component [48].

A new promising approach for the modification of thin polymer films is AFM-assisted electrostatic lithography (AFMEN). In this technique, lithography is performed by simply biasing the conductive AFM tip and the grounding substrate of the polymer film. Depending of the applied voltages, the polymer can be either raised or ablated away due to a combination of Joule heating and electrostrostatic pressure generation in the polymer [49].

Chapter 3

Transfer function analysis of free and surface-coupled AFM cantilever dynamics[1]

The dynamic operation of the AFM has emerged as a standard method both for imaging and manipulation. There are several different approaches to model the dynamics of an AFM cantilever. The most straightforward method relies on modeling the cantilever as a single-degree-of-freedom harmonic oscillator, the so-called first mode approximation (FMA) [50]. However, the first mode approximation neglects that the cantilever is a distributed parameter system with an infinite number of resonant frequencies. The equation of motion of the AFM cantilever can be solved by analytical methods [51]. The cantilever also may be modeled as a lumped parameter system [52] parting from the analytical solution. However, if damping or tip-sample interaction are to be considered, the solution of the problem is not trivial [53].

Here, an analytical transfer function analysis of a generic cantilever beam may provide additional insight. This analysis method has successfully been applied to study the dynamics of flexible structures [54]. From the transfer function it is straightforward to obtain the frequency response, modes of vibrations and step response of the system. Transfer functions of distributed parameter systems are transcendental functions[2], and therefore, in order to obtain system poles and zeros infinite product expansions must be used [55]. The analysis of poles and zeros facilitates the study of consequences in modeling and control design of the different

---

[1]This chapter has been partly published in: F. J. Rubio-Sierra, R. Vázquez, and R. W. Stark (2006) *Transfer function analysis of the micro-cantilever used in atomic force microscopy*, IEEE Transactions on Nanotechnology, accepted for publication.

[2]Transcendental functions are those which are not an algebraic function, i.e, a function which cannot be expressed in terms of algebra. Exponential and trigonometric functions, along with their inverse functions, are examples of transcendental functions.

inputs and outputs of the system [56].

In this chapter, the dynamics of a generic rectangular AFM cantilever is analyzed by the transfer function method. For the sake of clarity and due to its importance for AFM operation and sensing applications [57], we consider at first the uncoupled cantilever. Then we illustrate the influence of surface coupling in the system dynamics considering a (linearized) variable surface coupling, which includes the free end as a limiting case, as well as the pinned case. For both considered cases, analytical expressions of the transfer function for different system configurations are derived and the corresponding frequency responses are studied. Poles and zeros, which have important implications both for system stability and behavior, are obtained from the infinite product expansion of the transfer functions. Using the analytical expression of the transfer function, the resonant and antiresonant responses of the different configurations are examined. Point and distributed force actuation of an AFM cantilever are studied along with the implications of tip deflection or slope measurement. This distinction between deflection or slope is important since their sensitivity differs numerically in each of the vibration modes [52]. Finally, the step response of the AFM cantilever for the different system configurations is discussed. For the surface coupled cantilever, the influence of the contact stiffness on the frequency response, non-minimum phase behavior, stability, and controllability of the system is studied in detail. From the transfer function study, important conclusions on AFM dynamic operation for high resolution imaging and surface modification are obtained.

3.1 Dynamic description of the system

3.1.1 Transfer function of a dynamic system

The transfer function of a linear physical system with an input $v(t)$ and output $y(t)$ is defined by

$$G(s) = \frac{V(s)}{Y(s)}, \tag{3.1}$$

where $V(s)$ and $Y(s)$ are the Laplace transformed functions in the complex variable s of the system input and output, respectively:

$$V(s) = \mathcal{L}\{v(t)\} = \int_0^\infty e^{-st} v(t) dt, \tag{3.2}$$

$$Y(s) = \mathcal{L}\{y(t)\} = \int_0^\infty e^{-st} y(t) dt. \tag{3.3}$$

To obtain the transfer function of a linear dynamic system the differential equations describing the system have to be Laplace transformed. The solutions of

the Laplace transformed equations are straightforward and from these the transfer function is obtained. The response of the system in the positive time domain to any given input is obtained by applying the inverse Laplace transform

$$v(t) = \mathcal{L}^{-1}\{v(s)\} = \mathcal{L}^{-1}\{G(s)Y(s)\} = \frac{1}{2\pi i} \int_{c-i\infty}^{c+i\infty} e^{st} G(s) Y(s) ds, \qquad (3.4)$$

where i is the imaginary unit.

Of special interest for the study of stability and controllability of a dynamic system are the zeros and poles of the transfer function. The zeros and poles of the system are the complex solutions of the numerator and denominator when equalled to null respectively.

3.1.2 AFM cantilever system

The micro-cantilever can be described by a transfer function representation by considering the cantilever as an isolated input/output (I/O) system that is linear and time invariant. The inputs and outputs of the system to be considered in this work are the following:

Input 1 accounts for forces acting at the free end of the cantilever; these forces may be the interaction forces between tip and sample or a magnetic excitation realized by attaching a magnetic particle at the free end of the cantilever which is subject to a strong time varying magnetic field gradient [58]. Input 2 is a distributed uniform force along the cantilever; this corresponds to the inertial force caused by the usual mechanical excitation by a piezoelectric transducer below the cantilever chip [59] or to an electrostatic force.

Output 1 is the vertical deflection of the free end of the cantilever, usually measured by interferometric methods [8]. Output 2 is the deflection slope at the free end of the cantilever. This is the output measured in most of AFM systems using the light lever detection method [60].

In the next sections we will consider the following system configurations: (i) case 11, i.e. only input 1 and output 1; (ii) case 12, i.e. only input 1 and output 2; (iii) case 21, i.e. only input 2 and output 1; (iv) case 22, i.e. only input 2 and output 2.

The I/O system configuration considered is depicted in Fig. 3.1. It is worth noting that other inputs and outputs could be easily included into the system description by using the same tools presented in this chapter.

3.1.3 Tip-Surface interaction

The surface interaction force that acts on the tip of the cantilever is a non-linear function that depends mainly on the proximity of the tip to the sample [27] (see
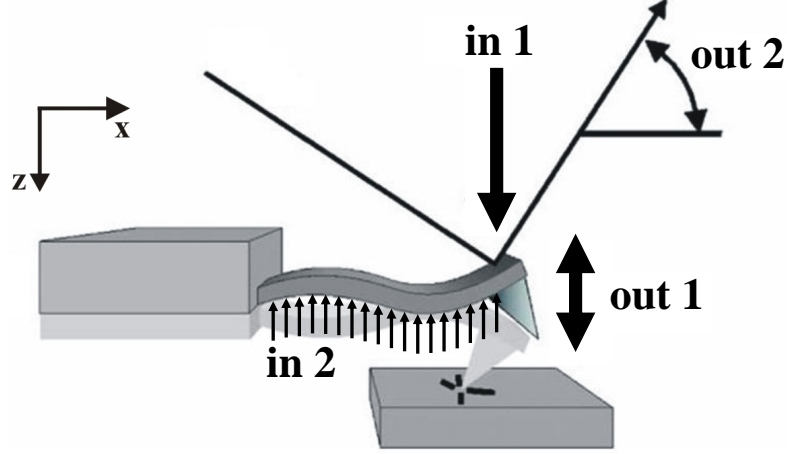
Figure 3.1: Schema of the inputs and outputs of the AFM system considered. Input 1 is a force applied at the cantilever fixed end. Input 2 is the position of the fixed end. Output 1 is the cantilever tip position. Output 2 is the slope at the end of the cantilever.

§ 2.2.1). If $z_{\mathrm{s}}(t)$ is the distance from the sample to the free end of the undeflected cantilever, the true tip-surface distance neglecting sample deformation is given by $z_{\mathrm{s}}(t) - z(L, t)$, where L is the length of the cantilever. Denominating $f(t)$ as the tip-surface interaction force, and a_0 the inter-atomic distance, one can characterize two regimes of behavior. If $z_{\mathrm{s}}(t) - z(L, t) \geq a_0$, the force is attractive and can be described by a van der Waals model,

$$f(t) = -\frac{HR}{6(z_{\mathrm{s}}(t) - z(L, t))^2}. \tag{3.5}$$

If $z_{\mathrm{s}}(t) - z(L, t) < a_0$, the interaction is repulsive and can be computed using the DMT [61] model (see § 2.2),

$$f(t) = -\frac{HR}{6a_0^2} + \frac{4}{3}E^*\sqrt{R}(z_{\mathrm{s}}(t) - z(L, t) + a_0)^{3/2}. \tag{3.6}$$

In (3.5) and (3.6), H represents the Hamaker constant, R the tip radius and E^* the reduced Young´s modulus defined in (2.8). For the transfer function analysis, we will consider the case in which the system stays in the close neighborhood of an equilibrium setpoint z_0, which can be adjusted by moving the sample relative to the cantilever base [62]. Linearizing the force around the set point, we obtain

$$f(t) = -k_{\mathrm{ts}}z(L, t), \tag{3.7}$$

where

$$k_{\mathrm{ts}} = -\left.\frac{\partial f(t)}{\partial z(L, t)}\right|_{z_0} \tag{3.8}$$

represents the effective force constant. Inserting (3.5) and (3.6) into (3.7), we find

$$k_{\text{ts}} = \begin{cases} -HR/3(z_{\text{s}}(t) - z_0)^3, & \text{if } z_{\text{s}}(t) - z(L,t) \geq a_0, \\ 2E^*\sqrt{R(z_{\text{s}}(t) - z_0 + a_0)}, & \text{if } z_{\text{s}}(t) - z(L,t) < a_0. \end{cases} \qquad (3.9)$$

Note that the sign of k_{ts} depends on the regime of the force. For the attractive regime, the constant is negative, while for the repulsive regime the constant is positive. We consider

$$k_{\text{ts}} = \frac{3EI}{L^3}\hat{k}_{\text{ts}}, \qquad (3.10)$$

where E is the Young modulus and $I = wd^3/12$ is the area moment of inertia and the quantity $3EI/L^3$ corresponds to the cantilever spring constant. Thus $\hat{k}_{\text{ts}}$ is the parameter that determines the magnitude and regime of the force.

This linear approximation can be extended to other force models of the tip-surface interaction. For the case where the tip of the cantilever is attached to a surface through a glued molecule, as in the acquisition of force spectroscopy curves, the effective force constant is given by the force constant of the attached molecule [63]. In this work we consider all possible values of $\hat{k}_{\text{ts}}$ including zero (free end) and infinity (pinned end).

3.1.4 Dynamic model of the AFM system

For the case of a generic rectangular beam the dynamics can be derived by using the classical Euler-Bernoulli beam model neglecting rotary inertia, shear deformation, axial effects and tip mass:

$$E\,I\,z_{xxxx}(x,t) + c\,\dot{z}(x,t) + m\,\ddot{z}(x,t) = -u(t), \qquad (3.11)$$

where the subindex x denotes the partial derivative with respect to the distance $(\partial/\partial x)$ and the dot differentiation with respect to time $(\partial/\partial t)$. The function $z(x,t)$ is the transversal displacement of the cantilever relative to its support, $u(t)$ is a uniform force per unit length acting along the cantilever, such as an inertial force caused by cantilever base displacement [51], t denotes the time, $x \in (0,L)$ the longitudinal position along the cantilever, EI the flexural stiffness, c is the damping factor, and m the mass per unit length. Note that the damping factor corresponds to, firstly, the intrinsic damping and , secondly, the damping caused by the surrounding media. If the cantilever base is not moved, then both damping factors are combined in c. For the special case where the cantilever base is moved to induce cantilever vibrations, then a first order approach must be assumed [64] and the damping factor in (3.11) is given by $c(\dot{z}(x,t) + \dot{z}_{\text{b}}(t))$, where $z_{\text{b}}(t)$ corresponds to the position of the cantilever base.

The boundary conditions at the fixed end of the tip are zero deflection and zero slope, namely,

$$z(0,t) = 0, \ z_x(0,t) = 0. \tag{3.12}$$

At the free end no torque is considered,

$$z_{xx}(L,t) = 0, \ EIz_{xxx}(L,t) + f(t) = -q(t), \tag{3.13}$$

where we have included both the interaction force $f(t)$ and the input force $q(t)$. Introducing the linearized force (3.7) and (3.10) in (3.13) yields

$$EI\left(z_{xxx}(L,t) - \frac{3\hat{k}_{\text{ts}}}{L^3}z(L,t)\right) = -q(t). \tag{3.14}$$

In order to obtain a transfer function description of the system we take Laplace transform on (3.11), disregarding initial conditions,

$$E\,I\,Z_{xxxx}(x,s) + (c\,s + m\,s^2)\,Z(x,s) = -U(s), \tag{3.15}$$

where $Z(x,s)$ and $U(s)$ respectively represent the Laplace transform of the cantilever transversal position and the distributed force along the cantilever, and s is the (complex) Laplace variable. The boundary conditions in the Laplace domain are given by

$$Z(0,s) = 0, \qquad\qquad\qquad Z_x(0,s) = 0,$$

$$Z_{xx}(L,s) = 0, \qquad E\,I\left(Z_{xxx}(L,s) - \frac{3\hat{k}_{\text{ts}}}{L^3}Z(L,s)\right) = -Q(s), \tag{3.16}$$

where $Q(s)$ is the Laplace transform of the force at the free end of the cantilever.

Equation (3.15) can be solved using the theory of linear ordinary differential equations [65]. We define

$$\lambda(s) = \sqrt[4]{\frac{c\,s + m\,s^2}{4E\,I}}. \tag{3.17}$$

In the following, we will omit the dependence of λ on s for simplicity of notation. The solution for the homogeneous equation is

$$Z_{\text{h}}(x,s) = e^{\lambda x}[C_1\sin(\lambda x) + C_2\cos(\lambda x)] + e^{-\lambda x}[C_3\sin(\lambda x) + C_4\cos(\lambda x)], \tag{3.18}$$

where the constants C_1, C_2, C_3 and C_4 can be found substituting (3.18) into the boundary conditions (3.16). For the non-homogeneous case, the general solution is of the form

$$Z(x,s) = Z_{\text{h}}(x,s) + W(x,s), \tag{3.19}$$

where $W(x, s)$ is a particular solution of the non-homogeneous equation. For the first force input we define the transfer function from the point force to cantilever deflection, G_{11}, and from the point force to cantilever slope, G_{12} as[3]

$$G_{11}(L, s) = \frac{Z(L, s)}{Q(s)}, \; G_{12}(L, s) = \frac{Z_x(L, s)}{Q(s)}, \quad (3.20)$$

where $U(s) = 0$ is considered. Likewise, we define for the second input the transfer function from the distributed force to cantilever deflection, G_{21}, and from distributed force to cantilever slope, G_{22}, as

$$G_{21}(L, s) = \frac{Z(L, s)}{U(s)}, \; G_{22}(L, s) = \frac{Z_x(L, s)}{U(s)}, \quad (3.21)$$

considering $Q(s) = 0$.

For the special case where the cantilever base is moving, the environmental damping has to be considered in the Bernoulli equation as mentioned above. For this case, the moving base introduces a multiplying factor in the transfer functions calculated from (3.11). The transfer function considering a moving base, and using the transfer function of the unmoved base $G_{ij}(s)$, is then given by[4]:

$$G'_{ij}(s) = G_{ij}(s) \frac{s + c/m}{s}. \quad (3.22)$$

Once the transfer function has been calculated, it is straightforward to obtain the frequency response of the system. At a given angular frequency ω, the response amplitude is given by $|G(j\omega)|$, while the phase response is given by $\angle G(j\omega)$; that is, the modulus and phase angle of the complex-valued function $G(s)$ evaluated on the imaginary axis. The frequency response of the cantilever at a given point can then be displayed using the Bode plot representation [66].

All numerical data and plots obtained from the transfer functions in this chapter have been calculated using the following parameters of a typical commercial cantilever[5]: $E = 169$ GPa, $m = 4.08 \times 10^{-7}$ kg/m, $L = 232$ μm, $w = 40$ μm, $d = 4$ μm, and $c = 0.01$ kg/ms, where w and d are cantilever width and thickness, respectively.

---

[3]Matrix notation is the standard notation used in system dynamics literature for multiple input multiple output (MIMO) systems. However, in this work the different transfer functions will be presented separately to remark their physical meaning.

[4]This is found by considering the equation of motion (3.11) using an inertial frame of reference and including the base motion as in [53].

[5]Data provided by Nanoworld AG, Erlangen Germany.

3.2   Freely vibrating AFM cantilever

First, we will consider the transfer function study of the surface uncoupled AFM cantilever, i.e. $\hat{k}_{ts} = 0$. The freely vibrating cantilever case illustrates dynamic aspects that are obscured by the surface interaction and, additionally, the free cantilever case study is an important theoretical tool for AFM based sensor applications.

3.2.1   First case: point force at the free end

In the first case we consider that the system input is a point load $q(t)$ acting at the free end of the cantilever without distributed forces ($u(t) = 0$). To obtain the solution of the equation of motion, it is only necessary to substitute the boundary conditions (3.16) in the homogeneous solution (3.18), thus obtaining a linear system of equations in the constants C_1, C_2, C_3, and C_4. The solution is then

$$Z^{\mathrm{pt}}(x, s) = \frac{-2Q(s)}{E\,I\lambda^3 D(s)} \times$$
$$[\cos(\lambda L)\,\cosh(\lambda\,(L-x))\,\sin(\lambda x) - \cos(\lambda\,(L-x))\,\cosh(\lambda x)\,\sinh(\lambda x)],$$
$$(3.23)$$

where
$$D(s) = 2[2 + \cos(2\lambda L) + \cosh(2\lambda L)]. \tag{3.24}$$

The transfer function from the punctual force to tip position is obtained by substituting $x = L$ in the previous equation, which gives

$$G_{11}(L, s) = \frac{\sinh(2\lambda L) - \sin(2\lambda L)}{EI\lambda^3 D(s)}. \tag{3.25}$$

To obtain the transfer function $G_{12}(L, s)$ from the punctual force to the cantilever slope at the free end, it is first of all necessary to take the spatial derivative of the solution, and then to make the same substitution as before. The obtained transfer function is

$$G_{12}(L, s) = \frac{\cosh(2\lambda L) - \cos(2\lambda L)}{EI\lambda^2 D(s)}. \tag{3.26}$$

The Bode plots for both transfer functions are shown in Fig. 3.2. The dynamic response for both outputs presents alternating resonances and antiresonances. The resonances are located at the same frequencies for both outputs due to the common denominator. The antiresonance frequencies are different for both cases. At the resonances the phase decreases by 180°, whereas at the antiresonances the phase is increased by 180°.
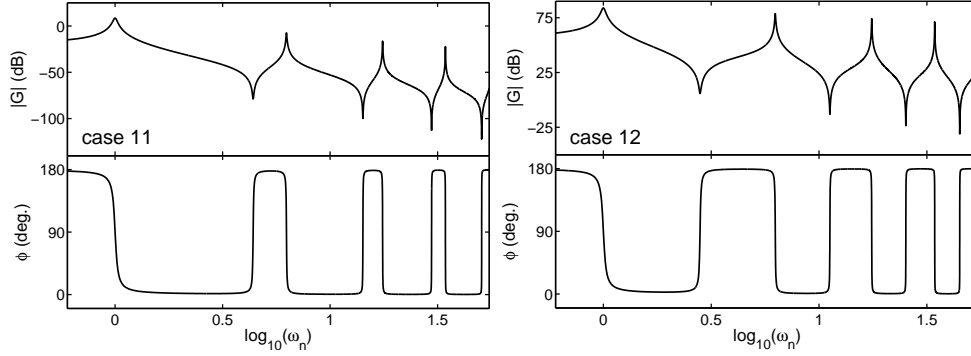
Figure 3.2: Bode plot of the response of a cantilever to a point force applied at its end. The frequency ω_n has been normalized with respect to the first resonant frequency of the system.

3.2.2 Second case: distributed force

Next we consider the case where the cantilever is solely driven by a distributed force and $q(t) = 0$ (no point force input). In this case, (3.15) is non-homogeneous. A particular solution is given by

$$W(x, s) = \frac{U(s)}{c\,s + m\,s^2}.\tag{3.27}$$

Again, we substitute the general solution into the boundary conditions (3.16) to obtain the coefficients from (3.19). The solution is

$$
\begin{aligned}
Z^{\text{dist}}(x, s) = \frac{-U(s)}{2EI\lambda^4 D(s)} \times \\
[D(s) - (\cosh(\lambda(2L - x)) + 2\cosh(\lambda x))\cos(\lambda x) \\
- \cosh(\lambda x)\cos(\lambda(2L - x)) + \sinh(\lambda x)\sin(\lambda(2L - x)) \\
+ \sinh(\lambda(2L - x))\sin(\lambda x)].
\end{aligned}\tag{3.28}
$$

The transfer function from the distributed force per unit length to the tip position is

$$G_{21}(L, s) = \frac{-1}{E\,I\,\lambda^4}\frac{[\cosh(\lambda\,L) - \cos(\lambda\,L)]^2}{D(s)}.\tag{3.29}$$

Again, by spatial differentiation of the solution we obtain the transfer function for the second output,

$$G_{22}(L, s) = -2\frac{\cosh(\lambda L)\sin(\lambda L) - \cos(\lambda L)\sinh(\lambda L)}{EI\lambda^3 D(s)}.\tag{3.30}$$
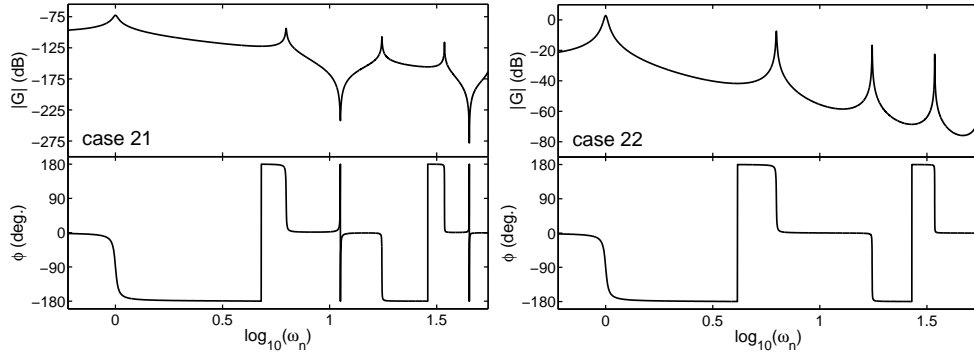
Figure 3.3: Bode plot of the response of a cantilever to a distributed force. Sharp edges at the position response represent phase increments of 360°; in the slope response, the sharp edges are due to the continuity of the phase between -180° and 180°. The frequency ω_n has been normalized with respect to the first resonant frequency of the system.

The frequency response for both transfer functions is shown in Fig. 3.3. The denominators of both transfer functions are the same as for the point load. Therefore, the resonances are located at the same frequencies. The antiresonances of the position frequency response alternate each two resonance peaks, while there are no antiresonances in the slope response. At the antiresonances of the position response, there is a phase increment of 360° (sharp edges at the phase diagram). In the slope response, there is a decrease of 90° at the resonances.

Note from (3.25), (3.26), (3.29) and (3.30) that the poles of the cantilever transfer function are the same for both inputs and outputs considered and do not depend on the actuator and sensor position as is usual in dynamical systems: the location of sensors and actuators can change the position of zeros, but not the denominator (the poles), which are "inherent" to the dynamics of the system.

3.2.3   Poles of the transfer function

The common denominator $D(s)$ can be factorized by direct application of the infinite product expansions table given in Goodson [55] and by using some trigonometric relations. The result is

$$D(s) = 8 \prod_{n=1}^{\infty} \left[1 + \frac{4\lambda^4 L^4}{c_n^4} \right],$$

$$\cos c_n \cosh c_n = -1, \ c_n > 0, \ \text{real}.$$

(3.31)

The s-plane roots of $D(s)$ are the poles of the system, the characterization of which is important for control analysis and to obtain an expression for all the

resonant frequencies of the system. By substitution of (3.17) in (3.31), the fourth power of λ in (3.31) reduces the fourth root in (3.17) and we find, for each n, a (simple) complex conjugate pair of imaginary poles in the s-plane,

$$s_n^{\text{pole}} = -\frac{c}{2m} \pm \sqrt{\frac{c^2}{4m^2} - \frac{E\,I\,c_n^4}{m\,L^4}}. \qquad (3.32)$$

All the poles are located in the left half plane (LHP) which means that the damped cantilever is stable. The numerical values for the first three conjugate pairs are:

$$\begin{aligned}
s_1^{\text{pole}} &= -13.4 \times 10^3 \pm 0.64 \times 10^6 i \ \ (\text{rad/s}), \\
s_2^{\text{pole}} &= -13.4 \times 10^3 \pm 4.02 \times 10^6 i \ \ (\text{rad/s}), \\
s_3^{\text{pole}} &= -13.4 \times 10^3 \pm 1.12 \times 10^7 i \ \ (\text{rad/s}).
\end{aligned} \qquad (3.33)$$

A resonant frequency corresponds to each complex conjugate pair of poles. Note that if base motion is being considered, then (3.22) introduces an additional pole at $s = 0$.

An analytical expression for each resonant frequency is not easy to obtain from the value of the poles, but since the damping of each pole (the negative real part) is very small (compared to the modulus of the pole), it can be considered to be approximately at the imaginary part of the conjugate pair of poles:

$$f_n^{\text{res}} = \frac{Im(s_n)}{2\pi}. \qquad (3.34)$$

For our case study, the first three resonant frequencies of the system are: 102 kHz, 640 kHz, and 1.79 MHz.

3.2.4 Amplitude and phase lag along the cantilever

Once the resonant frequencies are known, it is straightforward to obtain the amplitude and phase response of the transfer function along the cantilever in the natural modes of vibration using (3.23) and (3.28). The amplitude and slope response in the first three natural modes for all case studies are shown in Fig. 3.4. The amplitude response for both inputs is equivalent while they differ in the phase response. Resonant modes of vibration are of great importance for AFM measurements since they enable frequency and amplitude modulated operation of the cantilever [67]. From the resonant response of the cantilever it is observed that the gradient of the response at the end part of the cantilever, where system output is measured in standard AFM systems, is smaller for the second output, which enhances system output stability against internal drift of the microscope components.

Due to the finite velocity of propagation of the bending waves along the can-
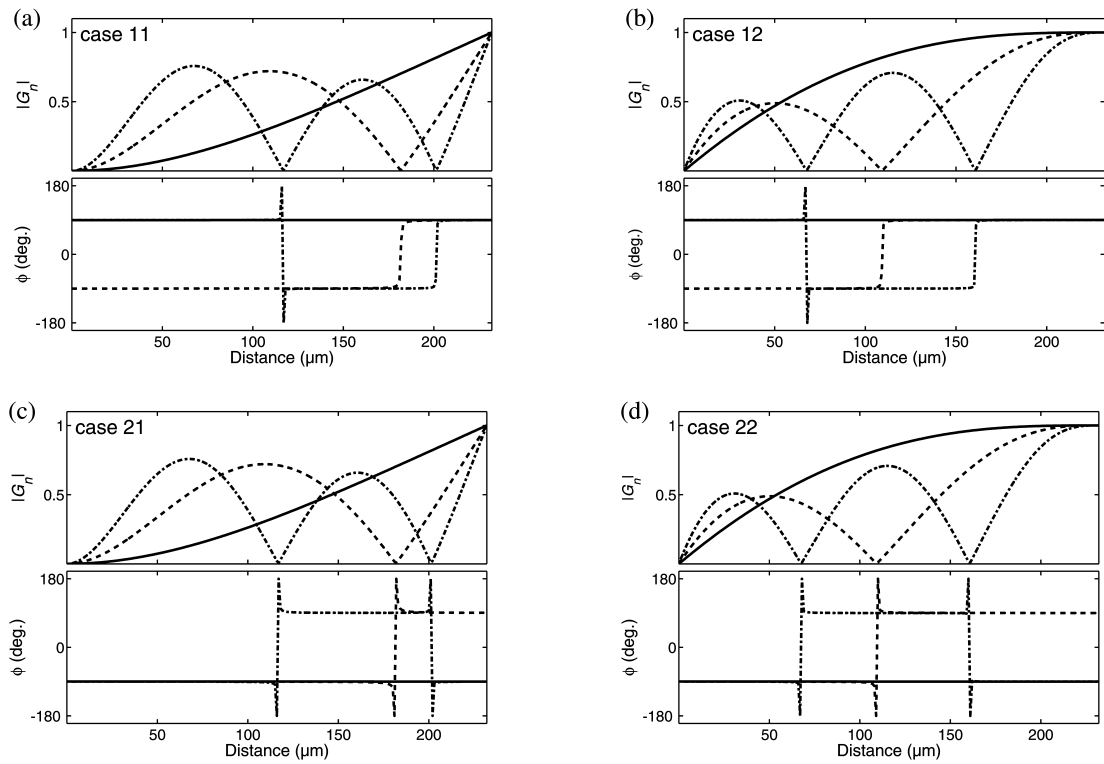
Figure 3.4: Magnitude and phase response along the cantilever at the first three resonant frequencies: (a) case 11, (b) case 12, (c) case 21, and (d) case 22. The magnitude $|G_n|$ has been normalized to the maximum of each mode.
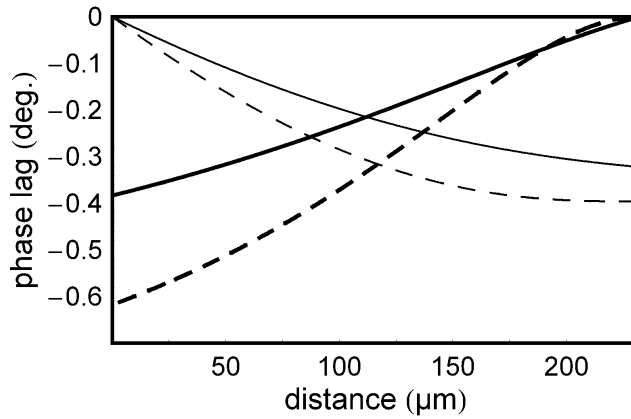
Figure 3.5: Phase lag along the cantilever for the four different cases in the first flexural mode of resonance: thick solid line, case 11; thick dashed line, case 12; thin solid line, case 21; thin dashed line, case 22.

tilever, there is a phase variation between the resonance nodes. The phase lag is given by

$$\Delta\phi = -\frac{\omega\Delta x}{\nu}, \qquad (3.35)$$

where $\Delta\phi$ is the change in phase of the bending wave traveling a distance Δx with propagation velocity ν. The velocity of propagation is not constant because of the dispersive nature of the flexural vibrations of the cantilever [51]. Fig. 3.5 shows the phase lag along the cantilever for the different inputs and outputs when the cantilever is excited in its first flexural mode of resonance. As expected, for the point load case the phase lag increases from the free end of the cantilever to its base, opposite to the direction in the distributed force case.

3.2.5 Zeros of the transfer function

Factorization of the numerators of (3.25), (3.26), (3.29), and (3.30) is practically impossible except in the case where $x = L$. In this case, transcendental functions whose product expansions are found in literature [55] can be easily obtained either directly or after the use of some trigonometric relations. The infinite product expansions of the four different transfer functions are:

$$G_{11}(L, s) = \frac{8L^3}{3EID(s)} \prod_{n=1}^{\infty} \left[1 + \frac{4\lambda^4 L^4}{d_n^4} \right], \qquad (3.36)$$

$$G_{12}(L, s) = \frac{4L^2}{EID(s)} \prod_{n=1}^{\infty} \left[1 + \frac{4\lambda^4 L^4}{n^4 \pi^4} \right], \qquad (3.37)$$

$$G_{21}(L, s) = \frac{-L^4}{EID(s)} \left(\prod_{n=1}^{\infty} \left[1 + \frac{\lambda^4 L^4}{4n^4 \pi^4} \right] \right)^2, \qquad (3.38)$$

$$G_{22}(L, s) = \frac{-4L^3}{3EID(s)} \prod_{n=1}^{\infty} \left[1 - \frac{\lambda^4 L^4}{d_n^4} \right], \qquad (3.39)$$

where

$$\tan d_n = \tanh d_n, \;\; d_n > 0, \;\; \text{real}. \qquad (3.40)$$

From these expressions it is straightforward to obtain an exact numerical expression for the zeros of the transfer functions, proceeding similarly as when we obtained the poles of the transfer function. Fig. 3.6 shows a graphical representation for the first three pairs of zeros of each output of both case studies. In this figure it is clearly seen that the transfer functions corresponding to cases 11, 12, and 21 have all their complex conjugate pairs of zeros in the LHP. For case 22, the complex conjugate pairs of zeros are all in the real axis and alternate in the LHP and right half plane (RHP).

The point load configuration corresponds to a system where the measurement is collocated (sensor and actuator in the same position). Therefore, it was expected to find all the zeros of the system in the LHP. This has important repercussions for the dynamics and control of the cantilever: if no zeros are present in the RHP, it is easier to stabilize the system and modal truncation accurately simulates the dynamics of the distributed system [52].

The configuration for the second input is non-collocated (sensors and actuators in different position). The position measurement (case 21) does not have RHP poles, and therefore is a minimum phase system. However, as shown in the Bode plot of Fig. 3.3, the phase contribution exceeds -180° after each two resonant frequencies and recovers 360° in the antiresonant frequency. This must be taken into account for control design. The system where the slope is used as output (case 22) suffers from presence of RHP zeros and after the first resonance the phase contribution always exceeds -180°. Hence its transfer function is non-minimum phase. Therefore, in this configuration the system is subject to performance limitations and is more difficult to control than in the other considered configurations [56].

For the special case where cantilever base motion is present in the system, then (3.22) introduces an additional zero at $s = -c/m$, i.e. a LHP zero which does not modify the quantitative analysis of the system presented above.

3.2.6   Antiresonant cantilever response

Once the infinite product expansions for the different transfer functions have been calculated, it is possible to obtain an approximation to the antiresonant frequencies
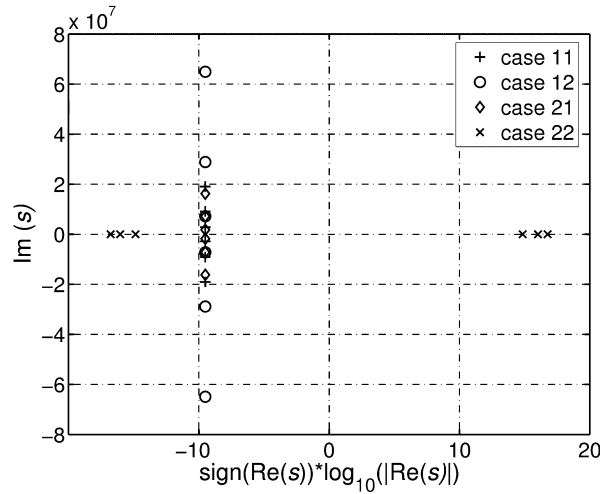
Figure 3.6: First three complex conjugate zeros of the four different transfer functions from (3.36), (3.37), (3.38) and (3.39).

Case 11	Case 12	Case 21
448 kHz	287 kHz	197 kHz
1.45 MHz	1.15 MHz	4.72 MHz
3.03 MHz	2.58 MHz	10.6 MHz

Table 3.1: First three antiresonant frequencies of the different system configurations calculated from the transfer function. Case 22 does not have antiresonances and is therefore omitted.

from the imaginary part of each complex conjugate pair of zeros (with non-zero imaginary part). Different from the resonant frequencies, each system configuration has different values of the antiresonant frequencies. Table 3.1 shows the values of the first three antiresonant frequencies for each case. Case 22 does not have any antiresonances (because its numerator does not have any real solution when equalled to null). The first three antiresont modes of vibration for every system configuration are shown in Fig. 3.7.

3.3 Surface coupled AFM cantilever

When surface interaction in our cantilever model ($\hat{k}_{ts} \neq 0$) is considered, (3.11) can be solved following the same methodology as presented above. We skip the long analytical expression of the solution, which can be found by using any commercial
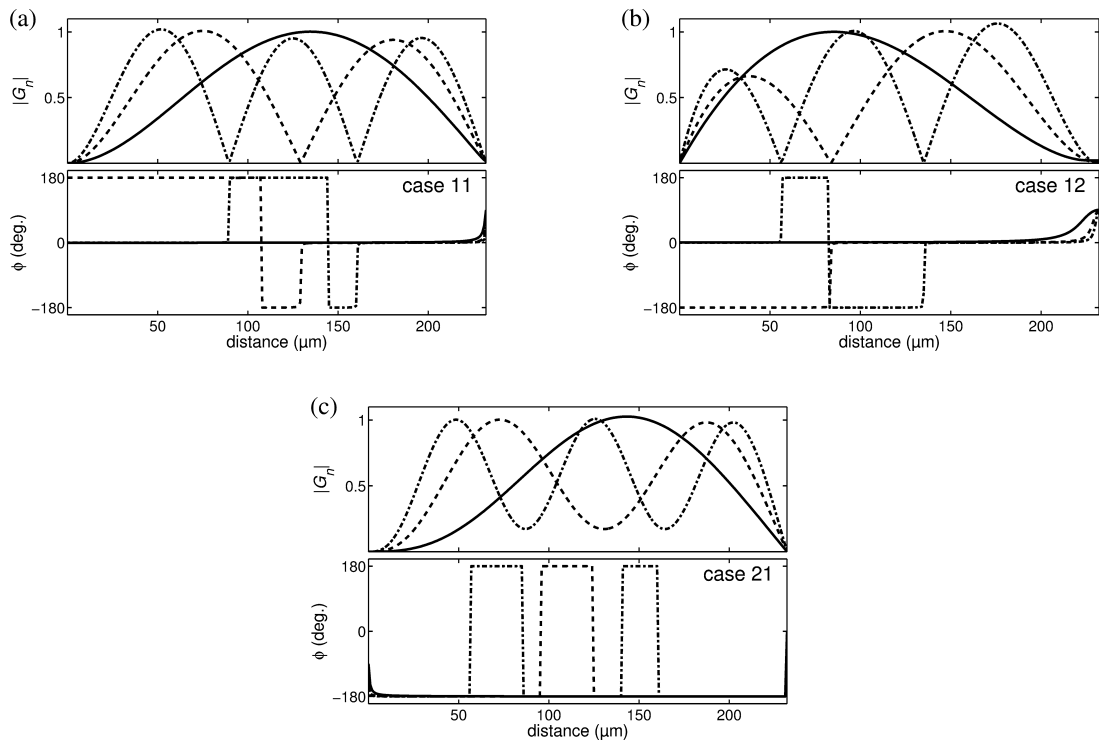
Figure 3.7: Magnitude and phase response along the cantilever at the first three antiresonant frequencies: (a) case 11, (b) case 12, and (c) case 21. The magnitude $|G_n|$ has been normalized to the maximum of each mode.

symbolical calculation package. In the next sections, we will study the critical influence of the tip-surface interaction, parametrized by $\hat{k}_{\text{ts}}$, in the dynamic response of the system.

3.3.1 Transfer functions of the coupled system

By solving the transformed equation of motion (3.15) as in the previous section, we find the expressions for the four different transfer functions considered in § 3.1.2. Again, the different transfer functions for the chosen inputs and outputs share a common denominator,

$$D(s) = 2[2 + \cos(2\lambda L) + \cosh(2\lambda L)] + \frac{3\hat{k}_{\text{ts}}}{L^3\lambda^3}[\sinh(2\lambda L) - \sin(2\lambda L)], \quad (3.41)$$

and the transfer functions are given by:

$$G_{11}(s) = \frac{1}{EID(s)\lambda^3}[\sinh(2\lambda L) - \sin(2\lambda L)], \quad (3.42)$$

$$G_{12}(s) = \frac{1}{EID(s)\lambda^2}[\cosh(2\lambda L) - \cos(2\lambda L)], \quad (3.43)$$

$$G_{21}(s) = \frac{-1}{2EID(s)\lambda^4}[\cos(\lambda L) - \cosh(\lambda L)]^2, \quad (3.44)$$

$$G_{22}(s) = \frac{-2}{EID(s)\lambda^3}[\cosh(\lambda L)\sin(\lambda L) - \cos(\lambda L)\sinh(\lambda L)]$$

$$+ \frac{3\hat{k}_{ts}}{2EID(s)L^3\lambda^6}[\sin(\lambda L) - \sinh(\lambda L)]^2. \quad (3.45)$$

Note that only D and G_{22} depend on $\hat{k}_{\text{ts}}$.

3.3.2 Shift of the frequency response

As stated in § 3.1.4, the frequency response of the system can be obtained using the Bode plot representation of the transfer function. Bode plots are shown in Fig. 3.8 for values $\hat{k}_{\text{ts}}$ = -1, 0, 10, 100. We do not show the frequency response for $\hat{k}_{\text{ts}} < -1$, since that range of values is demonstrated in § 3.3.3 to lead to an unstable system.

The great influence of the magnitude of the contact stiffness on the frequency response of the system is manifested in the Bode plots. The most interesting qualitative feature of the plots is the attenuation and displacement of resonance modes to the right as $\hat{k}_{\text{ts}}$ increases. Note that, as in the previously studied free cantilever system, the phase shift is finite for all the considered cases except the
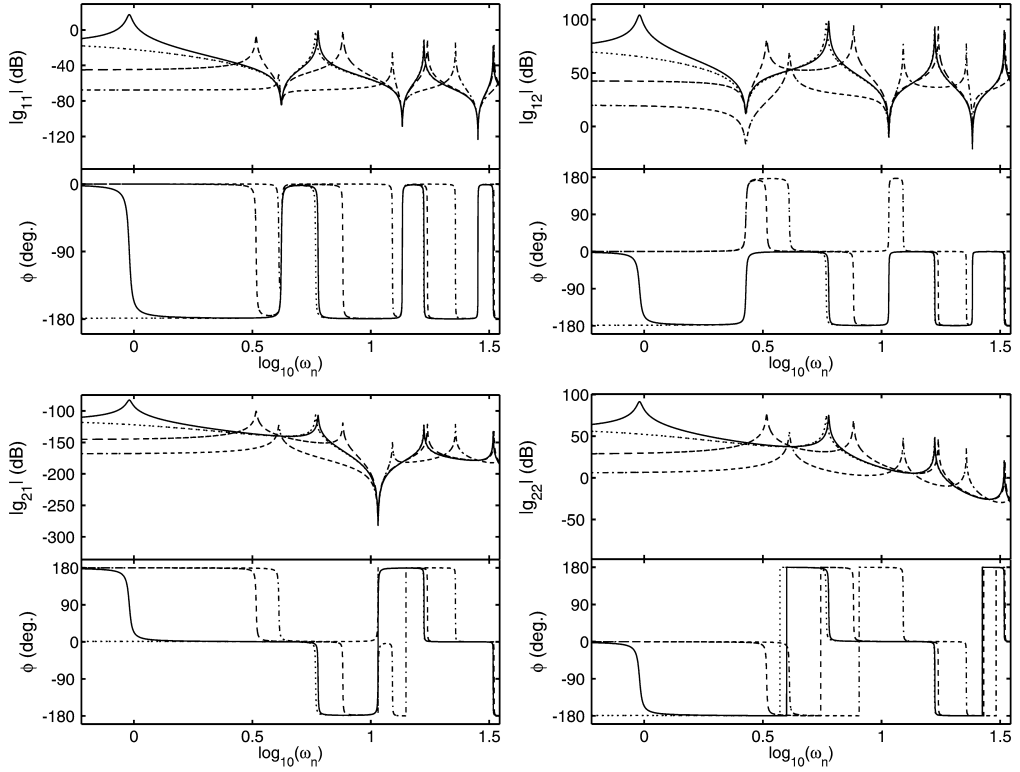
Figure 3.8: Bode plots of the four different transfer functions considering surface coupling (G_{11} top-left, G_{12} top-right, G_{21} bottom-left, and G_{22} bottom-right) for $\hat{k}_{\mathrm{ts}} = -1$, 0, 10, 100 (respectively dotted, solid, dashed, and dash-dotted lines). The sharp edges in the phase shift of G_{22} are due to the continuity from $-180°$ to $180°$.

one corresponding to G_{22}, i.e. these system configurations are minimum phase. For the values of $\hat{k}_{\mathrm{ts}}$ considered in the Bode plot, the phase shift for G_{22} is always incremented and tends to infinity with increasing frequency, i.e. it is non-minimum in phase. In § 3.3.4, it will be shown that this non-minimum behavior arises only for certain values of $\hat{k}_{\mathrm{ts}}$. Note that the position of the antiresonances for all system configurations except for the last case, distributed force with slope output (G_{22}), only depends on the used cantilever and not on the interaction with the surface.

In some cases there are modes of resonance that are strongly attenuated, almost disappearing or exchanging their position with an anti-resonance. This is the effect of a (stable) pole-zero cancellation that happens for certain values of $\hat{k}_{\mathrm{ts}}$. The cancellation may change the behavior of the system dramatically in the frequency range of the disappearing resonance mode. Figure 3.9 shows the first resonance peak for different values of $\hat{k}_{\mathrm{ts}}$ in the point load configuration. For both

Figure 3.9: Shift of the resonance curve for both outputs of the system due to different values of $\hat{k}_{ts}$ for the point load input. The values of $\hat{k}_{ts}$ for the different resonance peaks from left to right are 6.1, 7.0, 7.8, 8.7, 9.5, 10.4, and 11.2. For the slope output, the resonance vanishes due to a system antiresonance located at $f = 287$ kHz (marked with a line in the graph).

outputs, the resonance peak shifts for increasing contact stiffness, similar to the prediction of the FMA model. Additionally, the response for the slope output is dramatically changed. The cancellation of the system resonance is due to the antiresonance at 287 kHz.

Recently, a new method called force modulation spectroscopy has been developed to perform direct measurements of single-molecule stiffness and viscoelasticity with the AFM [68]. In this measurement the distributed force corresponds to the thermal excitation of the cantilever, and the tethered molecule generates the interaction force at the cantilever end. Figure 3.10 shows the shift of the first resonance peak for both outputs of the distributed force input with $\hat{k}_{ts}$ ranging from 0 to 2.4. The damping was $c = 0.04$, corresponding to the liquid environment of the experiment. The position output suffers a higher magnitude decrease than the slope output due to the reduction of the cantilever vibration amplitude caused by higher stiffness. This suggests that the position output can offer a higher sensitivity for the measurement of resonance shift in force modulation spectroscopy.

3.3.3   Poles of the coupled system

The poles of the system correspond to the complex roots of the denominator D in (3.41). The denominator is common to all the studied cases, due to the fact that the system poles are not affected by the selection of inputs and outputs, as
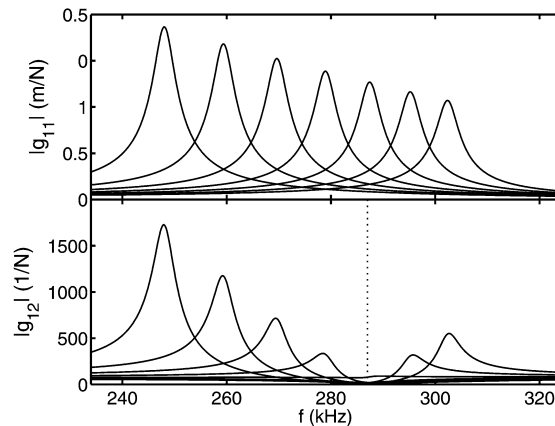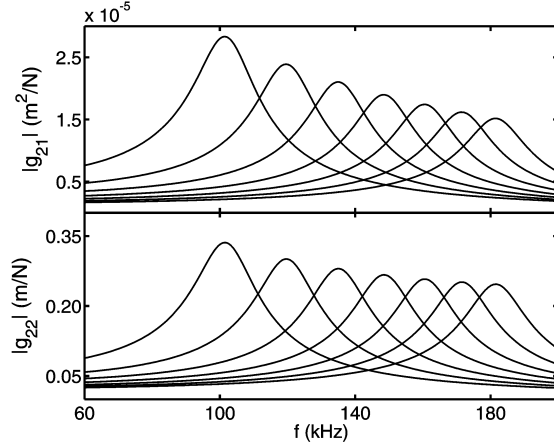
Figure 3.10: Shift of the resonance curve for both outputs of the system due to different values of $\hat{k}_{ts}$ for the distributed force input. The values of $\hat{k}_{ts}$ for the different resonance peaks from left to right span from 0 (free oscillations) to 2.4, with increments of 0.4.

mentioned above. As in the free cantilever study to obtain an exact expression of system poles the denominator has to be written in form of an infinite product expansion. Depending on $\hat{k}_{ts}$ three cases must be distinguished,

1. If $\hat{k}_{ts} > -1$, then

$$D(s) = C \prod_{n=1}^{\infty} \left[1 + \frac{4L^4\lambda^4}{d_n^4} \right]. \tag{3.46}$$

2. If $\hat{k}_{ts} = -1$, then a root at zero must be added to (3.46),

$$D(s) = \frac{88}{35} L^4 \lambda^4 \prod_{n=1}^{\infty} \left[1 + \frac{4L^4\lambda^4}{d_n^4} \right]. \tag{3.47}$$

3. If $\hat{k}_{ts} < -1$, the expression for the denominator is

$$D(s) = C \left[1 - 16 \frac{4L^4\lambda^4}{d_0^4} \right] \prod_{n=1}^{\infty} \left[1 + \frac{L^4\lambda^4}{d_n^4} \right]. \tag{3.48}$$

In (3.46), (3.47) and (3.48), $C = 8(1 + \hat{k}_{ts})$, d_n is the infinite sequence of increasingly ordered real positive solutions of the transcendental equation

$$\frac{3\hat{k}_{ts}}{d_n^3} \left[\sinh d_n \cos d_n - \cosh d_n \sin d_n \right] = 1 + \cos d_n \cosh d_n, \tag{3.49}$$

and d_0 is the only real, positive solution of the following equation:

$$2 + \cos d_0 + \cosh d_0 = -\frac{12\hat{k}_{ts}}{d_0^3} \left[\sinh d_0 - \sin d_0\right]. \tag{3.50}$$

Note that C, d_n and d_0 are all parameterized by $\hat{k}_{ts}$. Substituting the value of $\lambda(s)$ from (3.17) in expressions (3.46) and (3.48), it is possible to find the location of the poles for all three cases. For all values of $\hat{k}_{ts}$, there are poles verifying

$$\frac{cs_{\text{poles}} + ms_{\text{poles}}^2}{EI} = -\frac{d_n^4}{L^4}, \tag{3.51}$$

and solving for s_{poles},

$$s_{\text{poles}} = -\frac{c}{2m} \pm \sqrt{\frac{c^2}{4m^2} - \frac{EId_n^4}{mL^4}}, \tag{3.52}$$

which, for c smaller than d_n, yields a pair of complex conjugated roots.

For case 2 ($\hat{k}_{ts} = -1$), in addition to the poles given by (3.52), there is one additional pole at the origin and another pole located at $-c/m$.

In case 3 ($\hat{k}_{ts} < -1$), in addition to the poles in (3.52), there are two real poles, one with a negative real part and another with a positive real part (unstable pole),

$$s_{\text{poles}} = -\frac{c}{2m} \pm \sqrt{\frac{c^2}{4m^2} + \frac{EId_0^4}{4mL^4}}. \tag{3.53}$$

To find the numerical values of the resonant frequencies, the approximation introduced in § 3.2.3 can be used. This approximation is not valid in case 1 for the first pair of poles, calculated with d_1 from (3.49), if $\hat{k}_{ts}$ is close to -1. In this situation d_1 approaches zero and will be of the order of c. Table 3.2 shows the resonant frequencies values for the first five resonance modes of vibration calculated using different contact stiffness.

In Fig. 3.11 the poles for the numerical values given at the end of § 3.1.4 are represented in a root locus kind of plot showing how the position of the poles is altered by changing $\hat{k}_{ts}$. The poles for the limit cases (free and pinned end cantilever) alternate on a line parallel to the imaginary axis, located on the LHP. When $\hat{k}_{ts}$ increases from zero to infinity, the poles of the case $\hat{k}_{ts} = 0$ (circles in the diagram) increase their imaginary part, reaching the limit of the values of the case $\hat{k}_{ts} \to \infty$ (crosses in the diagram).

Analogously, for decreasing $\hat{k}_{ts}$ from zero to $-\infty$, the imaginary part of the poles decreases as well. Poles of the case $\hat{k}_{ts} = 0$ move toward poles of the pinned end limit case, always staying in the LHP. The only exception is the first pair of poles of the case $\hat{k}_{ts} = 0$, the imaginary parts of which decrease until they become real (for

$\hat{k}_{ts}$	Mode 1 f_1^{res} (kHz)	Mode 2 f_2^{res} (kHz)	Mode 3 f_3^{res} (kHz)	Mode 4 f_4^{res} (kHz)	Mode 5 f_5^{res} (kHz)
-0.5	72.8	636.8	1792.7	3515.0	5811.3
0.0	102.2	640.7	1794.1	3515.7	5811.7
1.0	142.5	648.8	1796.9	3517.1	5812.6
10.0	291.8	727.3	1823.5	3530.4	5820.5
100.0	426.5	1192.6	2144.4	3684.2	5906.7
∞	448.3	1452.9	3031.4	5183.9	7910.4

Table 3.2: Resonant frequencies of the first five modes of resonance for different values of the effective contact stiffness $\hat{k}_{ts}$.

$\hat{k}_{ts}$ approaching -1). At $\hat{k}_{ts} = $ -1 one of them is located in the origin. Decreasing $\hat{k}_{ts}$ beyond -1 moves the pole further into the RHP, making the system unstable. This unstable behavior for the range $\hat{k}_{ts} \in (-\infty, -1)$ (strongly attractive regime of the surface coupling force) corresponds to the physical phenomena known as "snap-in" [69]. When approaching the surface closely the cantilever will suddenly bend toward the surface due to the attractive van der Waals forces. This instability is stopped in the real non-linear system by a change of regime to the repulsive zone of the coupling force.

3.3.4   Zeros of the coupled system

The zeros of the system correspond to the roots of the numerators of the transfer functions in (3.42) and (3.45). As the numerators of G_{11}, G_{12}, and G_{21} do not depend on the contact stiffness, the value of $\hat{k}_{ts}$ does not change the location of zeros for these cases and corresponds to the freely vibrating limit case presented above. The only case in which zeros are affected by changes in the contact stiffness is the correspondent to the numerator of G_{22}. In Fig. 3.8 it is clearly seen that the antiresonant frequencies of cases 11, 12, and 21 are not affected by the surface interaction. Figure 3.12 shows how the antiresonant frequencies are shifted by varying values of the effective contact stiffness, which is directly related to the migration of zeros shown below. Sensitivity of zeros to changes of system parameters is a characteristic of non-minimum phase behavior [56].

Two cases must be considered in order to obtain an analytical expression for the zeros of G_{22} :
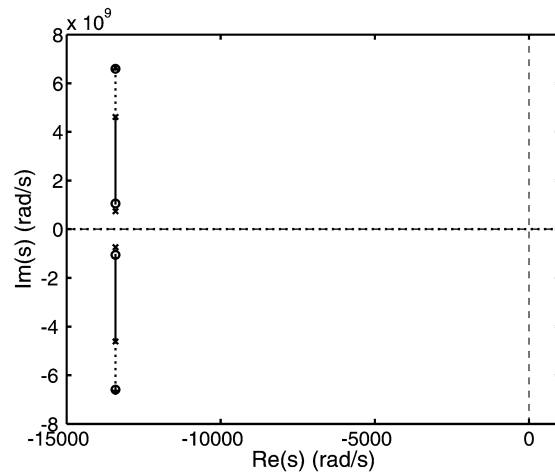
Figure 3.11: Location of poles with $\hat{k}_{ts}$. Circles mark poles at $\hat{k}_{ts} = 0$, crosses at $\hat{k}_{ts} \to \infty$. Solid lines and dotted lines describe, respectively, the movement of poles for positive and negative $\hat{k}_{ts}$. The dashed line is the imaginary axis.
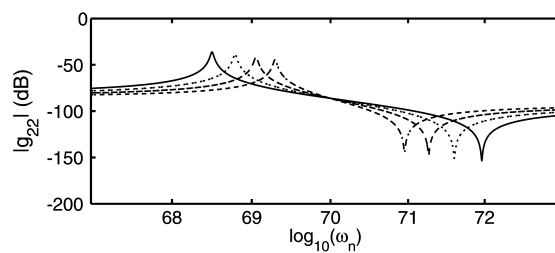
Figure 3.12: Frequency response for the case 22 showing the displacement of system antiresonances (related to zero migration) with varying constant stiffness: $\hat{k}_{ts} = 800$ (solid line), $\hat{k}_{ts} = 840$ (dotted line), $\hat{k}_{ts} = 880$ (dashed line), and $\hat{k}_{ts} = 880$ (dash-dotted line).

1. If $\hat{k}_{ts} \neq -8$, G_{22} can be expanded as

$$G_{22}(s) \quad = \quad \frac{-L^3}{6EID(s)}(8 - \hat{k}_{ts}) \prod_{n=1}^{\infty} \left[1 - \frac{L^4 \lambda^4}{z_n^4} \right]. \tag{3.54}$$

2. If $\hat{k}_{ts} = -8$, then a root at zero must be added, so

$$G_{22}(s) \quad = \quad \frac{-L^7 \lambda^4}{105EID(s)} \prod_{n=1}^{\infty} \left[1 - \frac{L^4 \lambda^4}{z_n^4} \right]. \tag{3.55}$$

In expressions (3.54) and (3.55), z_n is the infinite sequence of non-zero complex solutions, located in the first quadrant of the imaginary plane (positive real and imaginary part) and ordered by increasing absolute value, of the complex equation:

$$4z_n^3 \left[\cosh(z_n) \sin(z_n) - \sinh(z_n) \cos(z_n) \right] = 3\hat{k}_{ts} \left[\sin(z_n) - \sinh(z_n) \right]^2. \tag{3.56}$$

Substituting (3.17) in (3.54) and (3.55), we find that the zeros are located at

$$s_{\text{zeros}} = -\frac{c}{2m} \pm \sqrt{\frac{c^2}{4m^2} + \frac{4EIz_n^4}{mL^4}}, \tag{3.57}$$

and one can obtain, for small c and when the values of z_n from (3.56) are real or close to the real axis (this situation is found for large $\hat{k}_{ts}$, positive or negative), an approximate expression for the zeros whose absolute value corresponds to the location of antiresonances:

$$s_{\text{zeros}} \approx \pm i \frac{2|z_n|^2}{L^2} \sqrt{\frac{EI}{m}}. \tag{3.58}$$

In the special case $\hat{k}_{ts} = $ -8, in addition to the zeros in (3.57), there is one additional pair of real zeros, one at the origin and the other at $s = -c/m$.

In figure 3.13 the location of the zeros of case 22 when $\hat{k}_{ts}$ changes is represented. The diagram shows the rather complex zero dynamics for different values of $\hat{k}_{ts}$.

The most interesting qualitative feature of Figure 3.13 is how case 22 changes from a situation in which there are pairs of zeros in the real axis (alternating positive and negative) at $\hat{k}_{ts} = 0$ (circles in the diagram), to a situation in which there are pairs of complex conjugate zeros located in the LHP, for $\hat{k}_{ts} \rightarrow \pm\infty$ (crosses in the diagram). Numerically studying this behavior for intermediate values of $\hat{k}_{ts}$, we found that for any finite value of $\hat{k}_{ts}$ there exist RHP zeros, i.e. the case 22 (base excitation to slope measurement) is non-minimum phase. Otherwise *all* zeros are in the LHP, i.e. the system configuration is minimum phase. RHP zeros impose limitations in system performance and make the implementation of model-based control [56] difficult as noted above.
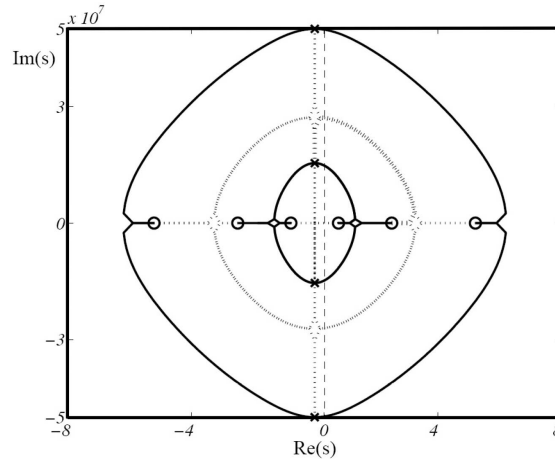
Figure 3.13: Location of zeros with $\hat{k}_{\text{ts}}$. Circles mark zeros at $\hat{k}_{\text{ts}} = 0$, crosses at $\hat{k}_{\text{ts}} \to \infty$. Solid lines and dotted lines describe, respectively, the movement of zeros for positive and negative $\hat{k}_{\text{ts}}$. The dashed line is the imaginary axis (image elaborated in collaboration with Rafael Vázquez).

3.4 Step response of the coupled cantilever

The step response of the case ij in the time domain $y_{ij}(t)$ is obtained applying the inverse Laplace transform to the product of the subsystem transfer function (G_{ij}) with the one corresponding to the unit step $(1/s)$ [66]:

$$y_{ij}(t) = \frac{1}{2\pi i} \int_{c-i\infty}^{c+i\infty} e^{st} \frac{G_{ij}(s)}{s}. \tag{3.59}$$

An exact solution to this integral is found by direct application of the residue theorem [70],

$$y_{ij}(t) = \sum_{k=0}^{\infty} \text{Res} \left[e^{st} \frac{G_{ij}(s)}{s} \right]_{s=s_k}, \tag{3.60}$$

where s_k are the singular points, i.e. the poles, of the function where the residues are evaluated.

Since (3.52) is an exact expression for all the poles of the transfer, the problem is reduced to calculate the residues. As the contribution of high order poles diminishes rapidly, i.e. the series (3.60) converges very quickly, only the first n poles contributing to the system response will be considered in the sum. Its truncation is an accurate estimate of the sum. All the cases considered above have no poles at zero. Thus the integrand in (3.59) where the residues are evaluated has a single pole at $s = 0$ corresponding to the step response transfer function.

The infinite product expansion of the denominator obtained in § 3.3.3 gives the remaining poles. Therefore, the step response is given by

$$y_{ij}(t) = G_{ij}(0) + \sum_{k=1}^{\infty} \frac{e^{s_k t}}{s_k} Res\left[G_{ij}(s)\right]_{s=s_k}. \tag{3.61}$$

$G_{ij}(0)$ is evaluated using the expressions for numerators and common denominator given in § 3.3.3 and § 3.3.4. The residues of the transfer function can be evaluated by application of the L´Hôpital rule [71]

$$Res\left[G_{ij}(s)\right]_{s=s_k} = N_{ij}(s_k) \lim_{s \to s_k} \frac{s - s_k}{D(s)} = \frac{N_{ij}(s_k)}{D'(s_k)}, \tag{3.62}$$

where $N_{ij}(s_k)$ and $D(s_k)$ are respectively the numerator and common denominator of the transfer function evaluated at s_k, and $D'(s_k)$ denotes the derivative of the common denominator with respect to s. Introducing (3.62) in (3.61) and applying the chain rule, the step response to a unit force is given as

$$y_{ij}(t) = G_{ij}(0) + \sum_{n}^{k=1} \frac{e^{s_k t}}{s_k} \frac{N_{ij}(\lambda(s_k))}{D'(\lambda(s_k))\lambda'(s_k)}. \tag{3.63}$$

If cantilever base motion is being considered then (3.22) must be used to calculate the step response.

Figure 3.14 shows the response to a unit force step of the different system configurations considered above with varying contact stiffness $\hat{k}_{ts}$. The damping factor of $c = 0.3$ kg/ms (corresponding to a liquid environment) was used to better exemplify the dynamics of the system. The steady response amplitude decreases with increasing contact stiffness and increases cantilever oscillations before the steady state is reached.

The non-minimum phase behavior in a certain range of $\hat{k}_{ts}$ for the system configuration corresponding to G_{22} is observed in the transient response of the cantilever. Figure 3.15 shows the normalized force step response of G_{22} with varying contact stiffness $\hat{k}_{ts}$. The system reacts against the input at the very beginning, corresponding to its non-minimum phase character. The amplitude of the reaction at the beginning increases with increasing $\hat{k}_{ts}$.

This example illustrates that the properties of the system transfer function give a direct insight into cantilever transient response. Other models using simplified AFM dynamics or considering a finite number of modes will not accurately describe the dynamics of the system unless they include the zero dynamics which plays an important role as seen in (3.63). It is also worth noting that the impulse response of the system can be easily found using the previous derivation. The transfer function of the impulse is the unit function without any pole at $s = 0$.
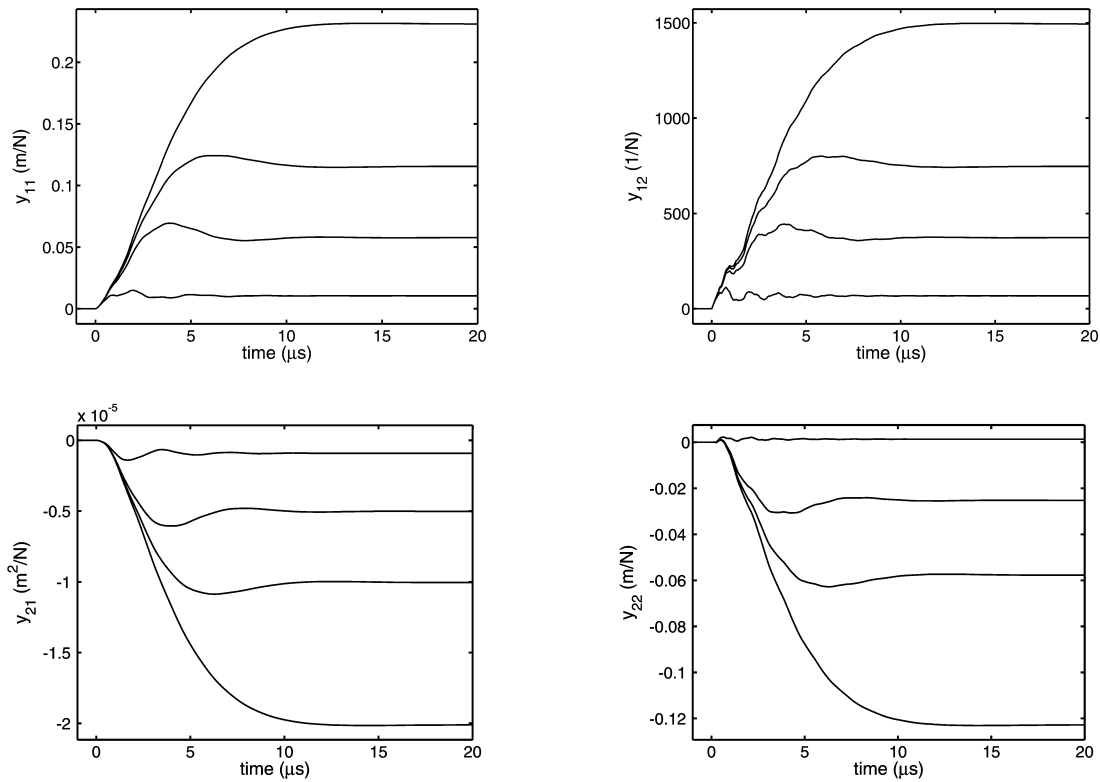
Figure 3.14: Response to a unit force step input of the different system configurations considered with varying contact stiffness ($\hat{k}_{\text{ts}} = -1$, 0, 1, and 10). The damping factor considered was of $c = 0.3$ kg/ms. The steady response amplitude decreases with increasing contact stiffness.
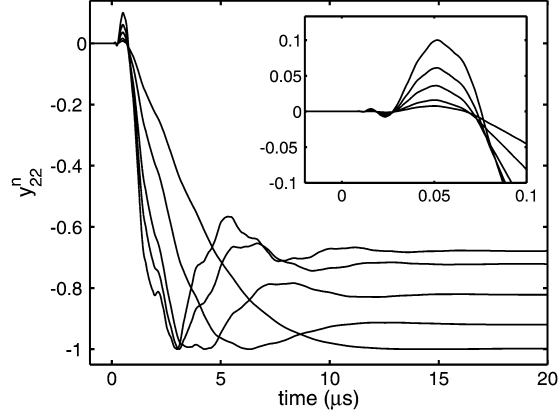
Figure 3.15: Response to a unit force step input of the normalized step response y_{22}^n with varying contact stiffness (corresponding to a distributed force input and slope output). The contact stiffnesses used are $\hat{k}_{ts} = -0.5$, 0, 1, 2 and 3. The normalized steady state response grows with increasing contact stiffness $\hat{k}_{ts}$. The damping factor considered was of $c = 0.3$ kg/ms. The inset shows a zoom of the response at the very beginning where the non-minimum character of the system produces an initial response of the system against the given force input.

Thus, it is only necessary to eliminate the term corresponding to the pole at $s = 0$ in (3.63). One direct application of the transient response of the considered system is the analysis of force spectroscopy curves obtained by AFM [27].

3.5   Conclusions

In this chapter a detailed study of the dynamic modes of operation of AFM has been presented using a system-theoretic exact approach. The infinite dimensional transfer function of the AFM cantilever for different system configurations has been obtained. From the transfer function the dynamics of the system was analyzed using the Bode plot, poles and zeros locus plot, and transient response to a force step input. The influence of system configuration and contact stiffness on the frequency response of the system has been studied using the Bode plot representation, verifying that resonances and antiresonances are greatly affected by varying contact stiffness. Poles are common to all system configurations and are obtained using the infinite product expansions of the system. Pole analysis allows the detection of a system unstable behavior for the range $\hat{k}_{ts} \in (-\infty, -1)$. The infinite product expansion of the transfer function numerator for the different system configurations enables the system zeros to be obtained. Only for the case where the cantilever is actuated by a distributed force and the cantilever slope is

considered as output are the zeros affected by the contact stiffness. Additionally, only for this case the system is non-minimum in phase for the finite values of $\hat{k}_{\text{ts}}$. The non-minimum phase behavior is manifested in the phase shift of the Bode plot and in the initial transient response to a step force input. The non-minimum phase behaviour represents a drawback for imaging and manipulation with closed-loop control since it limits feedback bandwith, and, consequently, the operational speed both for scanning and manipulating.

The transfer function approach reproduces very significant effects that simpler models cannot capture. Bode plots are a useful tool for the analysis of the dynamic operation of the AFM. The infinite product expansions enable an exact expression for all the poles and zeros of the system to be obtained. The MIMO transfer function analysis allows the quantitative study of the influence of different AFM configurations and surface interaction on system dynamics. Moreover, the transfer function analysis opens the possibility of model-based control and observer design for AFM cantilevers, improving state-of-the-art performance in microscopy and nanomanipulation.

In this thesis, the application of dynamic AFM to perform surface modifications will be illustrated. Both system configurations illustrated in this theoretical study will be used: the system configuration presented in Chapter 5 corresponds to the distributed force input while an alternative configuration is presented in Chapter 8, where an acoustic wave coupled through the tip of the cantilever corresponds to a point load system configuration. In these applications, we will observe that the dynamics behavior predicted by the transfer function, mainly the frequency shift of the cantilever response due to varying tip-surface coupling, greatly affects the forces exerted during the manipulation process. In the next chapter we present an experimental study of the phase shift along the cantilever as a validation of the transfer function description in its application on a real AFM cantilever.

Chapter 4

Resonant phase shift along an AFM cantilever

4.1   Introduction

The transfer function developed in Chapter 3 offers a detailed theoretical description of the dynamics of the AFM cantilever. While the amplitude response of the cantilever to different frequencies has been experimentally thoroughly investigated [62] [72], the phase shift has been examined in considerably less detail. Reinstaedtler *et al.* [73] measured the phase shift along the cantilever in the third flexural mode, for a system configuration where an acoustic wave was coupled to the tip[1] and the position was measured using interferometric methods. Dareing *et al* [53] presented a detailed study for the system configuration with distributed force input and slope output using a modal analysis as theoretical basis. However, they only experimentally obtained the system response for the first resonance mode. The investigation of the phase shift not only provides a validation of the transfer function description, but it is also of great relevance for material characterization by AFM and has important consequences on model-based controlling of AFM.

In this chapter the state-of-the-art experimental characterization of the AFM cantilever dynamics is further developed by measuring the phase shift along the cantilever for the first three modes of resonance. The experimental results are compared to the theoretical predictions of Chapter 3. The system configuration consists of a distributed force input and a position output. The distributed force corresponds to the inertial force generated by a piezoceramic plate supporting the cantilever. A scanning confocal optical microscope combined with a slip-stick sample positioning stage was used to measure the time varying position along the AFM

---

[1]This corresponds to the point load input in the description given in the previous chapter.

cantilever. The frequency response of the cantilever is obtained by demodulating the signal from the confocal measurement using a lock-in amplifier. This experimental setup represents a new approach to characterize the dynamics of AFM cantilevers.

4.2   Phase shift along an AFM cantilever

The transfer function $G_{21}(x, s)$ of the distributed force input to the position output along the free cantilever is given by (3.29). From the transfer function it is straightforward to obtain the phase shift $\phi_{21}(x, j\omega)$ at a given angular frequency ω:

$$\phi_{21}(x, j\omega) = \arg(G_{21}(x, j\omega)) = \arctan\left(\frac{Im(G_{21}(x, j\omega))}{Re(G_{21}(x, j\omega))}\right). \tag{4.1}$$

The Q value, commonly measured to characterize the AFM cantilever transient response at its resonant frequency [74], has a great influence on the phase shift along the cantilever. The Q value is defined as the ratio of the energy stored in the cantilever to the energy supplied per radian. Q can be obtained from the resonance curves considering that $Q = \omega_0/\Delta\omega_0 = \omega_0/\eta_{air}$. $\Delta\omega_0$ is the resonance peak width where the magnitude decreases to $1/\sqrt{2}$ of its maximum. $\Delta\omega_0$ is equivalent to η_{air} which is a material damping constant related to the environmental damping c by

$$\eta_{air} = \frac{c}{\rho w d}. \tag{4.2}$$

Figure 4.1 shows the phase shift along an AFM cantilever for the first three modes of resonance and different values of the quality factor Q calculated using (4.1). The cantilever dimensions and material parameters are given in the next section. The magnitude of Q greatly affects the phase transition at the nodes of the resonance. For the first resonance mode the time delay, which is proportional to phase shift, increases with Q (see (3.35)).

4.3   Materials and methods

A scanning confocal optical microscope working in reflectivity was used to measure the frequency response of the AFM cantilever. This confocal microscope was developed especially for imaging and dynamic characterization of microelectromechanical devices by Dr. C. Meyer in the group of Prof. J. Kotthaus (Department für Physik, Ludwig-Maximilians-Universität, Munich). A complete description of the system and its application can be found in [75]. The main optical components of the system are a laser diode operating at 635 nm wavelength and a focusing objective with a focal length of 1.8 mm, a numerical aperture of 0.8, and a working
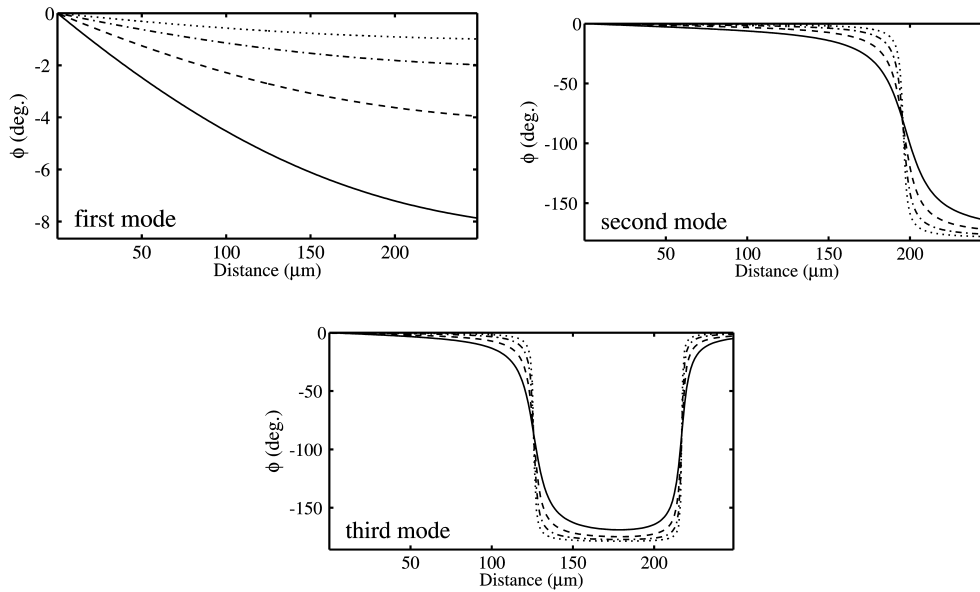
Figure 4.1: Phase shift along the cantilever for the first three resonance modes with $Q = 1, 2, 4, 8$ (respectively solid, dashed, dashed-dotted, and dotted lines).

distance of 3.4 mm (Olympus Mikroskopie GmbH, Hamburg, Munich, Germany). These two elements define a diffraction limited lateral resolution of 600 nm. The object to be measured is placed on a XYZ scanning table based on the combination of three slip-stick positioners (ANPx100, Attocube Systems, Munich, Germany). The scanning field is $7.5 \times 7.5 \times 7.5$ mm^3 with a minimum step size of 50-100 nm in ambient conditions [76]. The most important feature of the slip-stick positioner is its ability to perform almost perfectly linear scanning over the whole positioning range. In order to increase the stability of the system, a single mode optical fiber is used to guide the laser light into the optical path, which simultaneously acts as the pinhole necessary for the confocal measurement. The entire construction has been realized using titanium components. The intensity of the backscattered light is measured by a conventional silicon photodiode with a built-in amplifier (PDA 55, Thorlabs GmbH, Karlsfeld, Germany). The use of the slip-stick step motion, combined with the robustness of the microscope construction against drift and vibrations, makes it possible to perform reliable dynamic confocal measurements over large areas with high precision. The achieved vertical resolution is below 1 nm with bandwidth of 2.3 MHz for a 10 dB optical signal amplification.

To obtain the frequency response of the AFM cantilever, the signal from the confocal microscope was demodulated by a lock-in amplifier (7280 DSP, AME-TEK, Wokingham, United Kingdom). A commercial package software (Acquire, AMETEK, Wokingham, United Kingdom) was used to automate the measure-
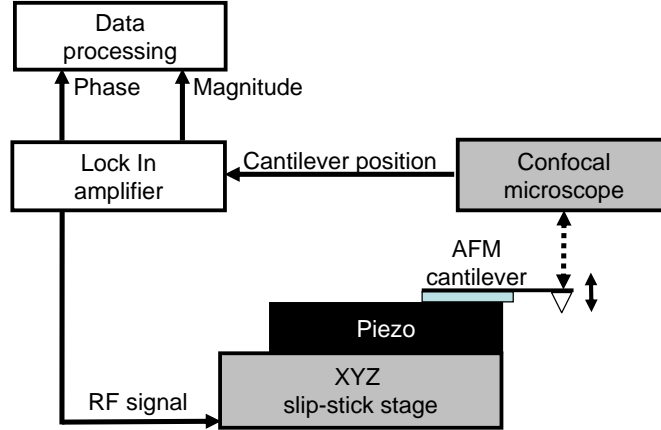
Figure 4.2: Outline of the experimental setup for the acquisition of the cantilever frequency response to an inertial force measured along its longitudinal axis. The oscillating inertial force is generated using a piezoceramic plate. The cantilever is positioned using a slip-stick scanning stage. The cantilever position is measured by a confocal microscope. The optical signal is demodulated by a lock-in amplifier to obtain the magnitude and phase shift of the cantilever oscillation.

ments. The software performs a frequency sweep of the RF signal and acquires the magnitude and phase shift from the lock-in amplified signal.

The inertial force needed to induce cantilever oscillations was generated by a piezoceramic plate ($10\times5\times0.5$ PICA51, PI Ceramic GmbH, Lederhose, Germany), which was actuated using the internal oscillator of the lock-in amplifier. The cantilever was glued on top of the piezoceramic plate using an adhesive with high bonding strength (Crystalbond 509 pk/5, SPI supplies, Weast Chester, USA). The same adhesive was used to fix the piezoceramic plate to the microscope setup.

Tipless Si cantilevers without coating were used for the frequency response measurements to eliminate effects from tip mass and multilayer friction which are not considered in our model. The nominal dimensions of the used cantilevers (NSC12, MikroMasch, Tallinn, Estonia) are: length = 250 ± 5 μm and width = 35 ± 5 μm. The cantilever thickness d and damping factor c were obtained applying (3.34) and the following equation derived from (4.2)

$$d = \frac{Qc}{2\pi f_1^{exp}\rho w}. \tag{4.3}$$

The values of the quality factor Q and the first resonant frequency f_1^{exp} were obtained from the experimental first resonance curve: $Q = 25.7$ and $f_1^{exp} = 12.85$ kHz. The following semi-empirical values were obtained: $c = 1.5\times10^{-4}$ and $d = 0.6$ μm.

To obtain the frequency response a confocal image of the cantilever is first

	f_1 **(kHz)**	f_2 **(kHz)**	f_3 **(kHz)**
Theo.	12.85	80.53	225.49
Exp.	12.85	87.20	255.40

Table 4.1: Theoretical and experimental numerical values of the first three resonant frequencies of the AFM cantilever.

acquired. This image allows a precise focusing of the confocal laser at the free end of the cantilever and a centering with respect to its longitudinal axis. Then, the cantilever frequency spectrum is acquired over the whole range of the lock-in amplifier (0–2 MHz). From this frequency spectrum, the values of the different resonants frequencies are obtained. Finally, the frequency response in the regions close (± 10 kHz) to the resonant frequencies are acquired at equally spaced points along the cantilever longitudinal axis. For each point, the focus position was carefully adjusted to obtain the maximum oscillation amplitude of the optical signal. The acquired data is saved and processed using self-programmed routines. Figure 4.2 shows an outline of the experimental setup.

4.4   Experimental results

Figure 4.3 shows a confocal micrograph of an AFM cantilever. Although the cantilever had been adjusted carefully such that its longitudinal axis is positioned in the focus plane of the microscope, the micrograph displays a strong variation in the intensity of the backscattered light. This strong intensity variation results from the high vertical sensitivity of the confocal measurement. Fabrication defects on the reflecting surface also affect the reflectivity and produce confocal imaging artifacts. The zoomed micrograph shows that cantilever shape is not perfectly rectangular. In the image it can be seen that the free end is wider than our model, i.e. the real cantilever shape differs slightly from that used for modeling. The additional mass at the free end of the real cantilever affects its dynamical response [77]. From the image, the high positioning linearity achieved by the slip-stick positioner is clearly seen.

The frequency spectrum of the cantilever is shown in Fig. 4.4. From the frequency spectrum, the experimental values of the resonant frequencies are obtained (Table 4.1). As the first resonance curve was used to get the semi-empirical values of cantilever thickness and damping, it is not surprising that the experimental and theoretical values of the first resonant frequency are the same. The second and third experimental resonant frequencies are slightly higher (approx. 10 %) than theoretically predicted, due to the additional mass at the end of the real cantilever.
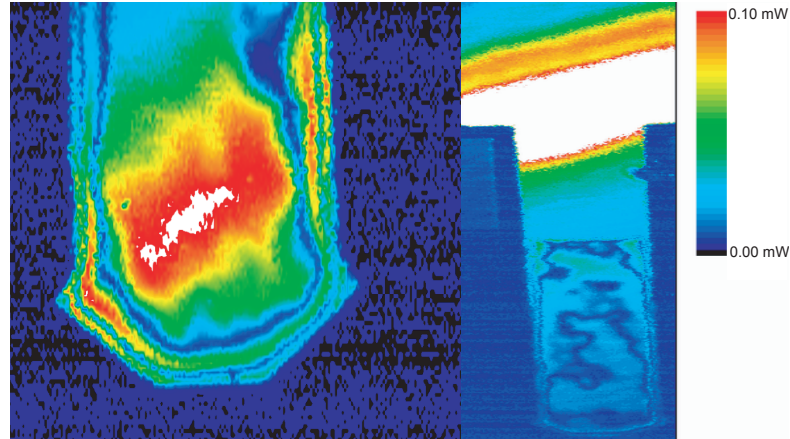
Figure 4.3: Scanning confocal optical micrographs of an AFM cantilever. The right image shows the whole cantilever (image size: $61 \times 120~\mu\mathrm{m}^2$). The left image displays a zoom on the free end of the cantilever (image size: $55 \times 55~\mu\mathrm{m}^2$). The color scale corresponds to the light intensity of the confocal measurement. The slight tilt of the cantilever with respect to the focus plane combined with material defects results in a strong image contrast on the cantilever surface.

Further, the third resonance peak presents a much higher oscillation amplitude, although a decrease of peak magnitude in higher resonance modes is expected. This amplification of higher resonance modes is due to a higher response of the piezoceramic plate in this frequency range[2]. Therefore, the acquired frequency spectrum does not only reflect cantilever properties but is also influenced by the dynamics of the excitation and measurement system.

The magnitude and phase shift at the first three resonant frequencies measured at the free end of the cantilever are shown in Fig. 4.5. Once more, the data corresponding to the first resonance matches the theory almost perfectly. The resonance curves corresponding to the second and third mode also agree well with the theoretical curve. Mismatches are mainly due to differences between the modeled cantilever and the real one as explained above. In all the modes, a 90° shift is found exactly at the resonance peak, and the predicted 180° phase shift difference in the resonance curve is also observed.

Finally, the experimental phase shift along the cantilever is presented in Fig. 4.6. As the oscillation magnitude greatly decreases close to the cantilever fixed end, the data obtained in this region does not match the theoretical curve well. The rest of the data, however, agrees with the theory. Most importantly, each figure corresponding to the n-th mode of vibration presents the expected $n-1$ nodes,

---

[2]The frequency response of the piezoceramic plate was measured and presents an increased response in the range 220-450 kHz with a resonance peak at 367.5 kHz (data is not shown).
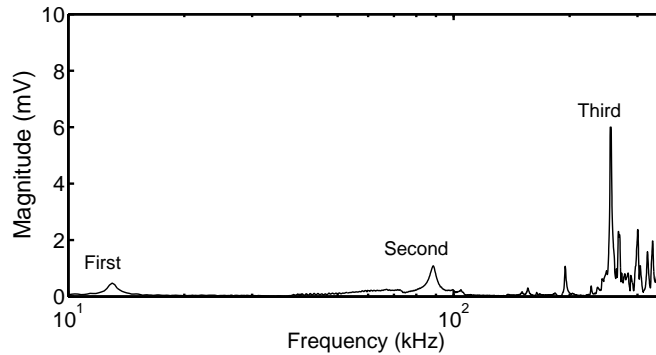
Figure 4.4: Cantilever frequency spectrum including the first three resonances (indicated in the figure). The higher magnitude of the third resonance peak is due to the frequency response of the piezoceramic plate, higher in this region of the spectrum.

at which a phase shift of 180° is observed. The slight phase shift produced by the finite velocity of the material waves (see Fig. 4.1) is obscured by the limitations of the measurement due to the smallness of the oscillations at the cantilever fixed end.

4.5   Conclusions

In this chapter a new experimental method for characterizing the dynamic response along an AFM cantilever has been presented. Precise and reliable positioning is achieved by a slip-stick stage. The position of the cantilever is measured with sub-nanometer precision by a confocal optical position measurement. The frequency response, magnitude and phase shift of the oscillation are obtained by demodulation of the optical signal by a lock-in amplifier. The phase shift at the free end of the cantilever and along the cantilever has been studied in detail for the first three resonance modes. A phase shift of 90° is measured at the resonant frequencies, with a whole resonance shift of 180° along the resonance curve. A phase shift of 180° is produced at each of the modal nodes. Deviations of the experimental data from the theoretical values can be mainly attributed to the difference in dimensions between the real cantilever and the one considered in our model. In summary, the experimental data agrees well with the theoretical model developed in Chapter 3, confirming that the transfer function is a valid approach for the characterization of AFM cantilever dynamics. The presented high frequency phase shift investigation is important for phase imaging AFM applied to obtain material contrast on surfaces with different composites [78]. Furthermore, a detailed characterization of the phase shift along the cantilever is an important issue for the development
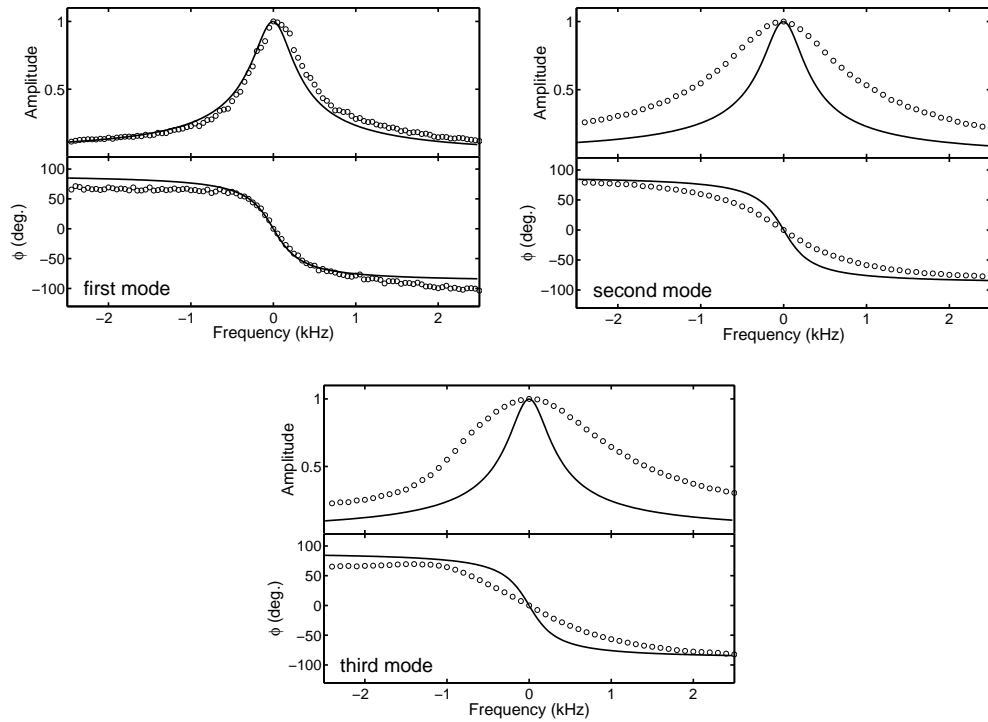
Figure 4.5: Phase shift at the free end of the cantilever. Circles correspond to the experimental values. Solid lines show the theoretical frequency response. Oscillation magnitude has been normalized at the maximum of each mode. The value of the n-mode resonant frequency f_n was used to center the data.

of model-based control of AFM cantilevers, which is critical for the controlled manipulation of surfaces at the nanometer scale.
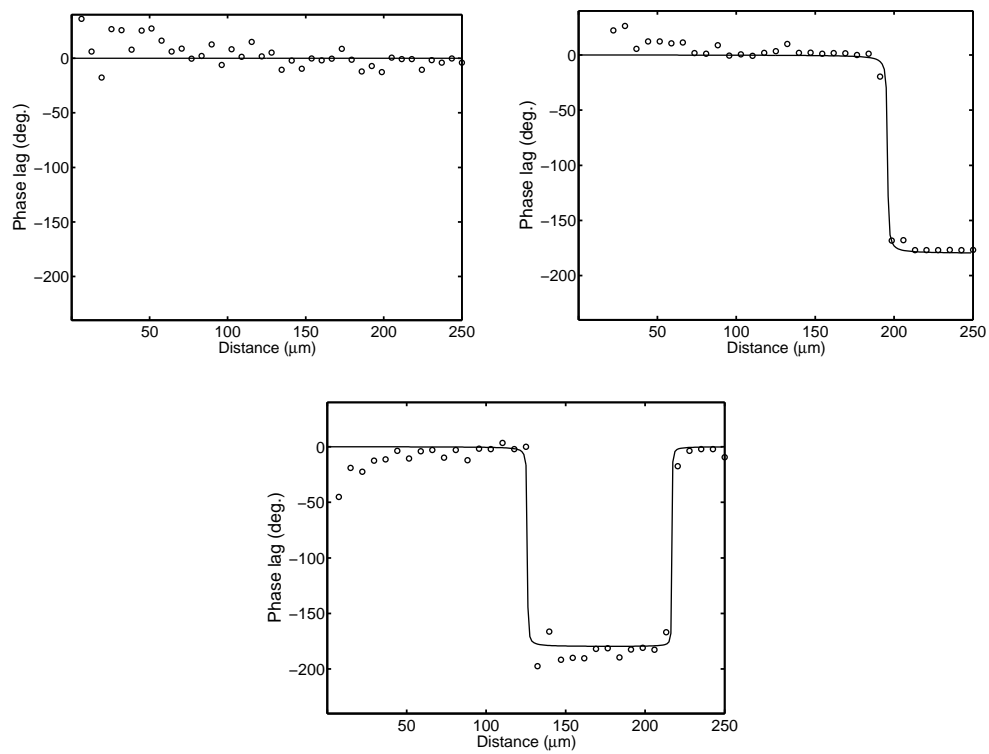
Figure 4.6: Experimental and theoretical phase lag along the cantilever. Reference phase for the experimental data was obtained by fitting the data of the 20 measurements closer to the free end.

Chapter 5

AFM based NanoManipulator for mechanical and optical lithography[1]

High resolution imaging of surfaces is the standard application of the AFM. In addition, surface modifications with a resolution far beyond the optical diffraction limit can be achieved by taking advantage of the mechanical contact of the AFM tip with the sample. Yet nanomanipulation based on AFM has some limitations, mainly due to its low speed and restricted range of operation. However, manipulation performance can be greatly enhanced by combining AFM with other methods such as optical microscopy, UV-laser ablation, automated lithography control and haptic interfacing.

The combination of AFM with optical microscopy enables a fast sample investigation to find the area of interest for surface modification. Laser ablation is a complementary tool in micro-patterning which is suitable for hard, brittle and heat-sensitive materials. For laser ablation, pulsed ultraviolet (UV) lasers are particularly useful for non-contact surface ablation because of the precision (± 2000 Å) with which the depth of the cut can be controlled as well as the lack of thermal damage to the sample [79]. For many applications, such as the patterning of flat soft surfaces [80], an automated control of the AFM cantilever with predefined manipulation parameters and path to be traced during the process is very efficient. However, on the complex surfaces of biological systems, the sample properties exhibit such strong local variation that predictable surface modification becomes difficult. In these cases, the control of the manipulation by the human

---

[1]This chapter has been partly published in: F. J. Rubio-Sierra, S. Burghardt, A. Kempe, W. M. Heckl, and R. W. Stark (2004): *Atomic force microscope based nanomanipulator for mechanical and optical lithography*, Proc. 2004 4th IEEE Conf. Nanotechnology, 17.-19. Aug Munich, Germany, pp. 468-470.

user through a haptic interface offers a very promising approach [81]. As low-cost haptic interface a force-feedback joystick offers the necessary tactile response and easy implementation in the system [82].

In this chapter a detailed description of the NanoManipulator, a fully developed system for manipulation of surfaces at the nanometer scale is presented. In the NanoManipulator system the above mentioned methods have been combined in a single instrument to extend the AFM capabilities for surface manipulation. This chapter is organized as follows: firstly, a system overview is presented and is followed by a detailed description of its main components and of the control software developed. Additionally, experimental demonstrations of system functions, both for imaging and manipulation, are given to illustrate the performance of the NanoManipulator.

5.1   System overview

Figure 5.1 shows a schematic drawing of the NanoManipulator system and its main components. An inverted optical microscope equipped with a CCD camera provides video-microscopy to the system. The modified microscope sample stage allows for XYZ sample positioning with nanometer resolution. A UV-laser is coupled through the optical path of the microscope. The AFM head is placed on top of the sample stage, with an embedded Z-stage which allows for precise vertical positioning of the AFM sensor. The combination of the sample stage and AFM head makes possible to obtain high-resolution images and to modify surfaces either by UV-laser ablation or mechanical manipulation. A digital signal processor (DSP) controls the system operation communicating with a control computer for user interaction. The control computer manages the joystick control interface which consists of a two-axis positioning joystick and a force-feedback joystick.

The hardware is controlled by real-time routines implemented in the DSP. The main program on the control computer communicates with the DSP, interacts with the user through a graphical user interface (GUI) and manages the joystick system. The tasks to be performed by the NanoManipulator are defined in the graphical interface and loaded into the DSP for their real-time execution. During the execution, the DSP transmits the data to the graphical interface to give the user online visual feedback. Figure 5.2 shows a diagram of the different software modules and their respective associated system components.

The user interface includes all the functionalities necessary to control an AFM and to display topography and other related data. These functionalities are extended for manipulation purposes. One module allows lithography experiments to be predefined by setting the trajectory of the tip, velocity, tip-sample distance and amplitude of oscillation for dynamic nanomanipulation. The automated lithogra-
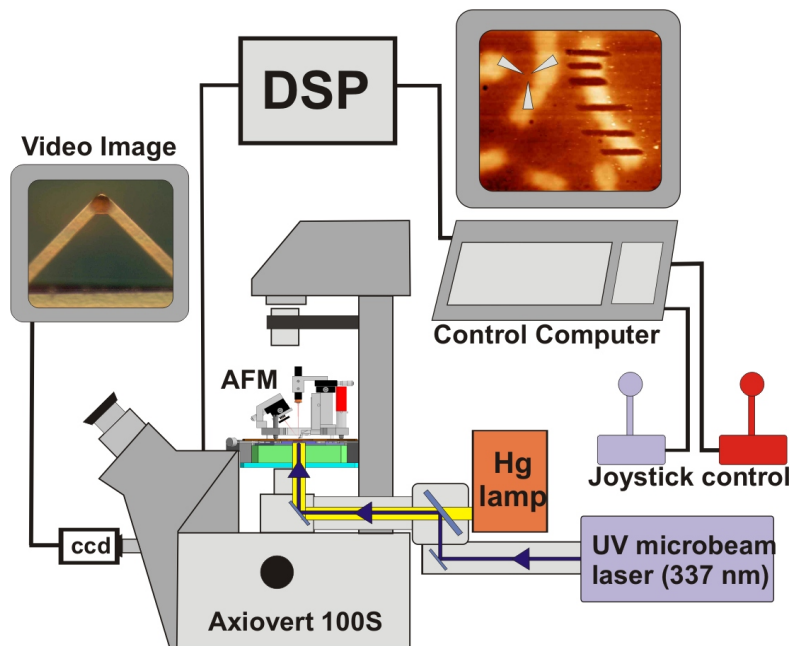
Figure 5.1: Schematic drawing of the NanoManipulator system depicting the main components of the experimental setup. The home-built AFM is placed on top of an inverted microscope equipped with a video image system and coupled to a UV microbeam laser. The system is controlled by a DSP using real-time routines. Interaction with the user is provided by a graphical interface on a control computer. A user-friendly control to accomplish fast manipulation is provided by the haptic joystick interface.

phy is performed using a vector-scan control approach [33], i.e. the pattern to be machined on the surface consists of a set of lines defined by the user in the graphical interface. The second nanomanipulation module enables the user to directly take control of the system using the joystick interface. In this mode the sample is displaced in the XY plane using the positioning joystick while a haptic signal is generated through the force-feedback joystick. Both manipulation modules can also be used to carry out photonic ablation on surfaces.

5.2 Optical components

For optical monitoring of the sample an inverted optical microscope is used (Axiovert 100S, Carl Zeiss MicroImaging GmbH, Göttingen, Germany). The microscope is equipped with a CCD camera (CoolSNAP, RS Photometrics, Tucson, USA) for digital image acquisition.
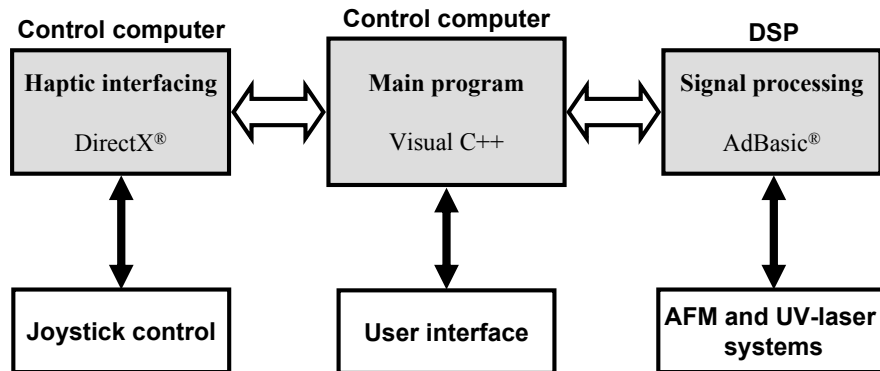
Figure 5.2: Diagram of the software used and its relationship to system components. The main program, implemented in Visual C++, communicates with the DSP, manages the joystick control through DirectX® routines and allows user interaction through the graphical user interface. Real-time routines, which are programmed in AdBasic® and implemented in the signal processor, control the experimental system.

The UV microbeam laser (P.A.L.M. Mikrolaser Technologies AG, Bernried, Germany) for laser ablation is focused on the sample through the microscope objective using the fluorescence illumination path via two high power beam splitters. The high power nitrogen laser is specified with a laser output of 337 nm (light wavelength in the UV range), pulse width of 3 ns, pulse repetition rate between 0 and 60 Hz and maximum pulse energy of 300 μJ. Laser pulses can be started either by a manual trigger board or by an external TTL trigger input.

The microscope objectives used are 10× 0.25 Ph1 Achromat, 40× 0.60 Glyc Ultrafluar oil immersion, and 100× 1.20 Glyc Ultrafluar oil immersion (Carl Zeiss MicroImaging GmbH, Göttingen, Germany). The oil immersion objectives are characterized by their high numerical aperture which reduces the size of the laser focus spot and improves ablation resolution. The theoretical minimum for the spot size is given by $1.22 \lambda / NA$, where λ is the wavelength of the laser light and NA is the numerical aperture of the objective.

5.3   AFM System

To position the sample in the planar coordinates, a piezoelectrically driven XYZ-flexure positioner is used (P-517 PZT Flexure Stage, Physik Instrumente GmbH & Co., Karlsruhe, Germany). The XYZ-flexure stage is equipped with capacitive position feedback sensors for closed-loop operation, is fixed on top of the inverted microscope, and manages the positioning of the sample-holder attached
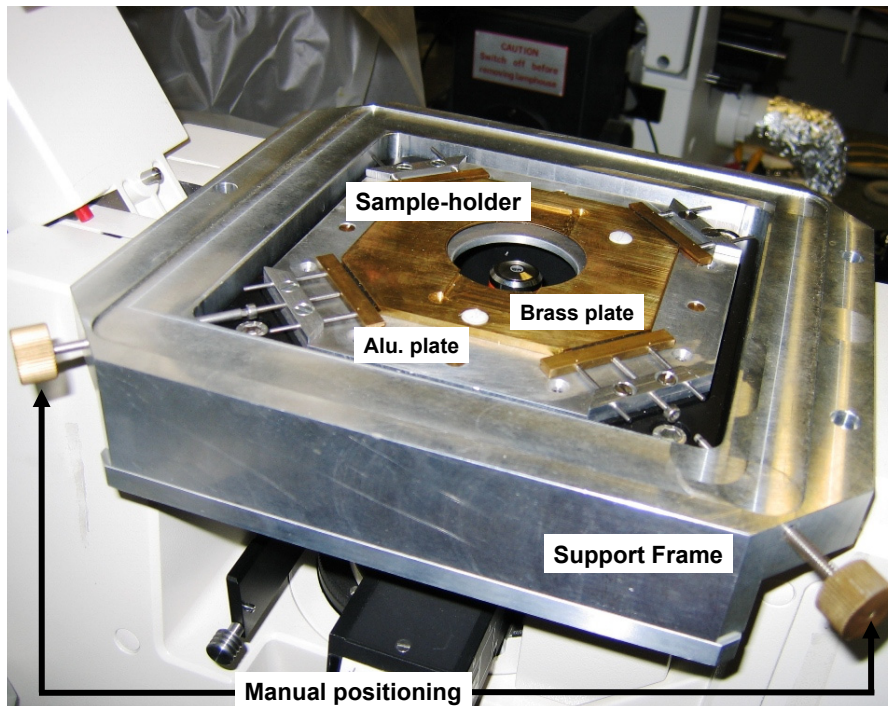
Figure 5.3: Photograph of the AFM sample stage on top of the inverted optical microscope. The sample rests on the brass plate which slides over the aluminum plate attached to the XYZ positioner. Sample position can be adjusted using precision screws.

to its mobile piece. The sample-holder can be positioned laterally by the flexure stage with 1 nm resolution in a 100 μm range achieving 5 nm position repeatability in closed-loop operation. The vertical positioner has a full range of 20 μm and is only applied for precise focusing of the UV-laser. An opening in the flexural stage allows placement of the sample over the objective of the inverted optical microscope.

The sample-holder allows a manual coarse positioning of the sample and has been designed to keep its weight as low as possible in order to reduce loading on the XYZ-flexure stage. Loading on the XYZ-flexure stage decreases its resonant frequency and worsens scanning performance [83]. Fig. 5.3 shows a photograph of the complete sample stage.

The AFM head is situated on top of a moving plate placed over the support frame. A piezoelectrically driven stage actuator (P-753 LISA NanoAutomation Stage Actuator, Physik Instrumente GmbH & Co., Karlsruhe, Germany) is fixed in the AFM head supporting the cantilever holder. This stage controls the tip-sample distance with 0.1 nm resolution in a 25 μm range also using capacitive sensors for

closed-loop operation with 2 nm position repeatability[2]. A dither piezoceramic plate (10×5×0.5 PICA51, PI Ceramic GmbH, Lederhose, Germany) in the cantilever holder enables the operation in dynamic AFM modes.

The cantilever deflection is detected using the standard bouncing beam detection method [60]. A laser diode (DL-3147-060, IMM Meßtechnologie GmbH, Unterschleißheim, Germany) is placed in a cylindrical case with a focusing lens (focal distance = 50 mm, LA1213, Thorlabs INC, Newton NJ, USA) at its opening. The cylindrical case is held by a XY manual positioning stage. For cantilever deflection readout, the position of the reflected laser beam is detected by a quadrant-photodiode (SSO-QP-50-6U1, Silicon Sensor GmbH, Berlin, Germany). The quadrant-photodiode is placed directly on the photodiode amplifier circuit which is fixed to a XY manual positioning stage. The XY manual positioners for precise adjustment of the incident laser beam on the cantilever and of the reflected beam on the center of the quadrant-photodiode consist of two orthogonally mounted linear stages with 6.5 mm travel and micrometer actuators (MicroMech, Coherent GmbH, Dieburg, Germany).

The AFM head is supported by three micrometer screws which can be vertically adjusted. The screw at the rear part of the AFM head is actuated by a DC-micromotor (mod. no. 03037, Dr. Fritz Faulhaber GmbH & Co, Schönaich, Germany) for automated tip-sample approaching. The AFM head has been designed to ensure that vertical and lateral deflection of the cantilever correspond to orthogonal trajectories of the laser spot on the quadrant-photodiode. A photograph of the AFM head is shown in Fig. 5.4.

The complete AFM stage is depicted in Fig. 5.5. The aluminum frame supporting the different components has been designed to be as compact and solid as possible in order to avoid system vibrations and drift. Special coaxial cables (STC50A-36T, Vishay Measurements Group GmbH, Heilbronn, Germany) are used for connecting the different components to avoid electric interferences and transfer of mechanical vibrations. In the designed AFM stage, the planar and vertical actuators are separated. Thus, imaging artifacts, mainly due to positioning crosstalk which occurs in AFM systems where the XYZ actuators move relative to each other, are avoided [84].

5.4   Electronic components

A combination of analog and digital electronics is used to control the whole system. Commercial electronics are used for the generation of the piezoelectric volt-

---

[2]The Z positioner is operated in open-loop mode for scanning and manipulation to take advantage of the faster response. The closed-loop operation is applied for calibration and acquisition of force curves.
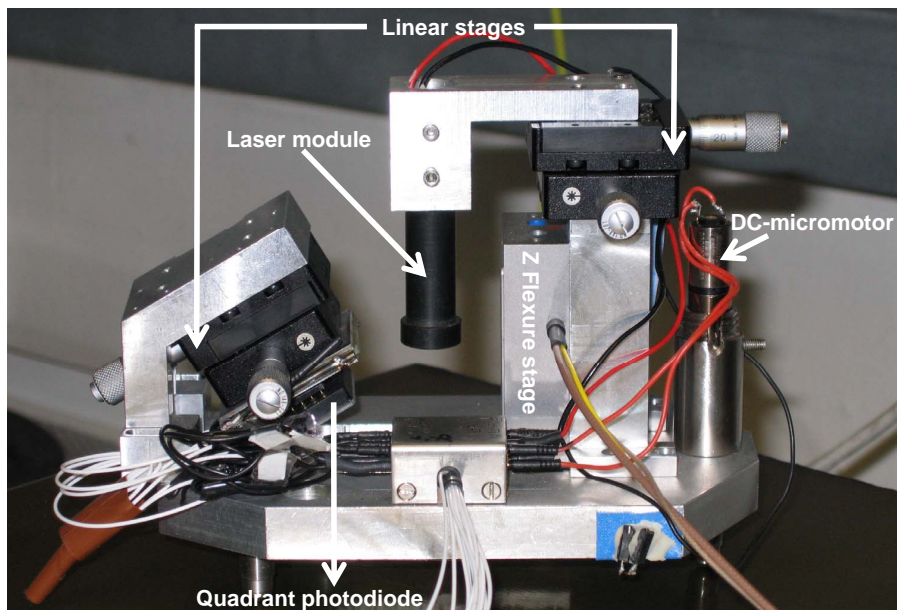
Figure 5.4: Photograph of the developed AFM head with the main elements indicated.
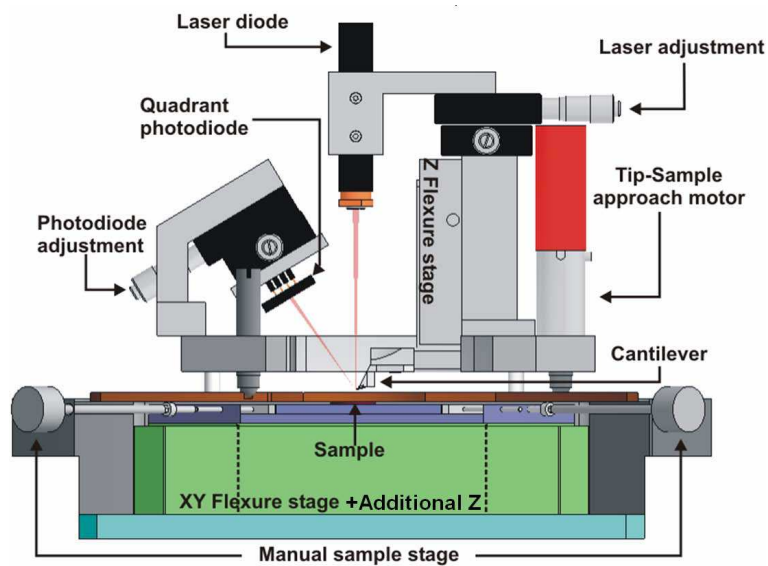
Figure 5.5: Drawing of the home-built AFM design for combined nanomanipulation. The whole setup is mounted on top of an inverted optical microscope. The sample stage is attached to the moving parts of the XYZ flexural stage. The AFM head rests on a plate which can be moved over the support frame (drawing composed with the help of Stefan Burghart).
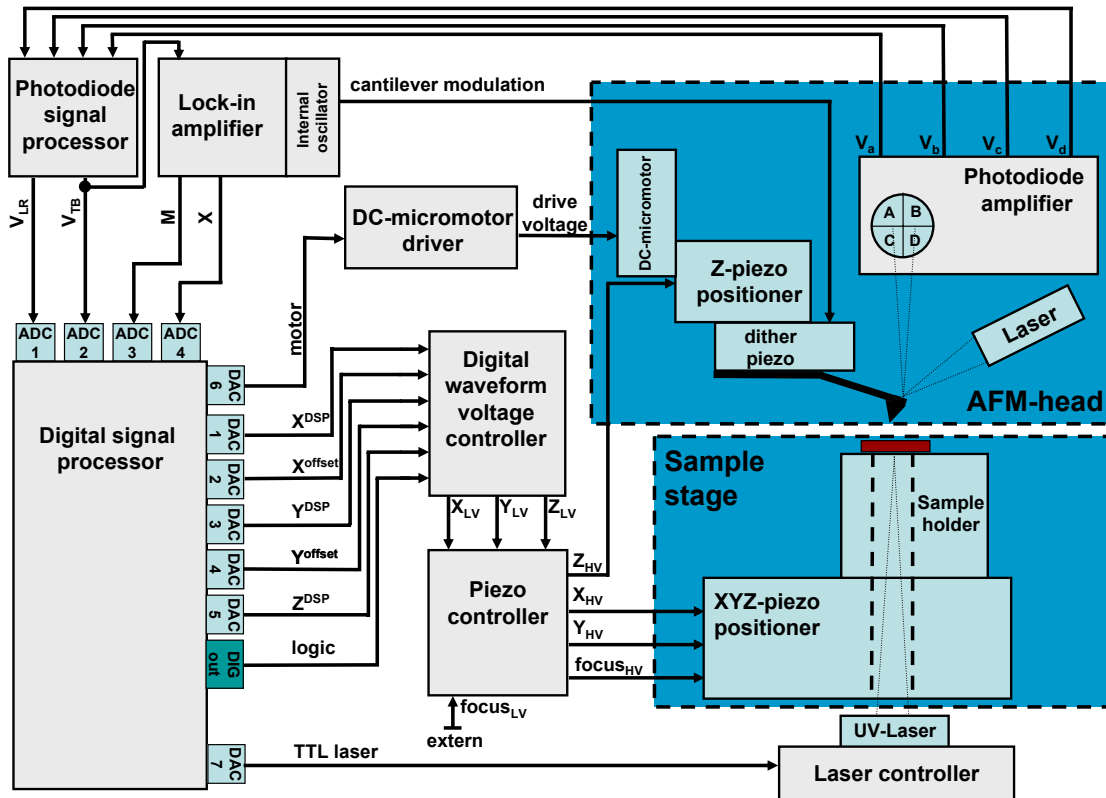
Figure 5.6: Scheme of the electronic components and main electronic signals for the control of the NanoManipulator system. "HV" and "LV" subscripts respectively denote high and low voltage signals.

ages in closed-loop operation, digital signal processing and signal demodulation for tapping mode AFM. Other components had to be specifically designed and developed including electronics for photodiode signal amplification, cantilever deflection measurement, scanning range controlling, DC-micromotor voltage generation, and laser driving. Figure 5.6 shows a scheme of the electronic control system in the NanoManipulator. In the following, a brief description of the main electronic components is given.

5.4.1   Commercial electronic equipment

The piezoelectric actuators are driven by a four channel controller (E-500 Series PZT Control Electronics Physik Instrumente, GmbH & Co, Karlsruhe, Germany). The controller also manages the closed-loop operation of the piezoelectric actuators. The controller provides connectors to drive the actuators with an external 10 V amplitude signal.

The DSP module (Adwin-Gold, Jäger Computergesteuerte Meßtechnik GmbH, Lorsch, Germany) generates the waveform for AFM operation and nanomanipulation using real-time routines. The DSP is equipped with two 100 kHz 16-bits ADCs connected through a multiplexer to 8 different channels fed into BNC inputs on the system board. For data output, the processor is provided with 8 DACs with 16-bit resolution. The ADCs and DACs of the system operate with a signal range of ±10 V. The conversion time is 3 μs for the small signal range (2 V), and 10 μs for the full data range (20 V). Additionally, the DSP module provides digital I/O through 32 digital channels TTL/CMOS compatible as input or output.

For tapping mode AFM imaging, a lock-in amplifier (7280 DSP, AMETEK, Wokingham, United Kingdom) is used to demodulate the cantilever oscillation signal in the x and y components, which are related to the signal magnitude M and phase ϕ by

$$M = \sqrt{x^2 + y^2},$$
$$\phi = \arctan(x/y). \tag{5.1}$$

When the lock-in amplifier is working in the fast response mode[3], the accessible outputs are the x-component and the magnitude M. The magnitude output can be directly used as feedback signal for tapping mode imaging. As the phase delivers information about sample material properties it should also be acquired during tapping mode imaging. In the NanoManipulator, the phase is calculated in the DSP from the lock-in outputs using

$$\phi = \arccos(x/M). \tag{5.2}$$

The lock-in internal oscillator is used to drive the dither piezo at the resonant frequency of the AFM cantilever.

5.4.2 Photodiode amplifier

Cantilever deflection is measured using the beam deflection detection scheme. Hereby, the position of the beam reflected on the cantilever is measured by a position sensitive detector, which in our system is implemented using a quadrant photodiode. In order to obtain a precise measurement of the cantilever deflection, the current corresponding to the amount of laser light on each quadrant of the photodiode has to be converted to a voltage and amplified. For that purpose, an operational amplifier working as current-to-voltage converter (transimpedance amplifier) is used for each photodiode channel, i.e. each quadrant. Due to the internal capacitance of each photodiode element this circuit tends to be unstable. To restore the stability, a capacitance is needed in the feedback path of the

---

[3]In the fast response mode, the lock-in output rate is 1 μs. This fast output rate is needed to maintain the stability of the AFM feedback-loop.

operational amplifier. To choose the values of the circuit components a `SPICE` simulation was carried out. The circuit components have been chosen to obtain the highest amplification without compromising circuit stability. From the simulation, the circuit offers a 13.5 dB amplification with a bandwidth of 750 kHz. The circuit yields four voltage outputs, each of them linearly proportional to the amount of light on each photodiode quadrant: V_a top-left quadrant output voltage, V_b top-right quadrant output voltage, V_c bottom-left quadrant output voltage, and V_d bottom-right quadrant output voltage.

The implementation of the amplifier circuit in the system is critical for system performance. Due to the great circuit amplification factor it not only amplifies the photodiode current but also any other residual signal influencing the input of the operational amplifiers. For this reason a low-noise circuit design approach was adopted: (i) the photodiode is directly attached on the circuit to avoid noise pick-up through connectors; (ii) circuits dimensions are kept small using SMD components; (iii) a shield case was built to protect the circuit from electrostatic interferences.

5.4.3   Photodiode signal processor

The outputs from the photodiode amplifier are processed by an analog circuit to measure normal and lateral deflection of the cantilever. The quadrant photodiode is adjusted in such a manner that a normal or lateral deflection of the cantilever results in a parallel trajectory of the laser spot respect to the axis dividing the quadrants.

The circuit output voltages V_{TB} and V_{LR} are proportional to normal and lateral cantilever deflection respectively. These are obtained from the outputs of the photodiode amplifier using a combination of summing and differential amplifiers performing the following algebraic operations:

$$\begin{aligned} V_{TB} &= (V_a + V_b) - (V_c + V_d), \\ V_{LR} &= (V_a + V_c) - (V_b + V_d). \end{aligned} \tag{5.3}$$

For AFM contact mode imaging the outputs are low-pass filtered at a cut-off frequency of 10 kHz and fed into the DSP for image acquisition. For tapping mode AFM, V_{TB} is connected to the lock-in amplifier without any previous filtering. The circuit bandwidth is sufficiently high, above 2 MHz, to avoid signal attenuation which could affect the signal-to-noise ratio. The acquisition of V_{LR} directly delivers the information necessary to obtain lateral force mapping of the sample surface.

Thermal noise spectra measurements were carried out to check the correct functioning of the cantilever deflection detection system (see § 5.7). These measurements revealed that the system is able to detect cantilever deflection in the range of Ångströms.
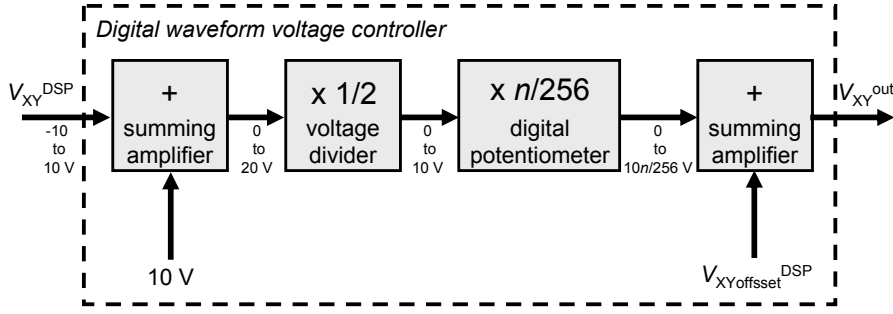
Figure 5.7: Flowchart of the digital waveform voltage controller. The voltage range of the waveform between the different stages is indicated below the respective arrows.

5.4.4 Digital waveform voltage controller

To take advantage of the positioning accuracy of the piezoelectrical flexure stages the waveform for the positioning of the DSP is processed to fulfill the following requirements: (i) the positioning waveform voltage range must accomplish the input requirements of the piezo-system controller (0-10 V); (ii) the scanning waveform must be scaled down to the selected scanning range with 16 bit resolution for all scanning ranges, i.e. one part in $1/2^{16}$ of the whole scanning range; (iii) an offset must be added to the scanning waveform to enable reduced scanning centered at any point within the positioning range.

All these requirements are implemented in the waveform controller using a combination of voltage dividers, summing amplifiers and digital potentiometers. Figure 5.7 shows the flowchart of one channel at the controller. The controller output signal for planar positioning $V_{\mathrm{XY}}^{\mathrm{out}}$ can be calculated from

$$V_{\mathrm{XY}}^{\mathrm{out}} = \frac{10 + V_{\mathrm{XY}}^{\mathrm{DSP}}}{2} \frac{n}{256} + V_{\mathrm{XYoffset}}^{\mathrm{DSP}}, \tag{5.4}$$

where $V_{\mathrm{XY}}^{\mathrm{DSP}}$ and $V_{\mathrm{XYoffset}}^{\mathrm{DSP}}$ correspond to the scanning waveform and positioning offset from the DSP respectively and n is an integer value in the range from 0 to 256. n is selected at the digital potentiometer (AD5260, Analog Devices Inc, Norwood, USA) and corresponds to the percentage of nominal end-to-end resistance. The value n is selected by a logic signal which is generated using the digital channels of the DSP. The value n to be selected is calculated in the graphical interface using the scanning range R selected by the user

$$n = \frac{\text{Calibration Factor (V/nm)} \times R}{256}. \tag{5.5}$$

The "Calibration Factor (V/nm)" corresponds to the ratio of voltage input in the piezoelectric controller and flexure displacement in nanometers which is obtained

by imaging a standard calibration sample (10 μm pitch, 200 nm deep, 3D reference, Veeco Metrology Inc., Santa Barbara, USA). The Z positioning voltage is processed similarly but neither position offset nor range scaling are necessary.

The XY positioning resolution defined by the waveform output of the controller for a selected scanning range R is $R/2^{16}$. This implies that for the maximum XY range of 100 μm the XY position resolution is limited by the electronics to 1.52 nm. The waveform resolution can be reduced by decreasing the selected scanning range until the resolution defined by the mechanical components of the piezoelectric flexure stages is the limiting factor for system positioning performance. The minimal range which can be scanned by the system is 390 nm. The Z positioning resolution defined by the waveform controller is 0.38 nm which is precise enough for the applications of this work[4].

5.4.5　DC-micromotor driver

The driving voltage for the DC-micromotor is generated by the DSP. However, the maximum output current (25 mA) which can be sourced by the DACs is not high enough to drive the DC-micromotor. Thus, to obtain a high-output current to drive the DC-micromotor a transistor circuit and an operational amplifier are combined to design a push-pull booster [85] which amplifies the DC-micromotor input current up to the required range.

5.4.6　Laser driver

The laser diode operating voltage is 5 V. To ensure the stability of the AFM measurement, laser power output must remain constant during system operation to avoid intensity drift of laser diode light. For this reason, a stable voltage source was built. Additionally, a potentiometer is implemented to manually regulate laser power output when the laser is being focused on the cantilever under the optical microscope.

5.5　DSP system control routines

The DSP is programmed using a pseudo-`BASIC` language (AdBasic® Version 4.01, Jäger GmbH, Lorsch, Germany) for simple and flexible system control. To ensure consistent timing system control the built-in timer of the DSP is used which works with a precision of 25 ns. This enables real-time operation of the system with high motion precision and a very efficient control response time. The DSP communicates with the graphical interface using a set of global parameters and data

---

[4]The Z positioning resolution can be easily reduced by decreasing the Z displacement range.

structures. The four main processes implemented in the DSP are: (i) start process for signal initialization; (ii) approach process to bring the AFM tip into contact with sample surface; (iii) feedback process, which manages all system operations, both for imaging and manipulation, following a switch-case structure; (iv) finish process for secure termination of system operation. All these processes are based on a cyclic repetition of the main routine. For all implemented processes the cycle period τ, which determines the system response time, is 10 μs.

1. **Start process**: this process is executed once at the beginning of system operation and initializes all necessary DSP signals and parameters. In this process the scanner is driven in a square trajectory over the whole scanning range as an initial system function check.

2. **Approach process**: an accurate handling of the imaging tip is of great importance to obtain high-quality AFM images. The most critical operation is when the AFM tip is brought into contact with the sample surface. For this reason an automated tip-sample approach is implemented to optimize the system response to cantilever normal deflection and hence avoid tip crash on the sample. The process is the following: first, the DC-micromotor is driven at a low speed to avoid a violent first contact on the sample; then, in each process cycle, the actual value of the feedback signal, normal cantilever deflection (V_{TB}) for contact mode or cantilever vibration amplitude (M) for tapping mode, is compared to the contact setpoint V_{SP} selected in the graphical interface. If the feedback signal reaches the selected setpoint ($V_{\text{TB}} \geq V_{\text{SP}}$ for contact mode and $M \leq V_{\text{SP}}$ for tapping mode) then the DC-micromotor is disconnected and, finally, the feedback process is started.

3. **Feedback process**: this process is the heart of the NanoManipulator system and is executed every time that the tip is in contact with the sample. The process structure is a switch-case statement. Each case statement implements a different system operation. The graphical inteface defines which case structure is executed by changing the value of a control parameter. Before the switch-case structure is evaluated, the process runs the feedback-loop and generates the voltages for the positioning piezoelectrical stages. In the feedback-loop the voltage for the vertical piezoactuator $V_z(i)$ in the i cycle is calculated by applying a proportional-integral regulator:

$$V_z(i) = V_z(i-1) + P\,E(i) + I[E(i) + E(i-1)]. \qquad (5.6)$$

Here P and I are respectively the proportional and integral constants of the regulator. Their values are set by the user in the graphical interface. $E(i)$ is the controller error given by

$$E(i) = F(i) - V_{\text{SP}}(i), \qquad (5.7)$$

where $F(i)$ is the signal used for feedback. For contact mode operation, $F(i)$ corresponds to the normal deflection of the cantilever (V_{TB}), while for tapping mode it corresponds to the magnitude of the oscillation, i.e. magnitude output of the lock-in amplifier (M). In the following a description of the subroutines of each case statement corresponding to the different system operations is given.

Joystick control: If the system is steered using the joystick control, the XY position of the sample is calculated by the graphical interface and transmitted to the DSP using ADBasic® global parameters. The stage position refreshing rate is 1 ms, defined by the time clock of the graphical interface. The positioning resolution is defined by the selected scanning range. The graphical interface calculates the position $X(i)$ in the process cycle i for the X coordinate using

$$X(i) = X(i-1) + k_x \, \Delta X \, J(i), \qquad (5.8)$$

where k_x is a calibration factor for the X axis related to the selected scanning range and volts-to-nm piezoactuator ratio, ΔX is selected by the user in the graphical interface and defines the positioning velocity, and $J(i)$ is the normalized X-axis location of the positioning joystick. The same approach is used for the Y coordinate. The Z positioning of the tip using the joystick is similarly handled with the single difference that the Z flexure stage is driven at a constant velocity (see § 5.9).

Trace line: To trace the lines necessary to perform manipulation in the vector-scan mode, the X and Y position of the sample stage are simultaneously incremented during a number N of process cycles. The X (and similarly Y) position of the stage in a given cycle is given by

$$X(n) = n\frac{\delta X}{N} + X_0, \qquad (5.9)$$

where n is sequentially incremented from 0 to N to complete a line, δX is the line length projected on the X-axis and X_0 is the X-coordinate at the initial position of the line. N is calculated by the graphical interface considering that the total number of steps is given by $N = Lv\tau$, with L being the line length, v the velocity at which the line is traced and τ the process delay. The velocity v is set by the user in the graphical interface. This algorithm takes advantage of the floating-point calculation capabilities of the DSP board and therefore the line trajectory resolution is only limited by the digital resolution of the DACs.

Scanning: In this subroutine the DSP generates the sample scan while the imaging data is acquired. The scan is generated tracing two lines (forward

and backward) in the X direction using the trace line algorithm presented above. The Y position is increased by $\Delta Y/\text{Res}$ after each forward/backward line scan. "Res" corresponds to the image resolution in the graphical interface selected by the user from the values 128, 256, 512, and 1024. While the sample is being scanned imaging data is acquired in each process cycle. Thus, for each point at the image, the acquired data is averaged k-times, with k corresponding to Res/N_{total}. N_{total} is the number of readouts in each scanning line for one direction. Once this number of steps is reached the averaged data is saved to a data point in the image and the X position is effectively advanced. The scan is rotated by an angle α by applying a mathematical two dimensional rotation in the DSP code. The values of the rotated coordinates X' and Y' are calculated from the unrotated coordinates X and Y by

$$
\begin{aligned}
X' &= X\cos\alpha + Y\sin\alpha, \\
Y' &= -X\sin\alpha + Y\cos\alpha.
\end{aligned}
\tag{5.10}
$$

The angle α is set by the user in the graphical interface.

Finish trajectory: Every time that a positioning task is finished, either for scanning or manipulation, the sample is smoothly returned to the initial position corresponding to the upper-left corner of the scanning range. This subroutine is also executed every time that any task is interrupted by the user. The subroutine main actions are to trace a line from the actual sample position to the initial scanning point and to reinitialize the necessary variables to operate the system again.

4. **Finishing**: The finish subroutine is executed every time that the main program of the graphical interface is terminated. It gradually sets all the voltages at the piezos to 0 V and retreats the tip from the sample using the DC-micromotor.

5.6   Graphical user interface

The graphical interface was programmed using Visual C++. The Microsoft Foundation Classes (also known as MFC) were used to drastically reduce the programming efforts and to facilitate further development of the graphical interface. The acquisition of joystick position and force input at the haptic interface were implemented using the DirectX® library. DirectX® is a Microsoft Co. programming interface designed to develop computer games compatible with a wide range of game devices.

The image acquisition module uses the data points for imaging acquired in the

feedback process at the DSP and displays them using bitmap structures which are updated every millisecond to optimize user visual feedback of the surface being measured. The user can select which data, including backward or forward scanning direction, is displayed. A linewise leveling algorithm is implemented to correct sample tilt online. To facilitate sample surface exploration, a user-friendly zoom selection by mouse click-and-drag was implemented. The acquired data is saved in binary files using the WSxM image processing file format (WSxM v2.1, Nanotec Electronica S.L., Tres Cantos, Spain); image data can thus be processed offline by any SPM image processing tool.

The interface for manipulation consists mainly of an image window and a manipulation parameter dialog. Figure 5.8 shows a snapshot of the graphical interface during vector-scan manipulation displaying the main components. In the image window sample topography and the real-time position of the AFM tip, represented by a cursor, are displayed. For vector-scan manipulation the user can draw the manipulation path directly on the imaging window. In the parameter dialog the values of the different parameters can be selected along with the type of manipulation (vector-scan or joystick controlled). The Z position, amplitude of tip oscillations and lateral displacement velocity are the main parameters for manipulation and can individually be set for each line of the manipulation path. Additionally, there is an option to acquire tip oscillation amplitude, Z position and average deflection during manipulation for analysis of the driven experiment. If vector-scan is being executed, the user interface sends the data of each line to the feedback process of the DSP and the lines are sequentially executed while the tip cursor on the image window gives visual feedback of the actual tip position. The manipulation module can also be used for UV-ablation. In this case the TTL signal at the DSP is turned on in the manipulation path.

5.7   Detector sensitivity and calibration

The performance of the cantilever deflection detection system is of paramount importance to obtain the high vertical resolution characteristic of AFM. As it has been mentioned previously (see § 5.4.2), the experimental characterization of the sensitivity of the cantilever deflection detection system is a complex task. A good estimation of the sensitivity of the cantilever deflection detection system is given by the acquisition of the thermal noise spectrum of the cantilever. From the equipartion theorem and considering the different modes of vibration of the cantilever [86], the mean-square deflection of fluctuations of a rectangular cantilever for the n-mode of vibration $< z_n^2 >$ is

$$< z_n^2 >= \frac{12k_\mathrm{B}T}{c_\mathrm{cant}d_n^4},$$

(5.11)
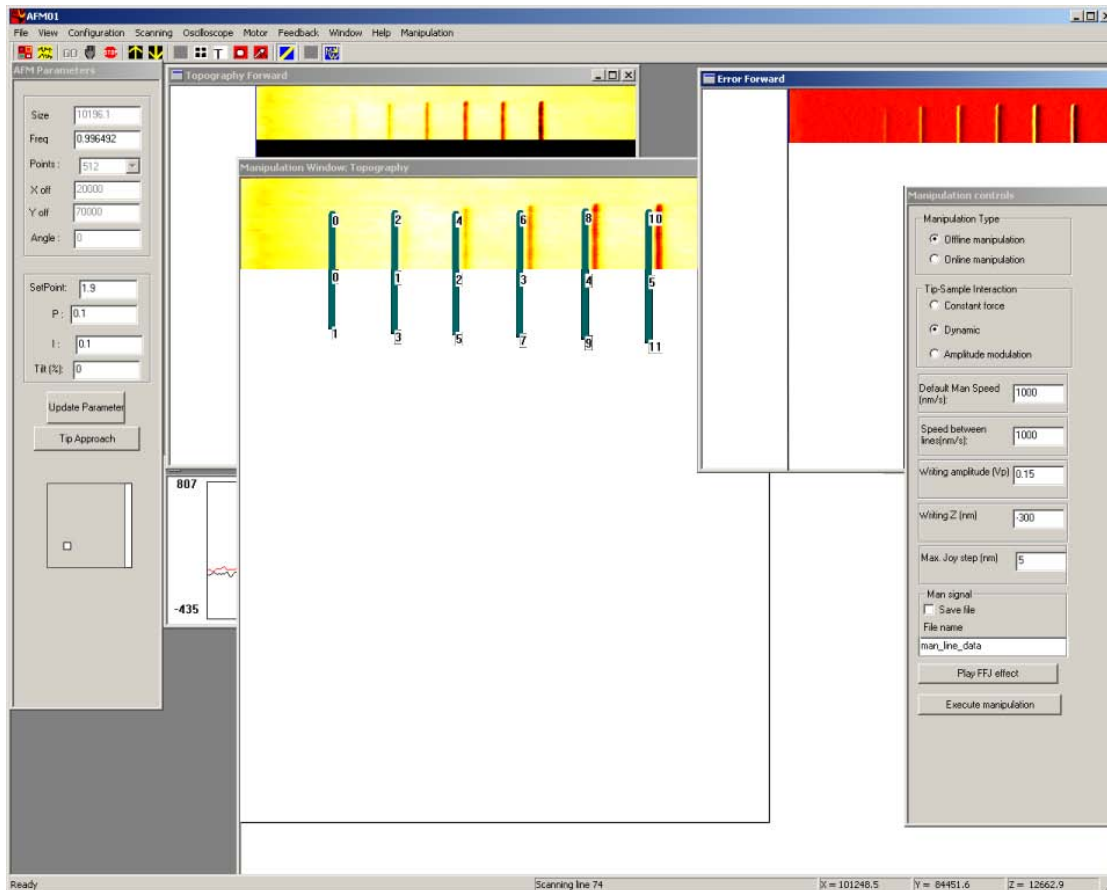
Figure 5.8: Snapshot of the graphical interface during manipulation using the vector-scan mode. During the experiment six lines with different manipulation parameters were lithographed over the surface of a thin-layer photoresist. The snapshot displays the different image windows (topography and error in the forward direction). In the manipulation window the defined traced lines are seen. The imaging and manipulation dialogs contain the options necessary for system operation.
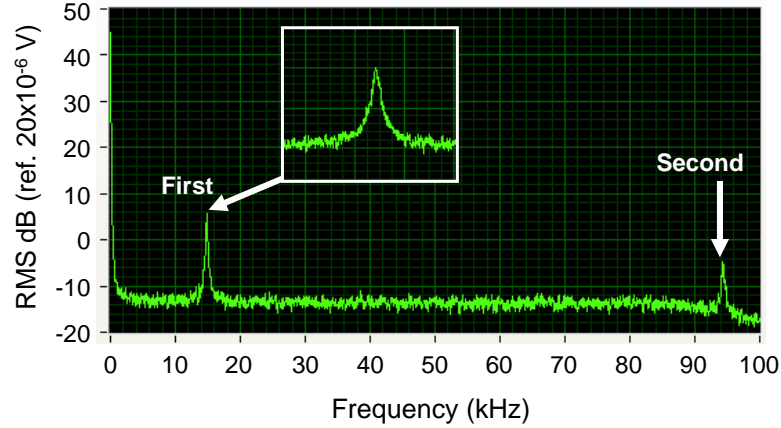
Figure 5.9: Thermal noise spectrum of an AFM cantilever measured by the Nano-Manipulator using a FFT based acquisition system. The spectrum shows the first two resonance peaks at 10.5 kHz and 90.4 kHz. The inset shows the first resonance peak acquired with higher frequency resolution.

where k_B is the Boltzmann constant, T the absolute temperature, c_{cant} is the cantilever spring constant and d_n corresponds to the real positive roots of the characteristic equation $1 + \cos d_n \cosh d_n = 0$. Figure 5.9 shows the thermal spectrum of a cantilever acquired in ambient conditions using the NanoManipulator detector (silicon cantilever, model Cont-W, Nanosensors, Neuchatel, Switzerland). In the spectrum, two resonance peaks corresponding to the first two cantilever flexural oscillation modes are clearly seen. Using the nominal cantilever spring constant of 0.28 N/m and (5.11) the estimated fluctuation amplitudes for the first two modes are 1.19 Å and 0.2 Å respectively. This shows that the developed cantilever deflection detection system is able to detect cantilever deflection in the range of Ångströms and is hence suitable for AFM operation[5].

Another important issue for the performance of the cantilever deflection detection system is the linearity of the vertical photodiode voltage V_{TB} versus vertical displacement curve during a force measurement. Additionally, the acquisition of a force measurement represents the most straightforward method for the determination of the so-called inverse optical lever sensitivity (InvOLS) [6]. Figure 5.10 shows a force curve acquired with the same cantilever used to obtain the thermal noise spectrum in contact with a silicon surface. The curve shows the high linearity of the voltage versus displacement curve over the large vertical displacement range (400 nm). The InvOLS coefficient is determined from the inverse of the fitted line slope.

---

[5]Actually, the optical lever system implemented in the NanoManipulator measures cantilever slope rather than cantilever displacement [87].
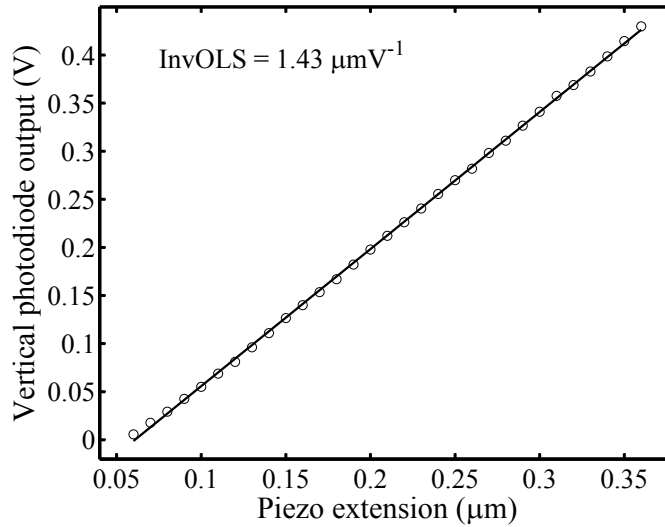
Figure 5.10: Force curve for the determination of the inverse optical lever sensitivity (InvOLS). Circles correspond to the experimental data and the solid line corresponds to the linear fit. The InvOLS from the fitted line is 1.43 $\mu m/V^{-1}$. The correlation factor of the linear fit is 0.997.

The linearity of the piezo-positioners for planar sample displacement is of high importance for metrology and manipulation by AFM. The linearity assures the correct measurement of planar distances in large scanning ranges, and allows the correct realization of predefined paths, and correct tip positioning. Figure 5.11 shows the image acquired by the NanoManipulator system of a calibration standard (10 μm pitch, 200 nm deep, 3D reference, Veeco Metrology Inc., Santa Barbara, USA) with a rectangular lattice superimposed on the AFM image aligned with the pitch. The lattice lines coincide exactly with the pitch lines illustrating the high linearity of the planar positioning system over the selected scanning range of 75×75 μm^2. This image is also used to determine the volt-to-nm calibration factors of the piezo-positioners used for AFM imaging.

5.8 Surface characterization by the NanoManipulator

The most used methods for surface characterization by AFM are contact and tapping mode imaging of surfaces and the acquisition of force-distance curves. These three methods have been implemented in the NanoManipulator system and their functionality is demonstrated by the imaging of a standard CompactDisk-Recordable (CD-R) sample and the acquisition of a force curve on a silicon surface.
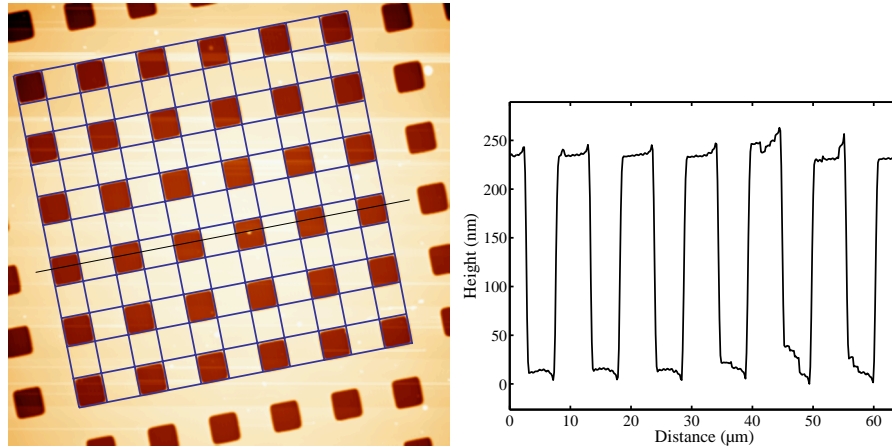
Figure 5.11: AFM image of a calibration standard and line profile along the black line on the image. From the image, the volt-to-nm calibration factors for the piezopositioner of the system are obtained. A rectangular lattice has been drawn on the image to show the high linearity over large ranges achieved by the scanning system. Image size 75×75 μm^2. Z-range 334.5 nm.

The surface of a CD-R containing information bits represents a good test sample because of its reduced feature dimensions in the range of tens of nanometers [88]. A standard CD-R consists of a 1.2 mm thick polycarbonate disk, with a spiral groove stamped on one side. The spiral groove is used to guide the laser beam for the reading and writing of the bits. Over the spiral groove side a thin film of an organic dye is spin coated. The bits are written on the thin film by ablation using the laser beam of the CD recorder. Finally, over the organic layer, a metallic film is spin coated as a reflective and protective layer. For imaging the nanosized bits this metallic film must be removed.

Figure 5.12 shows a contact mode image of the CD-R surface. The three acquired channels correspond to surface topography, error signal (not shown), and lateral cantilever deflection. The surface topography and error signal correspond to the vertical piezo-displacement and controller error respectively, which are calculated in the feedback-loop at the DSP (see (5.6)). The lateral deflection signal is obtained directly from the lateral voltage output of the quadrant photodiode V_{LR}. The contrast in the lateral deflection image results from a combination of surface topography and local material properties [7].

Figure 5.13 shows the topography and phase shift images acquired in tapping mode of a CD-R surface. The surface topography is acquired similar to contact mode imaging. The cantilever oscillation phase shift is acquired as described in § 5.4.1. Analogous to the lateral force, phase constrast during tapping mode imaging is caused by changes in tip-sample interaction caused by surface topography
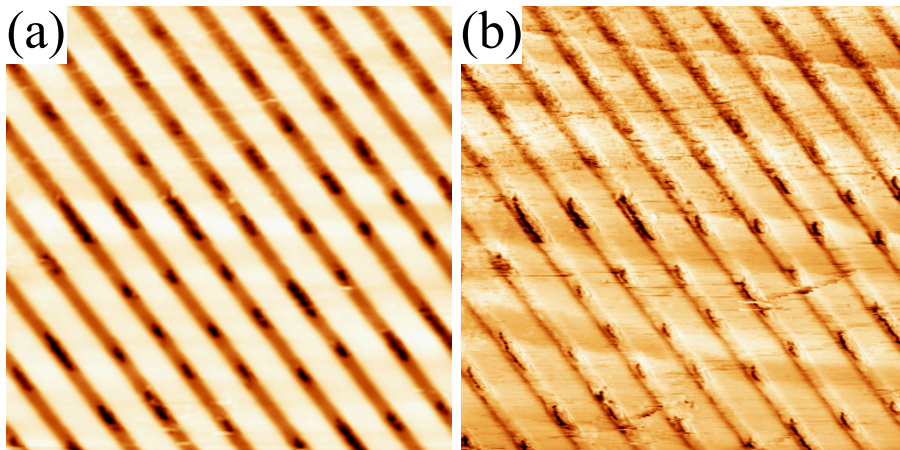
Figure 5.12: AFM image obtained in contact mode with the NanoManipulator system of the surface of a CD-R surface: (a) surface topography; (b) lateral deflection. In the images the different features of a CD-R are clearly seen such as the furrows comprising the organic material and the written bits. Image size $15{\times}15$ μm^2. Z-range: (a) 214.4 nm; (b) 20 mV.

and varying material properties [13].

Force-distance curves are a useful tool for the characterization of tip-surface interaction, giving insight into sample surface properties [27]. Figure 5.14 shows a force-distance curve on silicon in air acquired using the NanoManipulator system. The approach curve shows no changes in the cantilever deflection until the cantilever snap-into contact on the surface. In the contact region the cantilever obeys Hooke´s law, showing a linear increasement of deflection with piezo desplacement. A slight hysteresis effect is observed in the withdrawal curve at the contact region. Finally, a large negative cantilever deflection is observed beyond the contact point indicating tip adhesion at the withdrawal. This adhesion is caused by the meniscus force which appears due to the thin water layer covering the sample surface.

5.9 Joystick control stage

For XY positioning, a precise two-axis joystick with an auto center spring is used. The force-feedback joystick implemented in the system is the Wingman Force made by Logitech. In the Wingman a system of motors and magnetic coils communicates forces to the user hand. Only the X-axis of the force-feedback joystick was used to set the haptic force, which can have positive (away from the user) or negative values (towards the user).

The main program of the graphical interface retrieves the positioning joystick
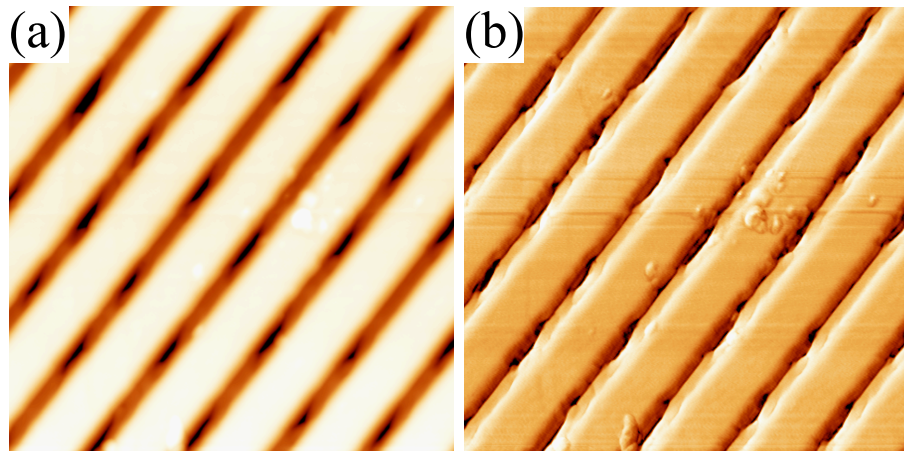
Figure 5.13: AFM image obtained in tapping mode with the NanoManipulator system of the surface of a CD-R surface: (a) surface topography; (b) phase contrast. Image size 15×15 μm^2. Z-range: (a) 200.2 nm; (b) 4.46 degrees.
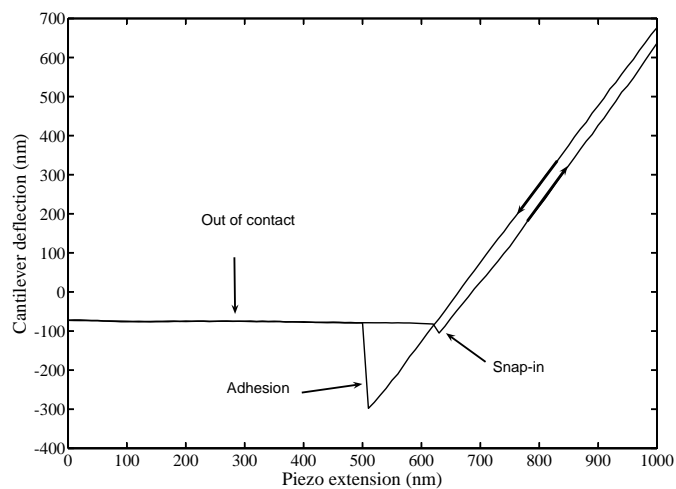
Figure 5.14: Force-distance curve acquired on silicon in ambient conditions by the NanoManipulator system. The main features of the curve, namely snap-into contact instability, region of contact, and withdrawal adhesion, are depicted in the figure.

data and increments the corresponding voltage in the manipulation waveform every millisecond. The sample is moved in the X and Y direction with a velocity proportional to the position of the joystick in each axis relative to its center (see (5.8)). For the vertical positioning of the sample a hat-switch on top of the force-feedback joystick is used. In this case the piezoelectric actuator for vertical positioning is extended or contracted with a constant velocity. The fire buttons of the joysticks were programmed to trigger the manipulation actions.

The acquisition time of the force along the vertical axis of the force-feedback joystick is 1 ms, thus giving the user a real-time interactive signal. To use the force-feedback joystick as a haptic interface between the AFM tip and the user, an interactive signal is A/D converted from the AFM electronics, scaled by the manipulator control system, and returned in the force-feedback joystick. The interactive signal can either be surface topography or tip-sample interaction. The tip-sample interaction is transmitted using the normal cantilever deflection in the static and modulated plowing mode or the cantilever oscillation amplitude in the dynamic plowing mode. The delay between the returned force and the interactive signal is less than 2 ms. Therefore, the user feels a force proportional to the interactive signal almost in real-time.

To provide the user with a real-time feedback of the sample surface, the topography signal from the AFM is fed to the force-feedback joystick while the human operator moves the tip using the positioning joystick. The hand of the user "feels" a force proportional to the height of the sample point interacting with the AFM tip. The topography signal from the AFM electronics is pre-processed in the DSP and then scaled to perform the appropriate response on the force-feedback joystick. The topography signal can be used as an interactive signal as long as the proportional-integral loop of the AFM control system is working. The force set at the force-feedback joystick is proportional to the height of the sample. This proportionality is set in the graphical interface by the user who can thus scale the increment of the height to the range of the feedback force. The user has to choose an amplification range, the height of which correspond to the maximum and minimal forces respectively. All values outside this amplification range drive the feedback force into saturation values.

The user can directly perform surface modification by taking control of the tip with the positioning joystick and setting the tip-sample distance or cantilever oscillation amplitude. If static or modulated plowing manipulation are being performed, then the interactive signal corresponds to the normal cantilever deflection given by the vertical quadrant-photodiode voltage V_{TB}. On the other hand, if the cantilever is being driven at its resonant frequency during manipulation, such as in dynamic plowing lithograpy, then the force set at the force-feedback joystick is proportional to the cantilever oscillation amplitude given by the lock-in magnitude
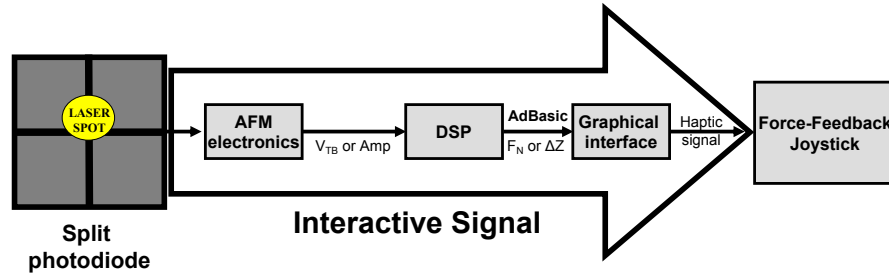
Figure 5.15: Flowchart of the haptic signal generation for joystick steering of the NanoManipulator. The photodiode signal is processed by the AFM electronics to obtain the normal deflection of the cantilever or its oscillation amplitude. These signals are processed by the DSP in order to obtain loading force or sample height which are transmitted to the graphical interface. In the last stage the interactive signal is scaled and sent to the force-feedback joystick.

output M. For both cases the proportionality factor is set by the user in the graphical interface along with the amplification range. The proportional factor depends on the characteristics of the cantilever, sample properties and loading forces onto the sample. Figure 5.15 shows the flowchart of the generation of the haptic signal for the force-feedback joystick.

To illustrate how the tip-sample force is transmitted through the haptic interface, an experiment has been performed where the user drives an AFM cantilever in the tip-sample contact region using the joystick control while the vertical photodiode signal V_{TB} was set as the interactive signal. During the experiment, the vertical piezo displacement V_{TB} and force sent to the force-feedback joystick were acquired. Figure 5.16 shows the acquired data. The amplification range and proportionality factor were chosen to enhance the haptic feeling in the range of values corresponding to the adhesion region of the tip-sample forces and to make positive or negative haptic forces correspond to positive and negative cantilever deflection respectively. In this way the user can sense when the tip is in contact with the sample, the positive force regime, the adhesion force and tip disengagement from the sample.

Figure 5.17 shows two examples of the aplication of the manipulation module to lithography on thin photoresist layers. In Fig. 5.17(a) the micrograph of an ablated structure using the UV-laser of the NanoManipulator is shown. The ablated structure perfectly reproduces the manipulation path previously drawn at the vector-scan module. The line features of the structure once more indicate the high linearity of the positioning piezos over the whole scanning range. This kind of surface nanomachining on thin photoresist films is applied as a first step for micro/nanofabrication [89]. Fig. 5.17(b) shows a structure lithographed using
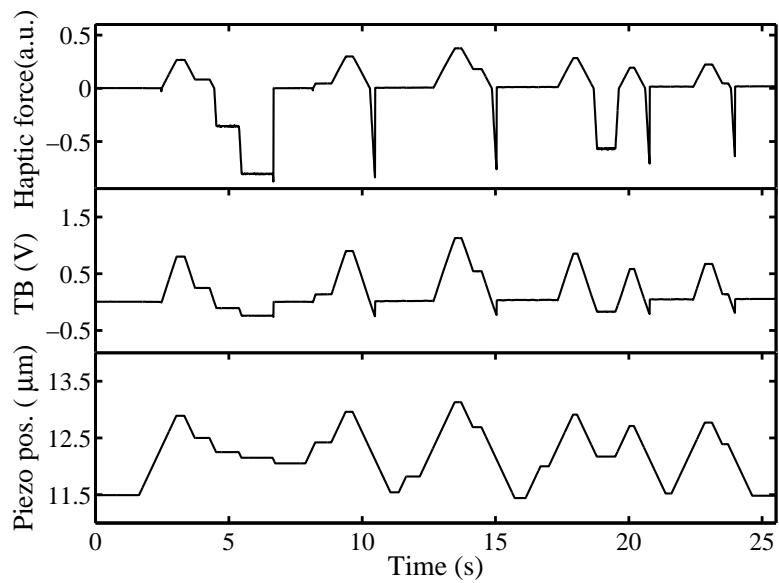
Figure 5.16: Piezo displacement, vertical photodiode signal V_{TB}, and haptic force sent to the force-feedback joystick during a tip approach-retreat experiment where the AFM tip position was controlled directly by the user. The maximum forces at the force-feedback joystick in each direction correspond to +1 and -1 haptic forces respectively.
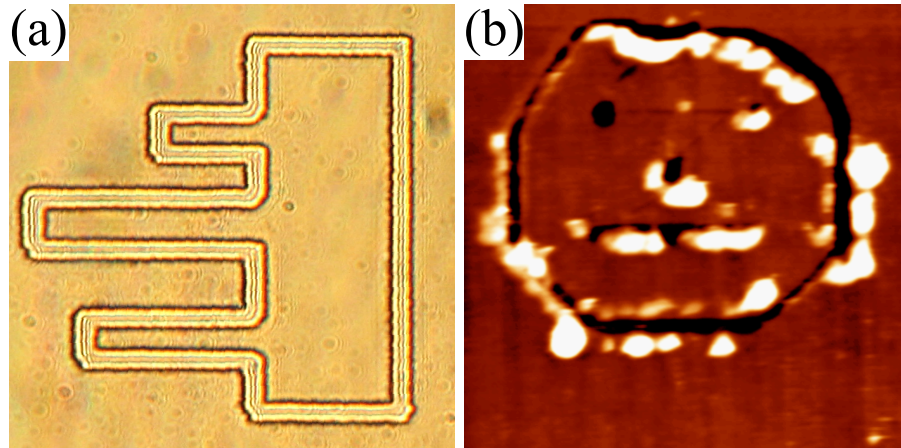
Figure 5.17: Examples of the application of the manipulation module. (a) Optical micrograph of an ablated structure on a thin photoresist layer using the UV-laser of the NanoManipulator and the vector-scan module. (b) AFM image of a lithographed drawing on a thin resist film using the NanoManipulator in the dynamic "nanoscribble" mode. Image size: (a) 120×120 μm^2; (b) 3.4×3.4 μm^2. Z-range (b) 83 nm.

the joystick interface and dynamic AFM manipulation, i.e. the dynamic "nanoscribble" mode. The voltage amplitude for tip displacement was 0.4 V while the writing voltage amplitude was of 0.8 V. When the user pressed the fire button of the position joystick surface modification was succesfully performed. Sample preparation details are given in § 6.1.

5.10   Conclusions

In this chapter we have presented an innovative nanomanipulation system based on the combination of AFM with other experimental methods to extend its capabilities for exploring and modifying surfaces at the nanoscale. The implemented AFM system achieves high resolution characterization of surfaces using different imaging modi such as contact mode, tapping mode and acquisition of force-distance curves. The NanoManipulator system allows the realization of manipulation experiments either by predefining the necessary parameters (vector-scan mode) or by online steering (joystick interface). In the latter mode the human operator handles a positioning joystick whilst obtaining an interactive feedback of the sample surface or the tip-sample interaction through a low-cost haptic interface. Due to the open architecture of the NanoManipulator different methods for AFM lithography and manipulation can be used in combination with UV-laser ablation.

In the following chapters the functional capabilities of the NanoManipulator will be illustrated along with its application for high resolution lithography on thin resist films and dissection of human chromosomes.

Chapter 6

Analysis of AFM plowing lithography on thin photoresist films

The main application of AFM based lithography is the machining of thin polymer films as a first step for semiconductor processing. The lateral resolution achieved by AFM based lithography is mainly limited by the mechanical dimensions of the AFM tip. Therefore, the size of fabricated features can be reduced beyond the light diffraction limit which is the limiting resolution factor in standard methods used in the semiconductor industry. One additional advantage of AFM lithography is that lithography results are studied *in situ* by the AFM itself. However, in the evaluation of lateral resolution in the machining process, the influence of the tip shape must be taken into account [90].

The design of the NanoManipulator allows its reliable application in the field of high resolution lithography due to its high positioning linearity and flexibility of the lithography module. The vector-scan module allows the application of the three standard methods for AFM based lithography: static, modulated and dynamic plowing (see § 2.3). Additionally, the vector-scan module enables the transient acquisition of different system signals to analyze the lithography process.

In this chapter the applicability of the NanoManipulator for the realization and analysis of high resolution lithography on polymers is demonstrated. For that purpose, thin films of a positive tone photoresist, which are applied in the fabrication of microdevices, were modified. Both dynamic and modulated plowing lithography are compared using the acquired transient signals and analyzing the resulted patterns. Additionally, the importance of correct image processing, especially dilation of tip shape, for the evaluation of machined features with lateral dimensions in the nanometer scale is illustrated.

6.1   Materials and methods

The vector-scan module of the NanoManipulator system was used for image acquisition, lithography and transient data acquisition. Topographic images were realized in tapping AFM mode using stiff silicon cantilevers (NSC15/AlBs, Mikro-Masch, Tallinn, Estonia) with a nominal spring constant of 20-75 N/m. The tip shape is conical with a nominal radius of 10 nm. The vector-scan module allows the parameters of each line to be set individually during the lithography experiments. The lithography parameters, that can be individually selected for each line, are line dimensions and position, lithography velocity, vertical positioning piezo extension, voltage amplitude oscillation input at the dither piezo inducing cantilever vibrations and AFM feedback-loop parameters. During the lithography process the AFM feedback-loop was always disconnected. For dynamic lithography the voltage amplitude at the dither piezo was increased to achieve plastic deformation of the surface. The most important parameter influencing line depth in dynamic plowing is the ratio between imaging voltage amplitude and manipulation voltage amplitude. For modulated lithography the vertical positioning piezo was extended to increase the loading force and indenting the tip on the surface. For both lithography methods the preloading force, which is directly related to the used imaging setpoint, also influences the plowing depth because it determines the tip-sample distance during lithography.

To compare and clarify the respective modes of operation of both lithography methods, different transient signals during the trace of a single line were acquired. The acquired transient signals correspond to the average cantilever deflection, cantilever amplitude of oscillation and cantilever base position. The average cantilever deflection is obtained by low-pass filtering the vertical output of the position sensitive detector. The cantilever amplitude of oscillation is obtained from the output of the lock-in amplifier. The cantilever base position corresponds to the extension of the vertical positioning piezo at the AFM-head. The output voltages of the position sensitive detector and lock-in amplifier are directly used to display the cantilever deflection during the experiment since this chapter only offers a qualitative illustration of the lithography process. However, if an evaluation of the applied forces during lithography should be required, this data could be translated to cantilever position by calibration of the position sensitive detector, as shown in § 5.7, and cantilever spring constant.

6.1.1   Preparation of thin photoresist films

A thin polymer film was prepared by spin coating (angular velocty (ω) = 500 min^{-1} for 30 s, ω = 5000 min^{-1} for 60 s) ma-p *1205* (based on Novolak, naphthoquinone diazide, and solvents; MicroChem, Newton, MA) on silicon chips with a size of

about 1 cm^2. Prior to coating the chips were cleaned with acetone, isopropanol and de-ionized water. After spinning the samples were dried on a hot plate at 100°C for 40 s.

6.1.2 Image processing

The acquired images were processed using the SPIP^{TM} software package (Image Metrology ApS, Lyngby, Denmark). The following processing procedure was used: (i) first, the raw data was flattened to remove image tilt; (ii) a 3×3 linear low-pass gaussian filter was used to reduce noise that would cause an underestimation of the tip radius in the characterization process; (iii) a blind tip-reconstruction algorithm was applied [10, 11] on the processed image to calculate the "worst case tip", i.e. the maximum tip shape which is able to reconstruct the imaged surface; (iv) finally, the estimated tip-shape is deconvoluted from the acquired image. In the processed images an upper constraint is set for groove lateral dimensions, while a lower constraint is set for bumps. Height measurements of steps are not greatly affected in the deconvoluted images. Line width values given in this chapter correspond to the full width at half maximum (FWHM).

6.2 Experimental results and discussion

Figure 6.1 shows the transient signals acquired during the dynamic plowing of a single line. When the line lithography is started the AFM feedback-loop is disconnected[1] and the internal oscillator output voltage of the lock-in amplifier is set from 2.5 V to 5 V. Due to the lock-in internal switch, the amplitude output falls to zero before the new voltage is set. From the transient signal graph a jump from 0 to 0.9 V of the average tip position output from the position sensitive detector V_{TB} can be observed responding to the increase of cantilever amplitude which is reflected directly in the amplitude output of the lock-in amplifier. While the line is being traced the transient signals remain constant although a slight decrease is observed in the amplitude, probably due to sample tilt. When the line trace is finished the oscillator voltage is set to its original value and the feedback-loop is reconnected. In the transient signals it is observed how the cantilever average position returns to near zero deflection. The amplitude falls momentarily to zero due to the lock-in internal switch and returns to a region close to the original value. The reconnection of the feedback-loop is clearly seen in the piezo extension signal, which reacts abruptly to the difference between amplitude and setpoint.

The transient signals corresponding to the traced line in the modulated mode

---

[1]If the feedback-loop is active during plowing, the applied load on the sample during plowing is not incremented respect to the applied load used for imaging [91].
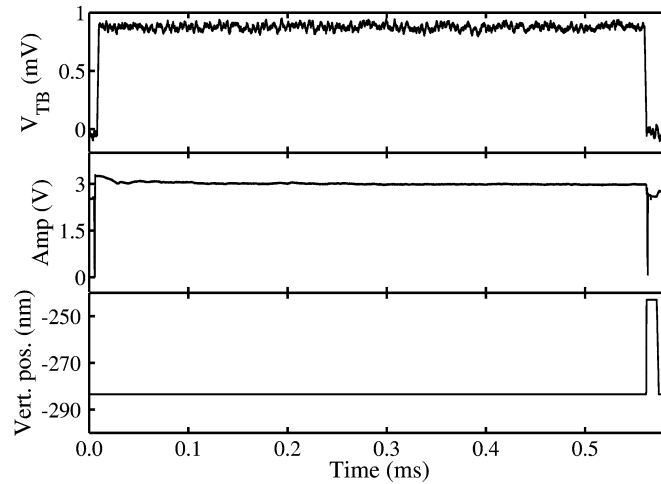
Figure 6.1: Transient data acquired during the dynamic plowing lithography of a single line: filtered deflection signal (V_{TB}), lock-in amplitude (amp), and vertical positioning piezo extension (vert. pos.). The used manipulation parameters were: imaging voltage 2.5 V; imaging setpoint 0.5 V; manipulation voltage 5V; tip velocity 1 μm/s. The lithography resulted in a graved furrow with a line depth of 25 nm and 90 nm width.

are shown in Fig. 6.2. At the beginning of the line the gradual extension of the positioning piezo and the correspondent gradual decrease of cantilever oscillation amplitude can be observed. When the vertical piezo reaches its complete extension no cantilever oscillations are observed. The average cantilever deflection starts to decrease when the piezo extension reaches 228 nm, which corresponds to the cantilever amplitude of oscillation before the vertical piezo is extended. The decrease of the average cantilever deflection in response to the vertical piezo extension from 228 nm to 250 nm indicates an effective loading force during plowing of 0.64-2.40 μN, estimated by Hooke´s law and using the nominal spring constant of the cantilever. During line tracing no major variations of the signals are observed. However, if the unfiltered deflection signal is considered (see inset in Fig. 6.2), it is seen that during manipulation the applied force is modulated by the dither piezo excitation. As a hyphothesis, this force modulation can be responsible for the decrease of lateral forces which leads to edge irregularities during static plowing, i.e. machining the surface without any applied modulation [31, 33, 34, 35]. At the end of the line the positioning piezo is set to its original position and the feedback-loop is reconnected, restoring the transient signals to their original values.

The experiments carried out by dynamic plowing lithography showed similar results to those of previous studies on similar materials, in particular, a linear dependence of lithographed depth with increasing amplitude is observed [80, 92].
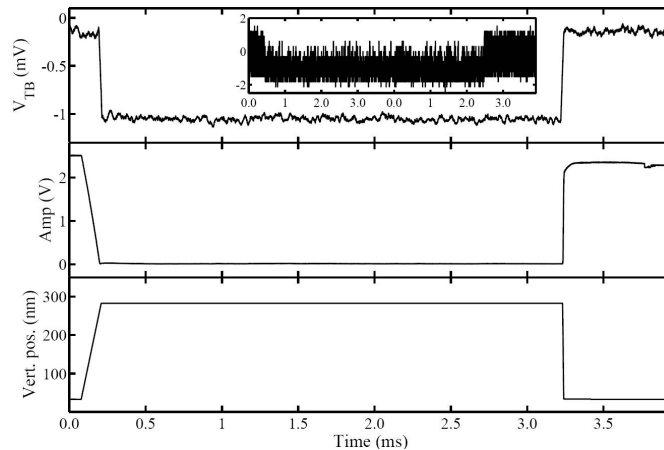
Figure 6.2: Transient data acquired during the modulated plowing lithography of a single line: filtered vertical deflection signal (V_{TB}), lock-in amplitude (amp) and vertical positioning piezo extension (vert. pos.). The inset shows the unfiltered vertical deflection signal, confirming that the load force is modulated during the modulated plowing process. The used manipulation parameters were: imaging voltage 2.5 V; imaging setpoint 0.5 V; piezo extension 250 nm; tip velocity 1 μm/s. The lithography resulted in an engraved furrow with a line depth of 3.5 nm and a width of 46 nm.

However, as Fig. 6.3 shows, in the lithography process huge bumps were produced in the furrows. Raised polymer areas after machining for loads below the yield strength of the polymer [93] and for dynamic plowing lithography [91] have been previously reported. This effect can not be attributed merely to material displacement during plowing due to the fact that the raised polymer volume exceeds greatly that of the engraved furrows. Other processes must therefore be involved where material properties modifications take place. Morphological changes of polymer molecules induced by viscoelastic effects, localized heat or the creation of cavities in the produced bumps have been proposed as an origin of this phenomenon [94]. Interestingly, material raising on thin polymer layers has also been reported in AFM-assisted electrostatic lithography (AFMEN) [49]. Here a combination of Joule heating with mass transport of softened polymer liquid in the non-uniform electric field has been proposed as generation mechanism of raised material. This enforces the hypothesis that tip oscillations induce a transition of polymer viscoelastic properties which, combined with tip-polymer adhesion, generates the observed bumps. Due to bump generation it is not possible to achieve reliable groove fabrication by dynamic plowing lithography of the investigated photoresist film. The generated bumps would complicate any postprocessing of the films necessary for structuring of the underlying substrate. However, the possibly
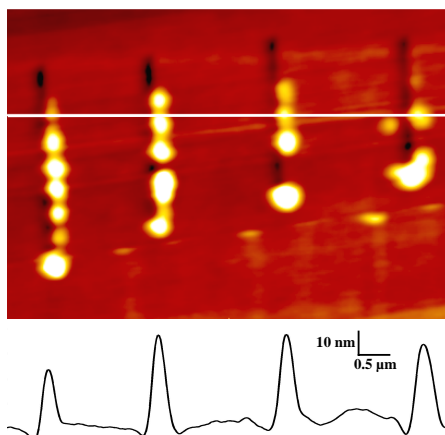
Figure 6.3: Deconvoluted AFM image and correspondent height profile along the white line of four lines lithographed by dynamic plowing on a thin photoresist film. The used manipulation parameters for the four lines were: imaging voltage 0.1 V; imaging setpoint 0.05 V; manipulation voltage 0.5 V; tip velocity 1 μm/s. Image size 4.8×6.9 μm^2. Z-range 118.3 nm.

generated bumps could also be used for a specific purpose, e.g. high density data storage devices.

In contrast, the application of the second method, modulated plowing, showed different characteristics of the lithographed patterns. The generation of bumps observed previously is no longer present and the features lithographed on the photoresist layer are reliably fabricated. Figure 6.4 shows six lines lithographed by modulated plowing with different piezo extensions. From the image the high influence of piezo extension on line depth and width is clearly seen as illustrated in the annexed data plot. Plowing depth depends linearly on the piezo extension, and hence on the loading force applied by the cantilever. It is observed in the graph how the steady increment of line width is only valid for low piezo extensions. For the last two lines no increment in line width is observed. This effect can be attributed to the influence of the tip shape on the line width, indicating a deviation from the conical shape at the apex of the tip used for this experiment. The conducted tip shape analysis estimation indicates that the tip was adequate for the lithography experiments with an estimated tip radius of 25 nm. The upper limit for width of the thinnest line is 97 nm, obtained from the processed image, while the lower limit, obtained from the raw data image, is 63 nm.

Finally, the influence of tip shape in the analysis of high resolution lithography by AFM is illustrated in Fig. 6.5. The figure shows the raw data and processed image of a single line lithographed by modulated plowing. The blind tip estimation indicates that a rather blunt tip was used in the experiment with an estimated
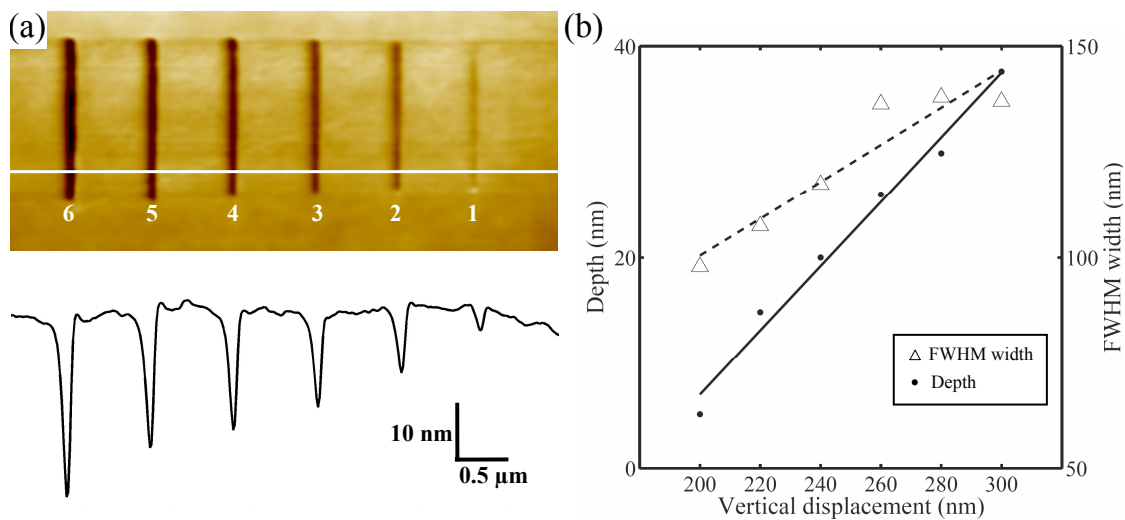
Figure 6.4: Six lines lithographed by modulated plowing on a thin photoresist film with varying piezo extension. (a) Deconvoluted AFM image and corresponding height profile along the white line. The parameters used for the lines were: imaging voltage 2.5 V; imaging setpoint 0.5 V; piezo extension (#1) 200 nm, (#2) 220 nm, (#3) 240 nm, (#4) 260 nm, (#5) 280 nm, (#6) 300 nm; tip velocity 1 μm/s. Image size 3.0×6.8 μm^2. Z-range 66.56 nm. (b) Dependence of line depth and width on vertical piezo extension.
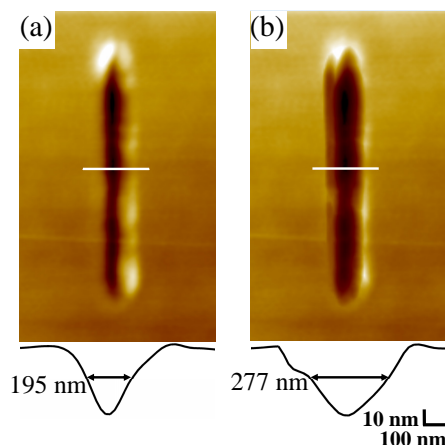
Figure 6.5: Single line lithographed by modulated plowing. (a) Raw data image and correspondent line profile along the white line. (b) The same image after tip deconvolution. Tip deconvolution reveals that lateral dimensions of lithographed features can be considerably underestimated without image restoration. Also note that the profile of the cut cross section changes as a consequence of the own shape of the estimated tip. Image size 4.2×2.5 μm^2. Z-range (a) 71.5 (b) 66.6 nm.

tip radius of 47 nm. The analysis of the unprocessed image gives a line width of 195 nm. In contrast, the deconvoluted image set the upper limit of the line width at 277 nm. Therefore, if the raw data is analyzed without considering tip effects on the measurement of the lateral dimensions, it is possible to underestimate the width of the lithographed feature by 45%. The deconvoluted image not only shows how the line width is increased by image restoration, but also that tip deconvolution changes the profile of the AFM image of the lithographed furrows.

6.3   Conclusions

In this chapter the application of the NanoManipulator system for the high resolution lithography of thin photoresist films has been illustrated. For lithography realization two different methods were applied and compared. The NanoManipulator not only allows the realization of high resolution lithography, but also offers an insight into the process by the acquisition of transient signals during plowing. Moreover, we have observed that in modulated plowing, the cantilever average deflection directly gives the load force applied during lithography. Assuming that lithography depth is directly related to applied load force, the average cantilever deflection seems to be an appropiate control parameter for online control of AFM modulated plowing. Dynamic plowing lithography on the photoresist used in our

study showed bump generation. In our experiments, the high dimensions of the bumps makes it difficult reliable fabricating of uniform lines necessary for film postprocessing. In contrast, modulated plowing lithography does not show bump generation, and therefore reliable surface structuring can be realized. A minimal line width of 97 nm, which is beyond the light diffraction limit, was achieved using a standard commercial AFM tip. Note that lithography lateral resolution could be increased using AFM tips with a high aspect ratio [95].

Although it has been claimed that dynamic plowing is advantageous compared to the modulated method due to the reduction of lateral forces acting on the tip during lithography, our application shows that other effects due to material properties, mainly plasticity of the substrate, greatly affect the process realibility. In any case, for different substrates and depending on their material properties, dynamic or modulated plowing methods must be studied in detail to decide which of them offers a better lithography performance.

Additionally, the influence of tip shape in lithography analysis has been illustrated by an experiment where a low quality AFM tip was used. Due to the lack of reliable tip fabrication in commercially available AFM sensors, such a case is not rare in AFM experiments. Surprisingly, although AFM lithography is being thoroughly investigated with the goal of reducing the lateral dimensions of surface structures, tip deconvolution is seldom applied in experimental analysis.

Previous work in the field of AFM lithography has shown that both lithography methods presented in this chapter have demonstrated their utility in surface structuring. However, new methods providing major process control and that can be applied for diverse AFM system configurations are needed. In Chapter 8 a novel method for the structuring of thin films is presented. This method is based on the coupling of a shear acoustic wave to the AFM tip to achieve high resolution lithography.

Chapter 7

Combined nanomanipulation by atomic force microscopy and UV-laser ablation for chromosomal dissection[1]

The combination of AFM with other experimental methods such as optical microscopy and UV-laser ablation represents a versatile approach for analyzing, handling and manipulating biological objects on the nanometer scale. One of the most interesting applications is the high resolution study of human metaphase chromosomes in different ambient conditions [96, 97, 98, 99]. However, the DNA contained in the chromosome and enclosing the genetic information can not be analyzed with standard microscopy methods.

Currently, the standard approach for the analysis of DNA is the sequencing of the whole genome which represents an immensely time-consuming procedure. One alternative is to analyze only a limited region of the genome by isolating DNA samples using microdissection methods. The dissected material can be used for various analysis applications including the generation of probes for fluorescence *in situ* hybridization (FISH), physical mapping for cytogenetic analysis [100] and the generation of chromosome band-specific libraries [101]. Dissection methods using a glass needle are not sufficiently accurate, and the amount of recovered biomaterial is still not reduced to a sufficiently small size to target single regions of the genome. For this application both UV-laser chromosomal fragment isolation and

---

[1]This chapter has been partly published in: F. J. Rubio-Sierra, W. M. Heckl, R. W. Stark (2005): *Nanomanipulation by atomic force microscopy*, Adv. Eng. Materials, 7(4), p. 193-196, and F. J. Rubio-Sierra, R. W. Stark, S. Thalhammer, W. M. Heckl (2003): *Force feedback joystick as a low cost haptic interface for an atomic force microscopy nanomanipulator*, Appl. Phys. A, 76, pp. 903-906.

AFM based dissection represent promising alternatives.

Optical manipulation of chromosomes using laser systems was already shown in the 1960s [102]. Laser microdissection was firstly applied for the generation of DNA libraries for the painting of chromosomal regions by Lengauer *et al.* [103]. Another significant advance was to recover the isolated DNA material by UV-laser catapulting for subsequent chemical analysis [104]. Currently, UV-laser based micromanipulation is a standard technique in the field of biomedicine, e.g. [105, 79, 106, 107]. The underlying mechanism involved in UV-laser ablation is local ablative photodecomposition, as revealed by studies in synthetic materials [108, 109]. However, the UV absorption contributions in structural biological material are difficult to determine. Probably the major contribution to UV absorption comes from water, small organic molecules and inorganic ions invariably present in biological material.

As we have already emphasized in this work the AFM actually represents the most versatile approach for manipulation at the nanometer scale. Taking advantage of its high positioning capability, AFM based dissection is a valuable tool for the generation of DNA samples. Henderson demonstrated that minute pieces of supercooled plasmid DNA can be dissected and manipulated by AFM [110]. Single DNA fragments were isolated and extracted for subsequent PCR amplification by Lü *et al.* [111]. Recently, numerous investigations are being conducted to optimize the direct extraction of minute amounts of DNA from localized chromosomal regions using the AFM [112, 113, 34, 114, 115, 115]. However, reproducibility and operation methodology must be improved to establish AFM-based manipulation on chromosomes as a standard method in biomedicine.

A combined experimental setup such as the NanoManipulator system is an ideal tool for the handling of biomaterial. Optical microscopy allows for fast specimen recognition and AFM tip positioning on the sample region of interest for manipulation. Further, high resolution *in situ* imaging of the specimen and manipulation analysis is provided by AFM. Due to automated manipulation and haptic interfacing, the NanoManipulator is a reliable and user-friendly system, which is particularly advantageous for the operation of the system by inexperienced users. The combination of UV-laser ablation and AFM mechanical dissection in one single instrument with the possibility of interactive user control extends the capabilities of current methods for the extraction of minute amounts of biomaterial.

In this chapter we illustrate the use of the combined manipulation system for the dissection of human metaphase chromosomes. Chromosomal regions are isolated either by photonic ablation or by AFM based mechanical microdissection, both with user interactive control. The results of the manipulation are *in situ* analyzed by AFM imaging directly after manipulation.

7.1 Materials and Methods

The experiments on chromosomal dissection presented in this chapter were performed using an earlier prototype of the NanoManipulator system. In this version of the NanoManipulator the positioning stages were not scan-linearized, and therefore the AFM positioning stage had to be properly calibrated prior to the experiments. In order to account for the non-linearity of the open-loop controlled piezoelectric actuators a 5% error is assumed for topographical data (reflected in the imaging of a calibration standard). Topographic images were obtained in AFM tapping mode using stiff silicon cantilevers (Pointprobe. NCH, Nanosensors Dr. Olaf Wolter GmbH, Wetzlar, Germany) with a nominal spring constant of 21-78 N/m and a nominal tip radius of 20 nm.

All the images and their corresponding metrological analysis presented in this chapter have been processed by tip shape deconvolution from topographic data as illustrated in § 6.1.2. Note, that all the lateral dimensions given in this chapter correspond to upper limit values set by the estimated tip shape.

To dissect the specimen by non-contact ablation the laser energy was adjusted to about 1 μJ/pulse and the sample was moved through the focus by the piezoelectric transducers of the scanning probe microscope. For mechanical AFM manipulation, the same type of cantilever as used for imaging was employed. Dissection was achieved by modulated plowing, i.e. the loading force of the tip onto the sample was increased by extension of the vertical piezoelectric positioner. The driving modulation for the dynamic mode of the cantilever base was maintained to decrease the lateral forces acting on the AFM tip, ensuring precise dissection of the biological material [31, 33, 34, 35]. Dissection was performed at an average scan speed of 0.5 μm/s. The cantilever was calibrated following a standard procedure [116] and the calibrated spring constant had a value of 60 N/m $\pm$ 5 N/m.

7.1.1 Human metaphase chromosomes

For the preparation of human metaphase chromosomes, heparinized human blood (0.4 ml) was cultivated at 37° C for 72 h in 10 ml GibcoTM Chromosome medium 1A (Invitrogen GmbH, Karlsruhe, Germany). Cells were arrested by a 30 min colchicine treatment (100 μl) followed by centrifugation (10 min at 1000 rpm). Chromosomes were prepared by resuspending the pellet in 10 ml 0.075 M KCl and incubation at 37° C for 15 min. After a further centrifugation (10 min at 1000 rpm) the pellet was carefully resuspended in a freshly prepared mixture of 3:1 metanol acetic acid at 4° C and fixed for 25 min at 4° C. After three washing steps in the metanol acetic acid fixative the chromosomes were dropped onto 0.17-mm-coverslips, rinsed in PBS and air-dried.

The chromosomes where classified using the method based on the criteria length

and centromere index, i.e. the ratio of the length of the short arm to the chromosome length ×100 [117]. Both features are considered the most discriminative geometric features of human metaphase chromosomes [118].

7.2 Experimental results and discussion

Previous to dissection, spreads of chromosomes were easily located using the light microscope with the 10× achromat long distance objective. Then the AFM tip was placed on the spread and a high-resolution AFM image was acquired. The chromosome number 2 in the standard classification of human metaphase chromosomes was selected for photonic ablation. The chromosome was identified considering the size and centromer position of the chromosome measured from the AFM image.

The 100× 1.20 Glyc Ultrafluar oil immersion objective was selected for photonic ablation and the laser focus was precisely adjusted using the vertical piezoelectric stage in the sample holder. Then, using the vector-scan module of the manipulation software, six cuts were performed on the selected chromosome with a fixed microdissection velocity of 0.3 μm/s, a pulse energy of 0.68 μJ and a pulse repetition rate of 60 Hz. Immediately after the dissection an AFM image was acquired to check ablation results.

The minimal cut width was achieved in cut #L1, with a FWHM width of 380 nm. The chromosome was fully dissected and the cut reaches down to the substrate with a sidewall angle of 60°. The laser cuts #L1 and #L2 are separated by 850 nm and a 420-nm-wide chromosomal fragment remained in between, corresponding to a volume of approximately 0.2 μm^3. This remaining isolated volume contains about 4000 DNA base pairs. Thus, using the UV-laser beam sharp and precise cuts could be obtained where the entire chromosomal material within the cut was ablated. The steep sidewalls of the cuts indicate that very precise cuts can be performed in chromosomal material, which is necessary for the localized isolation of DNA material and its subsequent chemical analysis. Exclusively using microscopic methods it is not possible to discern if the remaining chromosomal material close to the cut region can be used for genetical analysis. However, a detailed look at the height-profile measurement reveals that the height of the remaining fragment between both laser cuts #L1 and #L2 remains unchanged, suggesting that the genetic material should be unaltered after ablation. Comparing this experiment with earlier investigations on chromosome UV-laser manipulation, the achieved minimum cut size could be reduced significantly from 650 nm to 380 nm. This is probably a result of the focusing precision achieved in our system. Table 7.1 lists the FWHM values of the achieved cut widths by the UV-laser dissection.

After the ablation experiment a medium sized submetacentric chromosome next to the ablated one was selected for mechanical dissection by modulated plow-

	L_1	L_2	L_3	L_4	L_5	L_6
Width (nm)	380	405	521	411	387	382

Table 7.1: FWHM values of cut widths achieved by UV-laser ablation on the right chromosome of Fig. 7.1.
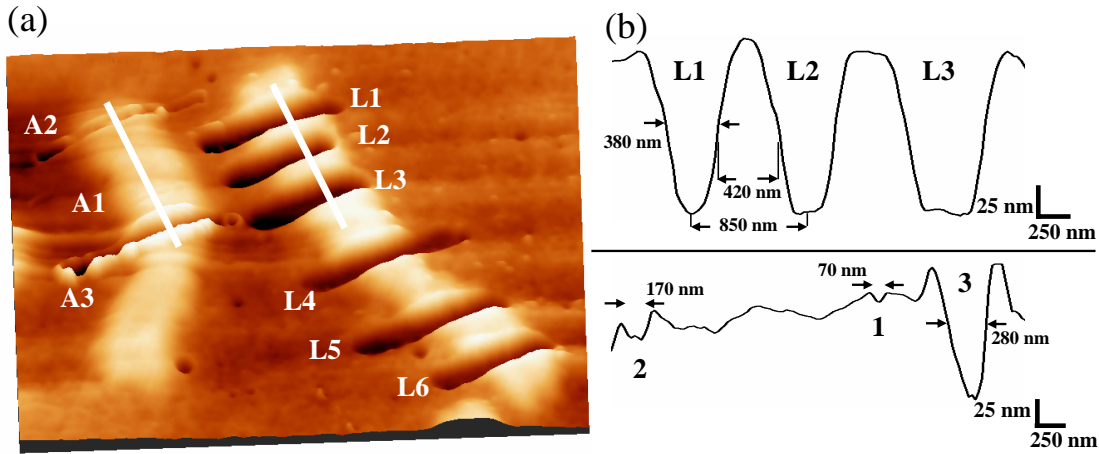

Figure 7.1: Combined mechanical dissection and non-contact laser ablation on human chromosomes. (a) Pseudo 3-dimensional representation of topographic AFM data showing mechanical AFM dissection (left chromosome, cuts A1-A3) and UV-laser photo ablation (right chromosome, cuts L1-L6). Image size 7.7×11.4 μm^2. Z-range 341.9 nm. (b) The corresponding cross-sectional analysis is shown as height diagrams, which are plotted along the white lines of the AFM image.

ing. Three different cuts were performed by taking control of the system using the joystick stage. At first, a superficial scratch of 20 nm depth and 70 nm width was made by applying an average tip loading force of 10 μN of the tip onto the sample (cut number #1 in Fig. 7.1). Then, the average loading force was increased to 20 μN and a cut of 50 nm depth and 170 nm width was performed (cut number #2 in Fig. 7.1). Finally, the chromosome was fully dissected by the application of an average loading force of 40 μN, realizing a cut of 160 nm depth and 280 nm width (cut number #3 in Fig. 7.1). Debris material was deposited next to the cuts by the plowing process. Although no chemical analysis was performed on the AFM tip after the dissection experiment, it can be expected that at least a minimal amount of the dissected material remains adhered to the AFM tip after dissection [79, 34]. Figure 7.1 shows both manipulated chromosomes after the combined mechanical and photonic dissection experiment.

In the mechanical dissection experiments it was observed that for high values
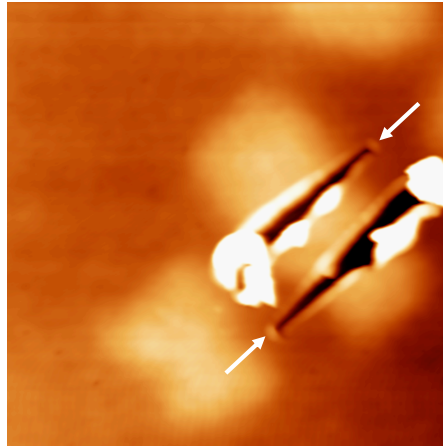
Figure 7.2: Human metaphase chromosome after mechanical microdissection with high applied loads. The arrows indicate the directions of each cut. White upheavals in the image correspond to debris formed massively during microdissection. The chromosome appears with a low contrast in respect to the background because of its low height difference compared to the accumulated debris. Image size $10{\times}10$ μm^2. Z-range 350.2 nm.

of the applied load of the AFM tip onto the sample, a widening effect of cut width in dissection direction was observed. Fig. 7.2 shows a human metaphase chromosome after the realization of two cuts by mechanical dissection. Each cut was performed in a different direction with applied loads of 70 and 75 μN, respectively. The progressive increase of the cut width in the direction of the dissection can be observed in the AFM image. Both cuts completely dissected the chromosome and, due to the high load, a considerable amount of debris was accumulated at the end of the cuts. Higher loads during dissection considerably diminish force modulation, consequently increasing the magnitude of the lateral forces acting on the tip.

7.3   Conclusions

In this chapter, it has been shown that an instrument that combines AFM nanomanipulation with UV-laser surgery represents a very efficient approach for the manipulation of human metaphase chromosomes. Chromosomal dissection with a high spatial resolution, as achieved by the combined setup, is an important requirement for the generation of genetic samples for high-resolution cytogenetical analysis. Haptic interfacing helps enhance system operation and allows the human operator to explore and manipulate biological objects in an environment that is

very distant in scale.

AFM imaging combined with optical microscopy enables the rapid selection and identification of human chromosomes. Additionally, AFM enables an *in situ* characterization of the resulted manipulation. The UV-laser microdissection of metaphase chromosomes with this new experimental set-up yields a better cut resolution as compared to previous work. Usually, systems for laser ablation move the sample by using a step-motor-based positioning system. The use of the piezoelectric actuators of the NanoManipulator to focus and move the sample during laser ablation optimizes the laser focusing and the energy deposited by the laser on the sample, minimizing thermal effects. Our instrument shows that with a standard nitrogen laser system a cut width of less than 380 nm is possible in human metaphase chromosomes. Additionally, our system implements a semi-automated environment for mechanical nanodissection below the light diffraction limit using the AFM tip. In this case, the minimum cut width is only limited by the mechanical dimensions of the AFM tip. Moreover, this method also offers the possibility of a localized extraction of minimal amounts of DNA for subsequent chemical analysis. The joystick system allows the implementation of a low-cost interactive interface to improve user-guided steering in the dissection process.

Chapter 8

Acoustical force nanolithography[1]

In Chapter 6 we have illustrated the application of the different approaches which are currently used for mechanical machining by AFM. The static approach relies on the application of a static load on the sample to produce plastic deformation while the AFM tip moves over the surface. It has been claimed that the lateral forces caused by this static method affect the controllability of the process when applied on thin films with low substrate adhesion [31, 33, 34, 35]. In the second approach, modulated and dynamic plowing, the applied forces during manipulation have an oscillating character which minimizes unwanted lateral forces during the lithography process [33]. However, modulated and dynamic plowing presents some drawbacks in their application:

- As we have shown in Chapter 6, dynamic plowing can generate unwanted sample deformation in some soft materials in the form of bumps which affects process reliability or makes difficult postprocessing of the modified material.

- In the theoretical transfer study in Chapter 3, we have demonstrated that the controllability of standard dynamic plowing is limited by the fact that cantilever actuation strongly depends on the transfer characteristics of the dithering piezo-element and the cantilever: the fixed end actuation of the cantilever introduces a time-delay in the system between the actuation and the tip displacement. This can limit the bandwidth of high-speed closed-loop control of the machining process as illustrated in Chapter 3.

- The non-linear tip-sample interaction produces a strong shift of the cantilever resonant frequency, which reduces the forces that can be applied during dynamic plowing lithography.

---

[1]This chapter has been partly published in: F. J. Rubio-Sierra, A. Yurtsever, M. Hennemeyer, W. M. Heckl, and R. W. Stark: *Acoustical force nanolithography of thin polymer films*, Phys. Stat. Sol. (a), 203 (6), pp. 1481-1486, 2006

- In commercial systems, dynamic and modulated plowing can be difficult to implement since internal signal accessing is needed. Additionally, process control can be limited by lack of system flexibility.

In this chapter "acoustical force nanolithography" is presented, a novel surface machining method based on the AFM, and the corresponding setup necessary for its easy implementation in a commercial microscope. In order to avoid the hardly controllable stick-slip oscillations of static plowing lithography, the oscillations are induced by a normal incidence shear acoustic wave. Prior to lithography the frequency response of the cantilever is acquired to obtain the optimal operation frequency. The influence of the main experimental parameters such as excitation frequency, amplitude and the preloading force are investigated in detail.

8.1   Materials and methods

The experiments were carried out on a Dimension 3100 Scanning Probe Microscope System (Veeco Metrology, Santa Barbara (CA), USA). Lithography paths were programmed using the NanoMan II software of the instrument. For the process parameter characterization a triangular cantilever with a nominal force constant of 48 N/m was used (NSC11, MikroMasch, Tallinn, Estonia). For the lithography examples described in § 8.6 a rectangular cantilever with a nominal force constant of 40 N/m was used (NSC16, MikroMasch, Tallinn, Estonia). As illustrated in Fig. 8.1 the sample was mounted on a normal incidence shear wave transducer (v153, Panametrics-NDT, Waltham (MA), USA). For lithography, a continuous sinusoidal signal was coupled to the ultrasonic transducer. To switch between imaging and lithography mode the sample bias voltage signal of the AFM controller was used as a trigger signal; this signal can be accessed through a signal access module. In this modified lithography system the sample holder is electrically isolated from the sample bias voltage signal of the controller[2].

   All images have been acquired in standard tapping mode where the dither piezo of the cantilever holder is used for excitation. For image processing a commercial software package was used (Image Metrology ApS, Lyngby, Denmark). In order to obtain a reliable measurement of the width of the lithographed structures, the influence of the tip-shape on the measured topography had to be considered. All the images and their corresponding metrological analyses presented in this chapter have been processed by tip shape deconvolution from topographic data as illustrated in § 6.1.2.

   The thin photoresist films were prepared as described in § 6.1.1.

---

[2]Due to the setup necessary for the coupling to the acoustic wave, this method is more appropiate for a probe-scanning system like the Dimension 3100.
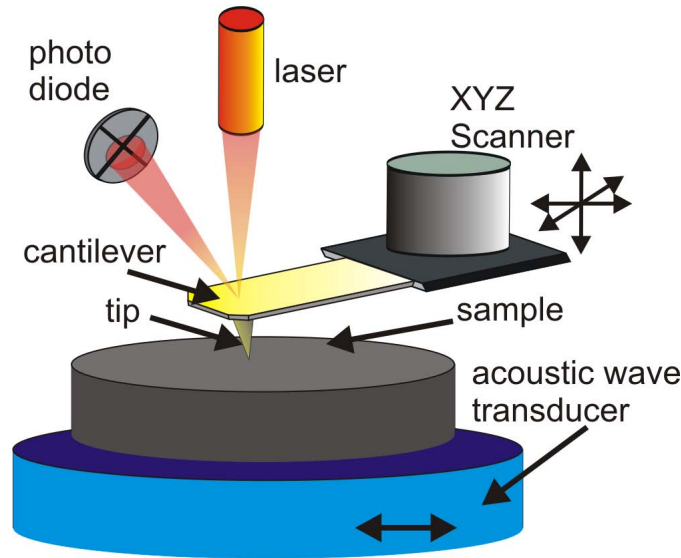
Figure 8.1: Experimental setup for acoustical force nanolithography. The sample holder consists of an acoustic wave transducer that is used to enhance cantilever flexural vibrations for lithography.

8.2 Characterization of process parameters

8.2.1 Resonance spectra

In order to tune the excitation frequency for lithography the frequency response of the cantilever to an excitation by a continuous single tone of the ultrasonic transducer was analyzed. Two different types of vibration spectra were acquired: one for the free cantilever and one for the surface-coupled cantilever. The excitation frequency was swept stepwise over the frequency band from 400 kHz to 1 MHz. The vibration spectra of the AFM cantilever were measured by demodulation of the deflection signal with an external lock-in amplifier (7280, Ametek, Oak Ridge, TN). The frequency response of the free cantilever is shown in Fig. 8.1. The cantilever was placed about 2 μm over the sample surface during the measurement of the frequency response. The out-of plane oscillations of the vibrations of the ultrasonic transducer couple through the air to the cantilever. Only one resonance peak appeared at a frequency of 423.4 kHz within the analyzed frequency band. In order to acquire the resonance spectra of the surface-coupled cantilever, the vibrating AFM cantilever is brought into intermittent contact by approaching the cantilever to the surface until the AFM cantilever oscillation amplitude was reduced to 20%. Then, the microscope feedback-loop was disconnected and the vibration spectrum was acquired. Figure 8.2 shows the vibration spectrum with several resonance peaks. The main resonance peak is shifted and obscured by new resonances in the
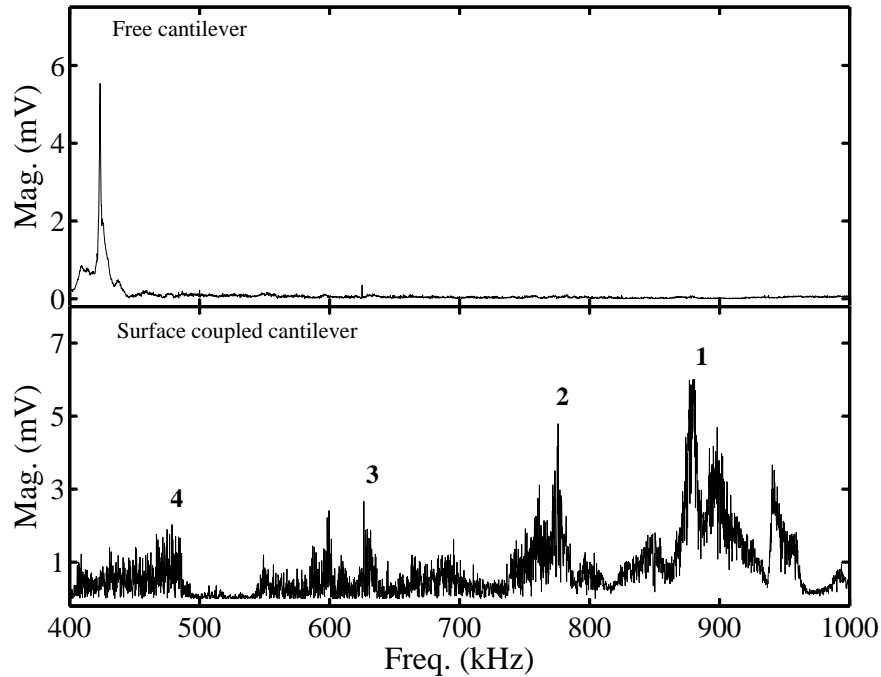
Figure 8.2: Vibration spectra of the freely vibrating and the surface-coupled cantilever. The numbered peaks in the surface-coupled spectrum were used to characterize the influence of the frequency response in the lithography process (see Fig. 8.3).

spectrum. These new resonances are caused by the strongly non-linear character of the tip-sample interaction and by resonances in the frequency response of the acoustic transducer [62, 52], as predicted by the dynamic model of the cantilever presented in Chapter 3. Six major resonance peaks are located at f = 477.0, 598.2, 637.8, 777.2, 879.6, and 940.8 kHz. The response of the system close to 1 MHz is enhanced due to the frequency response of the acoustic wave transducer which is centered at this frequency.

8.2.2   Acoustic wave frequency

The frequency response of the surface-coupled cantilever of Fig. 8.2 implies that the vibration amplitude strongly depends on the excitation frequency. In order to analyze this relation quantitatively, four traces were lithographed at different resonance peaks of the surface-coupled cantilever frequency response in order to characterize the influence of the excitation frequency (1 V signal amplitude). Figure 8.3 (a) shows the resulting traces and the height profile. All traced lines successfully plowed grooves on the sample surface. Residual material from the
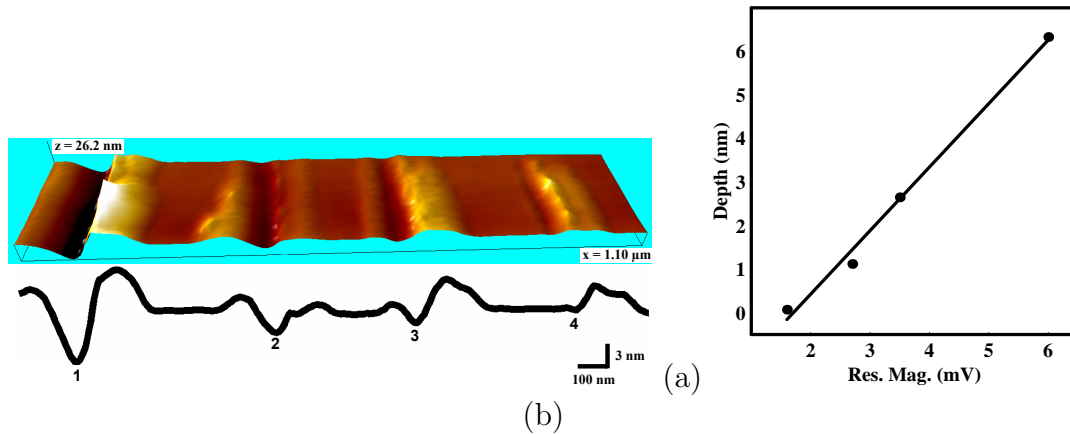
Figure 8.3: Variation of lithography depth with the resonant magnitude of the surface-coupled frequency response (Fig. 8.2). The resonant magnitudes and corresponding excitation frequencies for the four different traces were: trace #1, 6.0 mV (at 879.4 kHz); trace #2, 3.5 mV (at 774.2 kHz); trace #3, 2.7 mV (at 626 kHz); trace #4, 1.6 mV (at 479.4 kHz). (a) 3D-representation and height profile of the patterned area. (b) Increase of lithographed depth with the frequency response magnitude of the resonance peak (circular dots). A linear fit of the experimental data is also given.

plowing process appears at both sides of the grooves. From the results it is clearly seen that the lithographed depth is directly related to the resonance peak which is used to generate the acoustic wave. Figure 8.3 (b) shows that the lithographed trace depth increases with the magnitude of the resonance peak roughly linearly in the studied interval.

8.2.3 Acoustic wave amplitude

The vibration amplitude of the surface-coupled cantilever and, consequently, the applied tip-sample forces depends directly on the magnitude of the excitation. To characterize the influence of the acoustic wave amplitude on the lithography process, six lines were lithographed using the same frequency (940.8 kHz) but at different magnitudes of the excitation signal. The first line was performed without acoustic wave excitation. All the lines traced with acoustic wave excitation resulted in the fabrication of grooves. Figure 8.4 (b) shows a slight deviation from a linear relation between acoustic wave magnitude and lithographed depth. From Fig. 8.5 (a) it is evident that the sample surface appears raised next to the groove. In Chapter 6 we could observe a similar effect when dynamic plowing lithography was applied on the same polymer. However, using acoustical force lithography the size of the raised polymer is much lower and does not impede the reliable
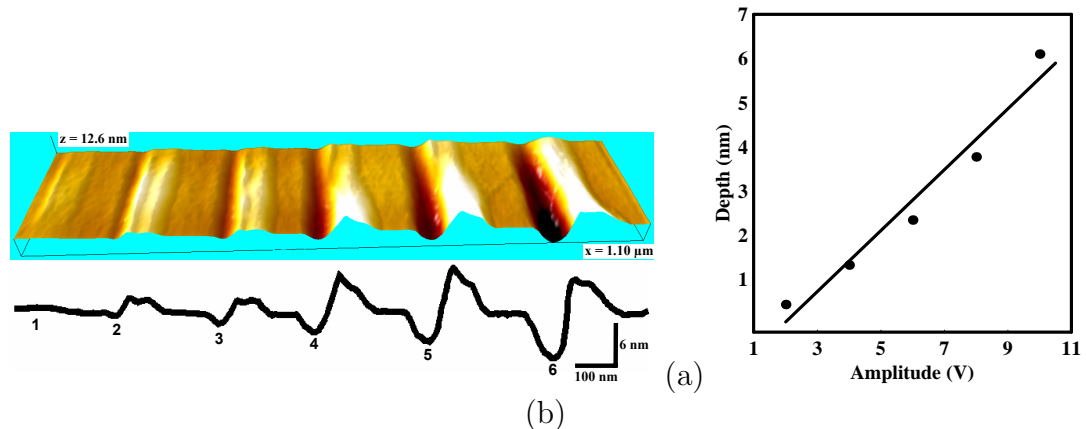
Figure 8.4: Increase in lithography depth with the magnitude of the excitation signal. The signal amplitudes for the five different traces were: trace #1, 0 V; trace #2, 2 V; trace #3, 4 V; trace #4, 6 V; trace #5, 8 V; trace #6, 10 V. (a) 3D-representation and height profile of the patterned area. (b) Relation between lithographed depth and signal magnitude (circular dots). A linear fit of the experimental data is also given.

nanomachining of the surface as observed in dynamic plowing lithography.

8.2.4   Preloading force

The coupling of the acoustic wave to the AFM tip depends on the cantilever preloading force. The preloading force is determined by the setpoint of the topography feedback prior to lithography. A lower setpoint corresponds to a greater preloading force. Thus, a dependency between the lithographed depth and the preloading force can be expected.

To investigate the influence of the preloading force, five lines were lithographed at different setpoints while applying an excitation signal of 1 V amplitude at the main resonance peak of the surface-coupled cantilever frequency response (at 879.4 kHz). As expected, a decrease of lithographed depth with increasing setpoint is observed in Fig. 8.5. This dependence has a linear character within the investigated range as seen in Fig. 8.5 (b).

Figure 8.6 shows two lithographed structures demonstrating the feasibility of the method for the generation of nanostructures on thin polymer films. Figure 8.6 (a) shows the lithographed emblem of the Ludwig Maximilians University. Figures 8.6 (b) and (c) show the AFM image and height profile respectively of three lithographed lines with a length of 4 μm. The average line width at FWHM was of 50 nm. The parameters were chosen to reach a line depth greater than 20 nm. This is relevant for the application of this method as first step in high res-
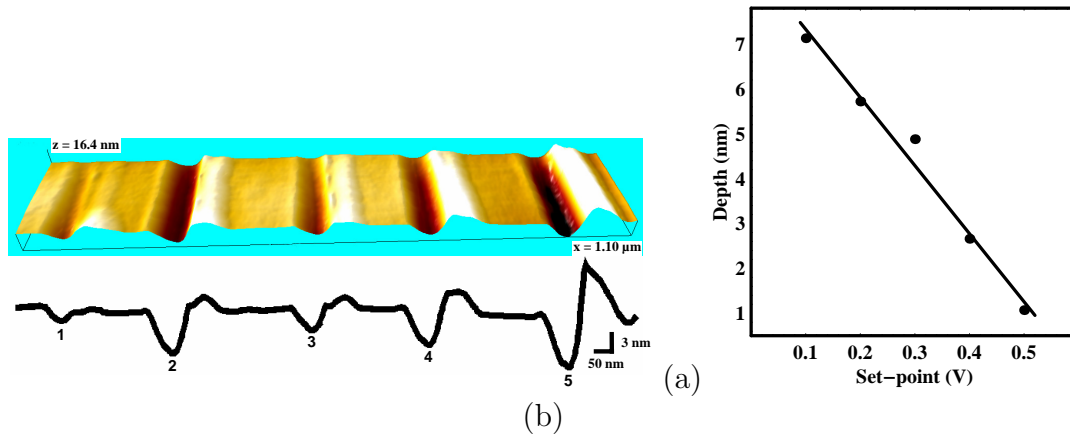
Figure 8.5: Variation of lithography depth with setpoint of the topography feedback. The corresponding setpoints were: trace #1, 0.5 V; trace #2, 0.2 V; trace #3, 0.4 V; trace #4, 0.3 V; trace #5, 0.1 V. (a) 3D-representation and height profile of the patterned area. (b) Decrease of lithographed depth with increasing setpoint (circular dots). A linear fit of the experimental data is also given.

olution lift off lithography, where thin resist layers with a thickness about 20 nm are tipically used [89].

8.3 Conclusions

Acoustical force nanolithography is an AFM lithography method providing control on the machining process by actuation of AFM cantilever through the specimen by an acoustic wave. A precise control can be achieved by tuning the excitation frequency and amplitude of the excitation to purpose. The feasibility of the method along with the characterization of the main parameters was illustrated by lithography of a thin resist film. After an initial tuning of the machining forces by fine adjustment of the excitation frequency, amplitude and setpoint, nanolithography is a reliable process. Due to the reduced physical dimensions of the AFM tip and the precise positioning and force control provided by acoustical force nanolithography, the lateral dimensions of the lithographed traces are reduced far beyond the light diffraction limit. The method is easy to implement in probe-scanning AFM configurations and can be used as a stand-alone method for surface modification or as a complement for the fine adjustment of standard mechanical machining of surfaces by AFM.
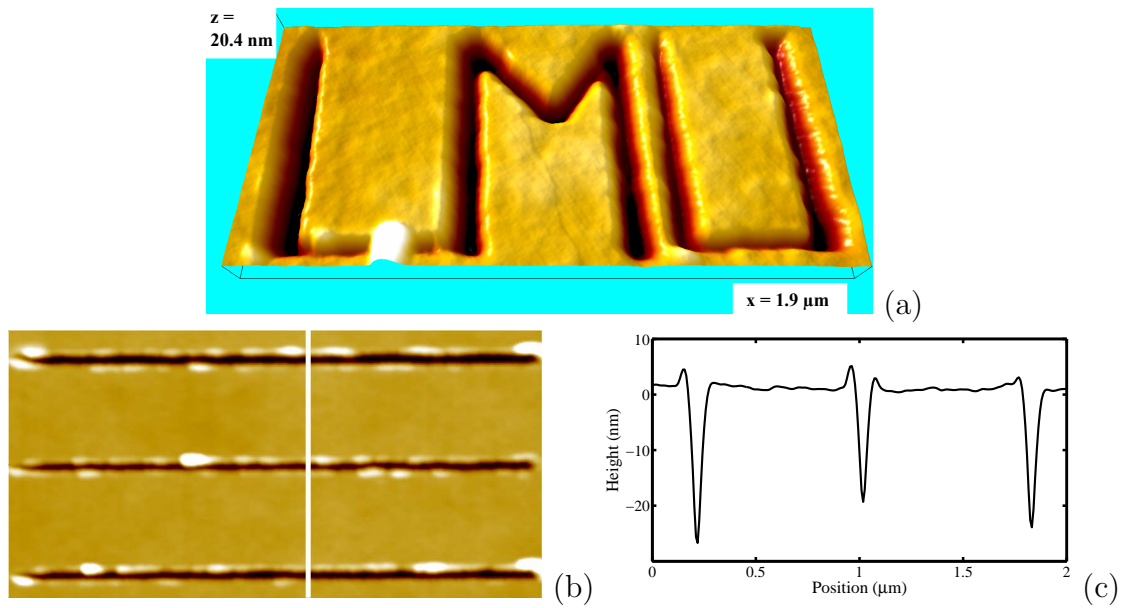
Figure 8.6: Nanostructures generated by acoustical force nanolithography: (a) lithographed emblem of the Ludwig-Maximilians-University; (b) AFM image of three 4 μm long lines lithographed using a signal amplitude of 0.5 V at a frequency of 740 kHz for acoustic wave generation with an average tip-sample distance of 12.7 nm (image size 4×2 μm^2 and Z-range 55.6 nm); (c) line height profile along the white line in panel (b) (images obtained in collaboration with Ayhan Yurtsever).

Chapter 9

Conclusions and outlook

The AFM is a valuable instrument for the controlled manipulation of surfaces with nanometer precision. The study of the instrument dynamics, the combination with other imaging and manipulation techniques, and the exploration of new cantilever actuation methods extend the possibilities and performance of AFM based lithography.

The transfer function approach presented in this thesis is a straightforward method to analyze the AFM dynamics where all resonance modes of the cantilever are considered. Using the transfer function we have studied standard configurations of the AFM system with different actuation inputs and measurement outputs, including a linearized tip-sample interaction force. The nature of the frequency response depends critically on the system configuration, i.e. on the chosen actuation force and the system output, and also on the magnitude of the tip-sample interaction. The single system configuration, in which the antiresonant frequencies are affected by the tip-sample interaction, corresponds to a distributed force input and cantilever slope output. Additionally, this system configuration is non-minimum in phase, which implies a limitation of the bandwith of a hypothetical model based controller. Using the infinite product expansion of the transfer functions we have obtained an analytical expression of all system poles and zeros, which allows for the study of system stability, range of non-minimum phase behavior, and step response. In particular, the study of the step response of the system has a direct application to the study of AFM force spectroscopy. The shift of resonant and antiresonant frequencies with varying contact stiffness is of critical importance for dynamical methods of AFM based mechanical nanolithography since it influences the magnitude of the applied load, and therefore, the indentation depth as demonstrated in acoustical force nanolithography.

To obtain a validation of the presented transfer function based model, the frequency response of AFM cantilevers has been characterized using a measurement system based on the combination of a confocal microscope and a stick-slip motor,

developed for the characterization of electromechanical devices. The experimental setup is able to acquire the frequency response along the cantilever with high precision. The obtained experimental data fits well to the frequency response predicted by the transfer function model. Of particular interest is the phase shift along the AFM cantilever, which has not been previously studied in detail in spite of its great importance for control application and phase imaging, since it determines the dynamic range of an implemented controller.

The developed NanoManipulator overcomes some limitations of state of the art AFM systems as it has been specially developed not only as an imaging tool but also as a powerful device for the manipulation of surfaces at the nanometer scale. The main features of the system are the combination with other imaging (optical microscopy) and manipulation (UV-laser ablation) methods, as well as the control of the instrument by either the automated module or the interactive approach offered by the joystick stage. The automated approach, based on the predetermination of manipulation parameters and setting of manipulation path, is an interesting approach for pattern generation on flat surfaces. In contrast, the interactive module can be applied on irregular surfaces, where the haptic sensing of the tip-sample interaction forces gives the human user the information necessary to perform the desired surface modifications. For this application the use of a simple game device such as a force-feedback joystick is a low-cost approach which yields a high performance in the tactile sensing of tip-sample interaction forces. The hardware and software of the NanoManipulator system were developed using an open-design approach, i.e. all system signals are easily accessed and the software has been developed using object-oriented standard programming which enables the implementation of new manipulation methods and also further development.

As an application of the automated module of the NanoManipulator, various AFM based dynamic lithography methods on thin resist films have been compared. In dynamic plowing, where the tip is in intermittent contact with the sample, the process produces bumps along the lithographed lines, making the process difficult to control. However, in modulated plowing, where the tip is always in contact with the sample while the indentation force is being modulated, no bumps are produced and the lithography process is highly reproducible. The mechanism of bump generation is not yet well understood although some research has been done. A detailed characterization of the process might lead to a higher controllability of bump generation, possibly representing a new method for ultra-high density data storage. Another important issue revealed by the study of the transient cantilever response during the lithography experiments is that the dynamics of the lithography process plays a critical role in the produced results.

The use of the interactive joystick module is illustrated by the dissection of human metaphase chromosomes by mechanical (modulated plowing) and non-contact

(UV-laser ablation) methods. The use of piezoelectric stages for the precise focusing of the UV-laser greatly improves the ablation spatial resolution of previous work, in which micromotors have been used for focusing the UV-laser. The mechanical dissection of the chromosomes overcomes the light diffraction limit for the spatial dimensions of the dissection cuts, and offers an alternative for the localized extraction of minimal amounts of DNA material, which can be used for a subsequent chemical analysis (such as PCR). The NanoManipulator is well-suited for biological applications, since the combination with other microscopy and manipulation methods offers a high versatility, while the joystick interface is a user-friendly and highly intuitive tool facilitating its operation by staff not familiar with AFM. The system can also be applied to other biological interesting experiments in which indentation can be used to characterize mechanical properties of biological samples or for the controlled removal of biomaterial in order to get access to buried biostructures.

Finally, the use of acoustical waves coupled through the sample surface to the cantilever for the controlled lithography of thin films is demonstrated in acoustical force nanolithography. This novel method offers a high degree of control of the process by adjusting the frequency and amplitude of the acoustic wave, and the preloading force of the cantilever. The resonance shift caused by the strong tip-sample interaction forces greatly affects the indentation forces during lithography. Acoustical force nanolithography increases the versatility of AFM as a nanopatterning tool. Additionally it is easy to implement in probe-scanning AFM configurations and can be used as a stand-alone method or for the fine adjustment of standard mechanical machining methods.

Critical issues for the further improvement of AFM based lithography are the increase of operational speed of the instrument, either by parallelization of the process or by improvement of actuator dynamics, and the consideration of the system dynamical model (transfer function) in the automated operation of the instrument. Additionally, a careful consideration of each particular experimental substrate will help to decide which system configuration and plowing method is most appropiate to achieve the desired results.

Appendix A

Software and electronics of the NanoManipulator system

In Chapter 5 we have given a detailed technical description of the NanoManipulator system. However, we omitted the diagrams of the designed circuits and the code of the developed software. However, for the sake of completeness this material is included in an accompanying CD. Those readers who get access to this work through its electronic version or are interested in further technical details of the system are encouraged to contact the author.

A.1   Electronic diagrams

The electronic diagrams are found in the directory \electronics. All circuits described in § 5.4 have been included.

A.2   Software

The code for control and operation of the NanoManipulator has been written following standard programming techniques [119, 120]. Comments have been introduced to make understable the different parts of the code.

A.2.1   Signal processor routines

The process routines implemented in the digital signal processor are found in the subdirectory \software\adwinRoutines. The routines have been programmed using ADBasic, a pseudo BASIC programming language specially developed for the ADWin system. The binary files which are directly loaded on the ADWin

system are also included. Machine code has been frequently used to boost operational speed of the different processes by direct access of the I/O addresses. The file `SignalIndex.pdf` includes a description of the global parameters and I/O connections of the ADWin system.

A.2.2   Graphical user interface code

All the files used for the programming of the graphical user interface are found in the subdirectory `\software\graphicalUserInterface`. The interface has been programmed using Visual C++ with a strong usage of the MFC library and object-oriented programming to speed the development time, facilitate further development of the interface, and code reusability. The Microsoft Visual C++ Studio (v. 6.0) has been used for the development of the graphical user interface. A compiled version of the program, which also can be used in demonstration mode, is found in the `\debug` directory (`AFM01.exe`).

Bibliography

[1] G. Binnig, H. Rohrer, C. Gerber, and E. Weibel, "7x7 reconstruction on Si(111) resolved in real space," *Phys. Rev. Lett.*, vol. 50, no. 2, pp. 120–123, 1983.

[2] M. Ringger, H. R. Hidber, R. Schlogel, P. Oelhafen, and H. J. Guntherodt, "Nanometer lithography with the scanning tunneling microscope," *Appl. Phys. Lett.*, vol. 46, no. 9, pp. 832–834, 1985.

[3] U. Staufer, R. Wiesendanger, L. Eng, L. Rosenthaler, H. R. Hidber, and H. J. Guntherodt, "Nanometer scale structure fabrication with the scanning tunneling microscope," *Appl. Phys. Lett.*, vol. 51, no. 4, pp. 244–246, 1987.

[4] A. A. Tseng, A. Notargiacomo, and T. P. Chen, "Nanofabrication by scanning probe microscope lithography: A review," *J. Vac. Sci. Technol. B*, vol. 23, no. 3, pp. 877–894, 2005.

[5] G. Binnig, C. F. Quate, and C. Gerber, "Atomic force microscope," *Phys. Rev. Lett.*, vol. 56, no. 9, pp. 930–933, 1986.

[6] M. J. Higgins, R. Proksch, J. E. Sader, J. P. Cleveland, and S. P. Jarvis, "Noninvasive determination of optical lever sensitivity in atomic force microscopy," *Rev. Sci. Instrum.*, vol. 77, p. 013701, 2006.

[7] G. Meyer and N. M. Amer, "Simultaneous measurement of lateral and normal forces with an optical-beam- deflection atomic force microscope," *Appl. Phys. Lett.*, vol. 57, pp. 2089–2091, 1990.

[8] D. Rugar, H. J. Mamin, R. Erlandsson, J. E. Stern, and B. D. Terris, "Force microscope using a fiber-optic displacement sensor," *Rev. Sci. Instrum.*, vol. 59, no. 11, pp. 2337–2340, 1988.

[9] G. Schitter, R. W. Stark, and A. Stemmer, "Sensors for closed-loop piezo control: strain gauges versus optical sensors," *Meas. Sci. Technol.*, vol. 13, pp. 47–48, 2002.

[10] J. S. Villarrubia, "Algorithms for scanned probe microscope image simulation, surface reconstruction, and tip estimation," *J. Res. Natl. Inst. Stand. Technol.*, vol. 102, pp. 425–454, 1997.

[11] P. M. Williams, K. M. Shakesheff, M. C. Davies, D. E. Jackson, and C. J. Roberts, "Blind reconstruction of scanning probe image data," *J. Vac. Sci. Technol. B*, vol. 14, no. 2, pp. 1557–1562, 1996.

[12] C. M. Mate, G. M. McClelland, R. Erlandsson, and S. Chiang, "Atomic-scale friction of a tungsten tip on a graphite surface," *Phys. Rev. Lett.*, vol. 59, no. 17, pp. 1942–1945, 1987.

[13] G. Bar, Y. Thomann, R. Brandsch, and H. J. Cantow, "Factors affecting the height and phase images in tapping mode atomic force microscopy. Study of phase-separated polymer blends of poly(ethene-co-styrene) and poly(2,6-dimethyl-1,4-phenylene oxide)of lateral and normal forces with an optical-beam- deflection atomic force microscope," *Langmuir*, vol. 13, no. 14, pp. 3807–3812, 1997.

[14] M. Basso, L. Giarré, M. Dahleh, and I. Mezic, "Complex dynamics in a harmonically excited Lennard-Jones oscillator: microcantilever-sample interaction in scanning probe microscopes," *ASME J. Dyn. Syst. Meas. Control*, vol. 122, pp. 240–245, 2000.

[15] S. Rützel, S. I. Lee, and A. Raman, "Nonlinear dynamics of atomic-force-microscope probes in Lennard-Jones potentials," *Proc. Roy. Soc. London A*, vol. 459, pp. 1925–1948, 2003.

[16] J. N. Israelachvili, *Intermolecular and surface forces.* Academic Press, London, 1985.

[17] L. D. Landau and E. M. Lifshitz, *Theory of elasticity.* Butterworth-Heinemann, Oxford, 1986.

[18] K. L. Johnson, *Contact mechanics.* Cambridge University Press, Cambridge, 1985.

[19] H. Hertz, "Über die Berührung fester elastischer Körper," *Journal für die reine und angewandte Mathemathik*, vol. 92, pp. 156–171, 1882.

[20] I. N. Sneddon, "The relation between load and penetration in the axisymmetric Boussinesq problem for a punch of arbitrary profile," *Int. J. Eng. Sci.*, vol. 3, pp. 47–57, 1965.

[21] V. M. Müller and B. V. Derjaguin, "On two methods of calculation of the force of sticking of an elastic sphere to a rigid plane," *Colloids Surf.*, vol. 7, pp. 251–259, 1983.

[22] K. L. Johnson, V. M. Müller, and B. V. Derjaguin, "Surface energy and the contact of the elastic solids," *Proc. Roy. Soc. London A*, vol. 324, pp. 301–313, 1971.

[23] D. Maugis, "Adhesion of spheres: the JKR-DMT transition using a Dugdale model," *J. Coll. Interf. Sci.*, vol. 150, pp. 243–269, 1992.

[24] E. K. Dimitriadis, F. Horkay, J. Maresca, B. Kachar, and R. S. Chadwick, "Determination of elastic moduli of thin layers of soft material using the atomic force microscope," *Biophys. J .*, vol. 82, pp. 2798–2810, 2002.

[25] B. R. Schlenker, *Introduction to material science.* John Wiley and Sons, New York, 1974.

[26] F. M. Capaldi, M. C. Boyce, and G. C. Rutledge, "Enhanced mobility accompanies the active deformation of a glassy amorphous polymer," *Phys. Rev. Lett.*, vol. 17, no. 89, p. 175505, 2002.

[27] B. Cappella and G. Dietler, "Force-distance curves by atomic force microscopy," *Surf. Sci. Rep.*, vol. 34, pp. 1–104, 1999.

[28] T. H. Fang, C. I. Weng, and J. G. Chang, "Molecular dynamics simulation of nano-lithography process using atomic force microscopy," *Surf. Sci.*, vol. 501, pp. 138–147, 2002.

[29] D. Mulliah, S. D. Kenny, R. Smith, and C. F. Sanz-Navarro, "Molecular dynamic simulations of nanoscratching of silver (100)," *Nanotechnology*, vol. 15, no. 3, pp. 243–249, 2004.

[30] I. Zarudi, W. C. D. Cheong, J. Zou, and L. C. Zhang, "Molecular dynamics simulation of nano-lithography process using atomic force microscopy," *Nanotechnology*, vol. 15, no. 1, pp. 104–107, 2004.

[31] T. A. Jung, A. Moser, H. J. Hug, D. Brodbeck, R. Hofer, H. R. Hidber, and U. D. Schwarz, "The atomic force microscope used as a powerful tool for machining surfaces," *Ultramicroscopy*, vol. 42–44, pp. 1446–1451, 1992.

[32] B. Bhushan and V. N. Koinkar, "Nanoindentation hardness measurements using atomic force microscopy," *Appl. Phys. Lett.*, vol. 64, no. 13, pp. 1653–1655, 1994.

[33] B. Klehn and U. Kunze, "Nanolithography with an atomic force microscope by means of vector-scan controlled dynamic plowing," *J. Appl. Phys.*, vol. 85, pp. 3897–3903, 1999.

[34] R. W. Stark, S. Thalhammer, J. Wienberg, and W. M. Heckl, "The AFM as a tool for chromosomal dissection - the influence of physical parameters," *Appl. Phys. A*, vol. 66, pp. 579–584, 1998.

[35] J. Yena and I. Lin, "Effect of force control algorithms on the scanning probe microscope lithography system," *Rev. Sci. Instrum.*, vol. 76, p. 036103, 2005.

[36] D. DeVecchio and B. Bhushan, "Use of nanoscale Kelvin probe for detecting wear precursors," *Rev. Sci. Instrum.*, vol. 69, pp. 3618–3624, 1998.

[37] B. Bhushan and A. V. Kulkarni, "Effect of normal load on microscale friction measurements," *Thin Solid Films*, vol. 278, no. 1, pp. 49–56, 2002.

[38] S. Sundararajan and B. Bhushan, "Development of a continuous micro-scratch technique in an atomic force microscope and its application to study scratch resistance of ultrathin hard amorphous carbon coatings," *J. Mater. Res.*, vol. 16, no. 2, pp. 437–445, 2001.

[39] T. Sumomogi, T. Endo, and K. Kuwahara, "Micromachining of metal surfaces by scanning probe microscope," *J. Vac. Sci. Technol. B*, vol. 12, no. 3, pp. 1876–1880, 1994.

[40] J. C. Rosa, M. Wendel, H. Lorenz, J. P. Kotthaus, M. Thomas, and H. Kroemer, "Direct patterning of surface quantum wells with an atomic force microscope," *Appl. Phys. Lett.*, vol. 73, pp. 2684–2686, 1998.

[41] M. Munz, B. Cappella, H. Sturm, M. Geuss, and E. Schulz, *Filler-reinforced elastomers scanning force microscopy.* Springer-Verlag, Heidelberg, 2003, ch. Materials contrasts and nanolithography techniques in scanning force microscopy (SFM) and their application to polymers and polymer composites, pp. 87–210.

[42] C. K. Wen and M. C. Goh, "AFM nanodissection reveals internal structural details of single collagen fibrils," *Nano Lett.*, vol. 4, pp. 129–132, 2004.

[43] M. Firtel, G. Henderson, and I. Sokolov, "Nanosurgery: observation of peptidoglycan strands in lactobacillus helveticus cell walls," *Ultramicroscopy*, vol. 101, pp. 105–109, 2004.

[44] S. Thalhammer, R. W. Stark, S. Müller, J. Wienberg, and W. M. Heckl, "The atomic-force microscope as a new microdissecting tool for the generation of genetic probes," *J. Struct. Biol.*, vol. 119, pp. 232–237, 1997.

[45] D. Wouters and U. Schubert, "Nanolithography and nanochemistry: probe related patterning techniques and chemical modification for nanometer-sized devices," *Angew. Chem. Int. Edit.*, vol. 43, no. 19, pp. 2480–2495, 2004.

[46] R. García, M. Tello, J. F. Moulin, and F. Biscarini, "Size and shape controlled growth of molecular nanostructures on silicon oxide templates," *Nano Lett.*, vol. 4, pp. 1115–1119, 2004.

[47] K. B. Lee, S. J. Park, C. A. Mirkin, J. C. Smith, and M. Mrksich, "Protein nanoarrays generated by dip-pen nanolithography," *Science*, vol. 295, no. 5560, pp. 1702–1705, 2002.

[48] S. Krämer, R. R. Fuierer, and C. B. Gorman, "Scanning probe lithography using self-assembled monolayers," *Chem. Rev.*, vol. 103, pp. 4367–4418, 2003.

[49] S. F. Lyuksyutov, R. A. Vaia, P. B. Paramonov, S. Juhl, L. Waterhouse, R. M. Ralich, G. Sigalov, and E. Sancaktar, "Electrostatic nanolithography in polymers using atomic force microscopy," *Nature Materials*, vol. 2, pp. 468–472, 2003.

[50] N. A. Burnham, G. Gremaud, A. J. Kulik, P. J. Gallo, and F. Oulevey, "Materials' properties measurements: choosing the optimal scanning probe microscope configuration," *J. Vac. Sci. Technol. B*, vol. 14, pp. 1308–1312, 1996.

[51] L. Meirovitch, *Analytical methods in vibrations.* Macmillan, New York, 1967.

[52] R. W. Stark, G. Schitter, M. Stark, R. Guckenberger, and A. Stemmer, "State space model of freely vibrating and surface-coupled cantilever dynamics in atomic force microscopy," *Phys. Rev. B*, vol. 69, no. 8, p. 085412, 2004.

[53] D. W. Dareing, T. Thundat, J. Sangmin, and M. Nicholson, "Modal analysis of microcantilever sensors with environmental damping," *J. Appl. Phys.*, vol. 97, no. 8, pp. 084 902.1–084 902.6, 2005.

[54] J. L. Junkins and Y. Kim, *Introduction to dynamics and control of flexible structures.* America Institute of Aeronautics and Astronautics, New York, 1993.

[55] R. E. Goodson, "Distributed system simulation using infinite product expansions," *Simulation*, vol. 15, no. 6, pp. 255–263, 1970.

[56] V. A. Spector and H. Flashner, "Modeling and design implications of non-collocated control in flexible systems," *ASME J. Dyn. Syst. Meas. Control*, vol. 112, no. 2, pp. 186–193, 1990.

[57] H. Lang, M. Hegner, and C. Gerber, "Cantilever array sensors," *Materials Today*, vol. 8, pp. 30–36, 2005.

[58] E. L. Florin, M. Radmacher, B. Fleck, and H. E. Gaub, "Atomic force microscope with magnetic force modulation," *Rev. Sci. Instrum.*, vol. 65, no. 3, pp. 639–643, 1994.

[59] C. A. J. Putman, K. O. V. der Werf, B. G. D. Grooth, N. F. V. Hulst, and J. Greva, "Tapping mode atomic force microscopy in liquid," *Appl. Phys. Lett.*, vol. 64, no. 18, pp. 2454–2456, 1994.

[60] G. Meyer and N. M. Amer, "Optical-beam-deflection atomic force microscopy: the NaCl (001) surface," *Appl. Phys. Lett.*, vol. 56, no. 21, pp. 2100–2101, 1990.

[61] B. V. Derjaguin, V. Muller, and Y. P. Toporov, "Effect of contact deformations on the adhesion of particles," *J. Colloid Interface Sci.*, vol. 53, no. 2, pp. 314–326, 1975.

[62] U. Rabe, K. Janser, and W. Arnold, "Vibrations of free and surface-coupled atomic force microscope cantilevers: theory and experiment," *Rev. Sci. Instrum.*, vol. 67, no. 9, pp. 3281–3293, 1996.

[63] M. Rief, F. Oesterhelt, B. Heymann, and H. E. Gaub, "Single molecule force spectroscopy on polysaccharides by atomic force microscopy," *Science*, vol. 275, no. 11, pp. 1295–1297, 1997.

[64] B. Anczykowski, B. Gotsmann, H. Fuchs, J. P. Cleveland, and V. B. Elings, "How to measure energy dissipation in dynamic mode atomic force microscopy," *Appl. Surf. Sci.*, vol. 140, pp. 376–382, 1999.

[65] G. Simmons, *Differential equations with applications and historical Notes*. McGraw-Hill, New York, 1991.

[66] G. F. Franklin, J. D. Powell, and A. Emami-Naeini, *Feedback control of dynamic systems*. Addison-Wesley, Reading, MA, 1986.

[67] R. Garcia and R. Perez, "Dynamic atomic force microscopy methods," *Surf. Sci. Reports*, vol. 47, no. 6, pp. 197–301, 2002.

[68] C. A. Bippes, A. D. L. Humphris, M. Stark, D. J. Müller, and H. Janovjak, "Direct measurement of single-molecule visco-elasticity in atomic force microscope force-extension experiments," *Eur. Biophys. J.*, vol. 35, no. 3, pp. 287–292, 2006.

[69] H. O. Hao, A. M. Baro, and J. J. Sanz, "Electrostatic and contact forces in force microscopy," *J. Vac. Sci. Technol. B*, vol. 9, pp. 1323–1328, 1991.

[70] I. N. Bronstein, K. A. Semendjajew, G. Musiol, H. Musiol, and H. Mühlig, *Taschenbuch der Mathematik*. Harri Deutsch, Frankfurt am Main, 1977.

[71] T. M. Apostol, *Calculus, Vol. 1.* John Wiley and Sons, New York, 1967.

[72] B. Serio, J. J. Hunsinger, and B. Cretin, "In-plane measurements of micro-electromechanical systems vibrations with nanometer resolution using the correlation of synchronous images," *Rev. Sci. Instrum.*, vol. 75, no. 10, pp. 3335–3341, 2004.

[73] M. Reinstaedtler, U. Rabe, V. Scherer, J. A. Turner, and W. Arnold, "Imaging of flexural and torsional resonance modes of atomic force microscopy cantilevers using optical interferometry," *Surf. Sci.*, vol. 532, pp. 1152–1158, 2003.

[74] T. Sulchek, G. G. Yaralioglu, C. F. Quate, and S. C. Minne, "Characterization and optimization of scan speed for tapping-mode atomic force microscopy," *Rev. Sci. Instrum.*, vol. 73, no. 8, pp. 2928–2936, 2002.

[75] C. Meyer, "Nanoelektromechanische Siliziumaktuatoren und deren optische Charakterisierung," Ph.D. dissertation, Department of Physics at the University of Munich, 2004.

[76] C. Meyer, O. Sqalli, H. Lorenz, and K. Karrai, "Slip-stick step-scanner for scanning probe microscopy," *Rev. Sci. Instrum.*, vol. 76, p. 063706, 2005.

[77] S. Dohn, R. Sandberg, W. Svendsen, and A. Boisen, "Enhanced functionality of cantilever based mass sensors using higher modes," *Appl. Phys. Lett.*, vol. 86, p. 233501, 2005.

[78] S. N. Magonov, J. Cleveland, V. Elings, D. Denley, and M. H. Whangbo, "Tapping-mode atomic force microscopy study of the near-surface composition of a styrene-butadiene-styrene triblock copolymer film," *Surf. Sci.*, vol. 389, pp. 201–211, 1997.

[79] S. Thalhammer, R. W. Stark, K. Schütze, and W. M. Heckl, "Laser microdissection of metaphase chromosomes and characterization by atomic force microscopy," *Journal of Biomedical Optics*, vol. 2, no. 1, pp. 115–119, 1997.

[80] M. Heyde, K. Rademann, B. Cappella, M. Geuss, H. Sturm, T. Spangenberg, and H. Niehus, "Dynamic plowing nanolithography on polymethylmethacrylate using an atomic force microscope," *Rev. Sci. Instrum.*, vol. 72, no. 1, pp. 136–141, 2001.

[81] M. R. Falvo, G. Clary, A. Helser, S. Paulson, R. M. Taylor II, V. Chi, F. P. Brooks Jr, S. Washburn, and R. Superfine, "Nanomanipulation experiments exploring frictional and mechanical properties of carbon nanotubes," *Microsc. Microanal.*, vol. 4, pp. 504–512, 1998.

[82] F. J. Rubio-Sierra, R. Stark, S. Thalhammer, and W. M. Heckl, "Force-feedback joystick as a low-cost haptic interface for an atomic-force-microscopy nanomanipulator," *Appl. Phys. A*, vol. 76, no. 6, pp. 903–906, 2003.

[83] D. Knebel, M. Amrein, K. Voigt, and R. Reichelt, "A fast and versatile scan unit for scanning probe microscopy," *Scanning*, vol. 19, no. 4, pp. 264–268, 1997.

[84] J. Kwon, J. Hong, Y. S. Kim, D. Lee, K. Lee, S. M. Lee, and S. I. Park, "Atomic force microscope with improved scan accuracy, scan speed, and optical vision," *Rev. Sci. Instrum.*, vol. 74, no. 10, pp. 4378–4383, 2003.

[85] P. Horowitz and W. Hill, *The art of electronics*. Cambridge University Press, Cambridge, 1977.

[86] H. J. Butt and M. Jaschke, "Calculation of thermal noise in atomic force microscopy," *Nanotechnology*, vol. 6, pp. 1–7, 1995.

[87] R. Lévy and M. Maaloum, "Measuring the spring constant of atomic force microscope cantilevers: thermal fluctuations and other methods," *Nanotechnology*, vol. 13, pp. 33–37, 2002.

[88] R. W. Stark and W. M. Heckl, *Procedures in Scanning Probe Microscopies*. John Wiley and Sons, London, 1998, ch. Preparation of a compact disk as a calibration sample for AFM, pp. 146–148.

[89] C. Martín, G. Rius, X. Borrisé, and F. Pérez-Murano, "Nanolithography on thin layers of PMMA using atomic force microscopy," *Nanotechnology*, vol. 16, pp. 1016–1022, 2005.

[90] R. W. Stark, F.-J. Rubio-Sierra, S. Thalhammer, and W. M. Heckl, "Combined nanomanipulation by atomic force microscopy and UV-laser ablation for chromosomal dissection," *Eur. Biophys. J.*, vol. 32, no. 1, pp. 33–39, 2003.

[91] B. Cappella, "Dynamic Plowing Lithography und Kraft-Abstands-Kurven Indentation als lithographische Methoden für die Modifizierung von Polymeroberflächen," Ph.D. dissertation, Processscience Faculty at the Technical University of Berlin, 2002.

[92] B. Cappella and H. Sturm, "Dynamic plowing lithography of single holes on polymethylmethacrylate using an atomic force microscope," *Acta Microscopica*, vol. 10, pp. 8–18, 2001.

[93] X. Jin and W. N. Unertl, "Submicrometer modification of polymer surfaces with a surface force microscope," *Appl. Phys. Lett.*, vol. 61, pp. 657–659, 2001.

[94] E. Hamada and R. Kaneko, "Micro-tribological evaluations of a polymer surface by atomic force microscopes," *Ultramicroscopy*, vol. 184, pp. 42–44, 1992.

[95] M. Wendel, H. Lorenz, and J. P. Kotthaus, "Sharpened electron beam deposited tips for high resolution atomic force microscope lithography and imaging," *Appl. Phys. Lett.*, vol. 184, pp. 3732–3734, 1995.

[96] B. G. De Grooth and C. A. Putman, "High-resolution imaging of chromosome-related structures by atomic force microscopy," *J. Microsc.*, vol. 168, pp. 239–247, 1992.

[97] W. Fritzsche, A. Schaper, and T. M. Jovin, "Probing chromatin with the scanning force microscope," *Chromosoma*, vol. 103, pp. 231–236, 1994.

[98] T. J. McMaster, M. O. Winfield, A. A. Baker, A. Karp, and M. J. Miles, "Chromosome classification by atomic force microscopy volume measurement," *J. Vac. Sci. Technol. B*, vol. 14, pp. 1438–1443, 1996.

[99] J. Tamayo and M. Miles, "A scanning probe microscopy for chromosomal research," *Arch. Histol. Cytol.*, vol. 65, no. 5, pp. 369–376, 2002.

[100] T. D. Gelehrter and F. S. Collins, *Principles of medical genetics*. Williams & Wilkins, Baltimore, 1990.

[101] H. Lüdecke, G. Senger, U. Claussen, and B. Horsthemke, "Cloning defined regions of the human genome by microdissection of banded chromosomes and enzymatic amplification," *Nature*, vol. 338, pp. 348–350, 1989.

[102] M. W. Berns, R. S. Olson, and D. E. Rounds, "In vitro production of chromosomal lesions with an argon laser microbeam," *Nature*, vol. 221, pp. 74–75, 1969.

[103] C. Lengauer, A. Eckelt, A. Weith, N. Endlich, N. Ponelies, P. Lichter, K. Greulich, and T. Cremer, "Painting of defined chromosomal regions by in situ suppression hybridization of libraries from laser-microdissected chromosomes," *Cytogenet Cell Genet.*, vol. 56, pp. 27–30, 1969.

[104] L. Schermelleh, S. Thalhammer, W. M. Heckl, H. Pösl, T. Cremer, K. Schütze, and M. Cremer, "Laser microdissection and laser pressure catapulting for the generation of chromosome-specific paint probes," *Biotechniques*, vol. 27, pp. 362–367, 1999.

[105] K. Schütze, I. Becker, K. F. Becker, S. Thalhammer, R. W. Stark, W. M. Heckl, M. Bohm, and H. Pösl, "Cut out or poke in - the key to the world of single genes: laser micromanipulation as a valuable tool on the look-out for the origin of disease," *Genet. Anal.*, vol. 14, pp. 1–8, 1997.

[106] A. Clement-Sengewald, T. Buchholz, and K. Schütze, "Laser microdissection as a new approach to prefertilization genetic diagnosis," *Pathobiology*, vol. 88, pp. 232–236, 2000.

[107] K. O. Greulich, *Micromanipulation by Light in Biology and Medicine: the laser microbeam and optical tweezers.* Birkhäuser, Basel, 1999.

[108] R. Srinivasan, "Ablation of polymers and biological tissue by ultraviolet-lasers," *Science*, vol. 234, pp. 559–565, 1986.

[109] D. Bäuerle, *Laser processing and chemistry.* Springer-Verlag GmbH & Co, Heidelberg, 2000.

[110] E. Henderson, "Imaging and nanodissection of individual supercoiled plasmids by atomic force microscopy," *Mol. Biol.*, vol. 20, no. 3, pp. 445–447, 1992.

[111] J. H. Lü, H. K. Li, H. J. An, G. H. Wang, Y. Wang, M. Q. Li, Y. Zhang, and J. Hu, "Positioning isolation and biochemical analysis of single DNA molecules based on nanomanipulation and single-molecule pcr," *J. Am. Chem. Soc.*, vol. 126, no. 36, pp. 11 136–11 137, 2004.

[112] C. Mosher, D. Jondle, J. Vesenka, and E. Henderson, "Microdissection and measurement of polytene chromosomes using the atomic force microscope," *Scanning Microsc.*, vol. 8, no. 3, pp. 491–497, 1994.

[113] D. Jondle, L. Ambrosio, J. Vesenka, and E. Henderson, "Imaging and manipulating chromosomes with the atomic force microscope," *Chromosome Res.*, vol. 3, no. 4, pp. 239–244, 1995.

[114] S. Iwabuchi, T. Mori, K. Ogawa, K. Sato, M. Saito, and Y. Morita, "Atomic force microscope-based dissection of human metaphase chromosomes and high resolutional imaging by carbon nanotube tip," *Arch. Histol. Cytol.*, vol. 65, no. 5, pp. 473–479, 2002.

[115] M. Oberringer, A. Englisch, B. Heinz, H. Gao, T. Martin, and U. Hartmann, "Atomic force microscopy and scanning near-field optical microscopy studies on the characterization of human metaphase chromosomes," *Eur. Biophys. J.*, vol. 32, no. 7, pp. 620–627, 2003.

[116] J. E. Sader, J. W. M. Chon, and P. Mulvaney, "Calibration of rectangular atomic-force microscope cantilevers," *Rev. Sci. Instrum.*, vol. 70, pp. 3967–3969, 1999.

[117] F. Vogel and A. G. Motulsky, *Human genetics: problems and approaches.* Springer, Berlin, 1997.

[118] B. Lerner, "Toward a completely automatic neural-network-based human chromosome analysis," *IEEE Trans. On Systems, Man, and Cybernetics, Part B*, vol. 28, no. 4, pp. 544–552, 1998.

[119] B. Stroustrup, *The C++ Programming Language.* Addison-Wesley Professional, Boston, 2000.

[120] J. Prosise, *Programming Windows 95 With MFC.* Microsoft Press, Redmond, 1996.

Publications

Following articles, published in peer-reviewed scientific journals, contain parts of this work:

1. F. J. Rubio-Sierra, R. Vázquez, and R. W. Stark, "Transfer function analysis of the micro cantilever used in atomic force microscopy," *IEEE Trans. on Nanotechnology*, vol. 5, no. 6, pp. 692–700, 2006.

2. F. J. Rubio-Sierra, A. Yurtserver, M. Hennemeyer, W. M. Heckl, and R. W. Stark, "Acoustical force nanolithography of thin polymer films," *Phys. Status Solidi (a)*, vol. 203, no. 6, pp. 1481–1486, 2006.

3. F. J. Rubio-Sierra, W. M. Heckl, and R. W. Stark, "Nanomanipulation by Atomic Force Microscopy," *Adv. Eng. Mater.*, vol. 7, no. 4, pp. 193–196, 2005.

4. F. J. Rubio-Sierra, R. W. Stark, S. Thalhammer, and W. M. Heckl, "Force feedback joystick as a low cost haptic interface for an atomic force microscopy nanomanipulator," *Appl. Phys. A*, vol. 76, pp. 903–906, 2002.

Further publications in scientifical journals, including conference proceedings:

5. R. Vázquez, F. J. Rubio-Sierra, and R. W. Stark, "Transfer function analysis of a surface coupled atomic force microscope cantilever system," *Proc. of the 2006 American Control Conf.*, June 14–16, 2006, Minneapolis, Minnesota, USA.

6. F. J. Rubio-Sierra, R. Vázquez, and R. W. Stark, "Transfer Function Analysis of Atomic Force Microscope Cantilevers," *Conf. Proc. of the ASME International Mechanical Engineering Congress and Exposition*, Nov. 5–11, 2005 Orlando, Florida, USA.

7. F. J. Rubio-Sierra, S. Burghardt, A. Kempe, W. M. Heckl, and R. W. Stark, "Atomic force microscope based nanomanipulator for mechanical and optical lithography," *Proc. of the 2004 4th IEEE Conf. of Nanotechnology*, 17.-19. August Munich, Germany, pp. 468–470.

8. R. W. Stark, F. J. Rubio-Sierra, S. Thalhammer, and W. M. Heckl, "Combined nanomanipulation by atomic force microscopy and UV-laser ablation for chromosomal dissection," *Eur. Biophys. J.*, vol. 32, no. 1, pp. 33–39, 2003.

Contributions in scientific conferences and invited seminars:

9. "Transfer function analysis of atomic force microscope cantilevers," *ASME International Mechanical Engineering Congress and Exposition*, November 2005 in Orlando, Florida, USA.

10. "Lithography of polymer thin films by acoustic force microscope (poster)," *SPM Workshop 2005*, September 2005 in Munich, Germany.

11. "Acoustic Force Lithography (poster)," *Trends in Nanotechnology Conference 2005*, September 2005 in Oviedo, Spain.

12. "Toward controlled nanomanipulation by atomic force microscope," *Kristallographisches Oberseminar*, June 2005 at the Crystallography Section in the LMU Munich, Germany.

13. "Development of nanomanipulation by AFM," *2. ENNaB-Workshop: BMBF Junior Research Groups in Nanotechnology*, April 2005 in Munich, Germany.

14. "AG Heckl: Scanning probe microscopy group at the University of Munich," *CeNS Winter Workshop*, February 2005 in Mauterndorf, Austria.

15. "Atomic force microscope based nanomanipulator for mechanical and optical lithography," *Scanning Probe Microscopies and Organic Materials XIII*, September 2004 in Bielefeld, Germany.

16. "Atomic Force Microscope based nanomanipulator for mechanical and optical lithography (poster)," *IEEE-NANO 2004*, August 2004 in Munich, Germany.

17. "Nanomanipulation by AFM," *1. ENNaB-Workshop: BMBF Junior Research Groups in Nanotechnology*, July 2004 in Munich, Germany.

18. "User friendly nanomanipulator for mechanical and photonic manipulation," *Nanoanalytik Workshop*, April 2002 in Hamburg, Germany.

Acknowledgments

At the end of this thesis, I would like to thank to all the people whose contribution, advice or support have made the realization of this work possible. In the following I want to acknowledge some of them especially.

Prof. Dr. Wolfgang M. Heckl for giving me the chance to work on the *NanoManipulator* project and for sharing with me his views about science and technology.

Dr. Robert W. Stark for the exceptional coaching of this work and for supporting me with interesting motivations and ideas of new possibilities for the development of the AFM as a lithography tool, along with his insights on high resolution characterization of surface properties.

Stefan Burghart and Eduardo Macías for their professional help in the technical development of the *NanoManipulator*, specially in the construction of the electronic parts and the mechanical design of microscope components.

Rafael Vázquez for the excellent and fruitful team work in the development of the transfer function description of the AFM, his brilliant mathematical insights and for making me understand that there is only one thing more interesting than doing mathematics: speaking about them.

Ayhan Yurtserver for the collaboration in the development of acoustical force nanolithography and his tireless energy in the performance of measurements.

Marc Hennemeyer for the preparation of the thin resist films, language revision of the *Zusammenfassung*, and interesting discussions at lunchtime.

Dr. Stefan Thalhammer for the preparation of the human metaphase chromosome samples and helpful advise about UV-laser ablation.

Dr. Christine Meyer and Constanze Metzger at the Physics Department in the LMU München for facilitating the use of the confocal measurement setup and assistance in the measurement of cantilever dynamics.

Prof. Miroslav Krstic at the Department of Mechanical and Aerospace Engineering in the University of California, San Diego for his insights in control engineering applied to non-linear systems.

Günter Hesberg and the people of the fine mechanics workshop for the outstanding precision work achieved in the machining of the *NanoManipulator* components.

Lebenslauf

Francisco Javier Rubio-Sierra

1975	Geburt in Sevilla (Spanien)
1981–1993	Schule Sagrados Corazones in Sevilla (Spanien)
1993	Allgemeine Hochschulreife (Selectividad)
1993-2000	Studium der Physik (Diplom) an der Universidad de Sevilla
2001	Wissenschaftliche Arbeit in der Art einer Diplomarbeit "Aufbau und Test eines Nanomanipulators", am Institut für Kristallographie und Angewandte Mineralogie, Arbeitsgruppe Prof. Dr. W. M. Heckl
seit 2002	Promotionsstudium im Fach Geologie/Paläontologie am Institut für Kristallographie und Angewandte Mineralogie, Arbeitsgruppe Prof. Dr. W. M. Heckl